Experimental Condensed Matter Physics

28

Adding nonlinearity to an electromagnetic-magnonic quantum hybrid device

Marco Pfirrmann

KIT Scientific Publishing

Marco Pfirrmann

Adding nonlinearity to an electromagnetic-magnonic quantum hybrid device

Experimental Condensed Matter Physics
Band 28

Herausgeber
Physikalisches Institut
Prof. Dr. David Hunger
Prof. Dr. Alexey Ustinov
Prof. Dr. Georg Weiß
Prof. Dr. Wolfgang Wernsdorfer
Prof. Dr. Wulf Wulfhekel

Eine Übersicht aller bisher in dieser Schriftenreihe erschienenen Bände finden Sie am Ende des Buchs.

Adding nonlinearity to an electromagnetic-magnonic quantum hybrid device

by
Marco Pfirrmann

KIT Scientific Publishing

Karlsruher Institut für Technologie
Physikalisches Institut

Adding nonlinearity to an electromagnetic-magnonic quantum hybrid device

Zur Erlangung des akademischen Grades eines Doktors der Naturwissenschaften von der KIT-Fakultät für Physik des Karlsruher Instituts für Technologie (KIT) genehmigte Dissertation

von M. Sc. Marco Pfirrmann

Tag der mündlichen Prüfung: 22. November 2019
Referent: Prof. Dr. Martin Weides
Korreferent: Prof. Dr. Alexey V. Ustinov

Impressum

KIT Scientific Publishing

Karlsruher Institut für Technologie (KIT)
KIT Scientific Publishing
Straße am Forum 2
D-76131 Karlsruhe

www.ksp.kit.edu

Print on Demand 2020 – Gedruckt auf FSC-zertifiziertem Papier

ISSN 2191-9925
ISBN 978-3-7315-1003-1
DOI 10.5445/KSP/1000104130

Contents

1 Introduction

Quantum technologies promise to revolutionize the world we live in by using devices that utilize quantum effects [1] such as quantum state supersposition and entanglement to provide access to features that go beyond what is classically possible. With the 2012 Nobel prize in physics awarded to David Wineland and Serge Haroche [2] *"for ground-breaking experimental methods that enable measuring and manipulation of individual quantum systems"*, the expectation on quantum technology is now higher than ever. For example, the impact on quantum chemistry by simulating complex molecules is probably one of the most anticipated applications of quantum simulation [3], while encryption software companies are already developing and implementing post-quantum cryptography algorithms to counteract the computational speedup [4].

Billions of Euros of public funding worldwide, such as the multi-national European quantum technology flagship initiative [5], illustrate not only the technological importance of quantum technologies for the future, but also the hope for a long-term economical impact similar to the mid-20th century semiconductor industry, which resulted in the success story of the Silicon Valley. At the same time, large international companies such as Google [6], IBM [7, 8], and Microsoft [9] invest heavily in their own quantum research groups, attracting the attention of scientists, the media, and the general public alike.

In analogy to classical computers, quantum information processing builds on quantum bits (qubits) as its basic processing units [10]. While a classical bit operates in binary 0 and 1, a qubit operates in a quantum superposition state $|\Psi\rangle = \alpha\,|g\rangle + \beta\,|e\rangle$ that when measured collapses into either its ground state $|g\rangle$ or excited state $|e\rangle$. Although a single qubit does not offer a particular advantage over a classical bit, combining multiple interacting qubits in a joint Hilbert space potentionally offers exponential computational speedup compared to a classical computer for a certain class of problems [11]. A recently published paper by the Google group [12] claims to have shown the proposed quantum supremacy for the first time ever by performing a computational task on a 53 individually controllable qubit chip, which *"for a state-of-the-art classical supercomputer would take approximately 10,000 years."*, with the significance of this archievement compared to the Wright's brothers first

flight: *"It is what the event represented, rather than what it practically accomplished, that was paramount"* [13].

Of the different technologies nowadays considered as the basis for quantum computing, qubits based on superconductivity [14] are currently at the forefront of a solid state approach [15]. Superconducting nanostructures that utilize the Josephson effect result in a non-linear and non-dissipative circuit element, which forms the base building block of such a qubit. Together with quantum versions of capacitors and inductors, quantum electrodynamic architectures combine these qubits with superconducting resonators to encoded, manipulate, and retrieve quantum information using microwave photons [16, 17].

Despite the engineering progress and technological developments in recent years, there are still certain limitations in superconducting quantum circuits. Typically operating in the single digit gigahertz regime, such a system requires operation in a cryogenic environment at temperatures near absolute zero to freeze out thermal excitations and minimal probing power to not suppress the quantum effects. Qubit parameter fluctuation [18–20], unintentional crosstalk between on-chip components, and the need for constant elaborate error-correction while performing algorithms due to insufficient coherence times [21] renders the implementation of a universal superconducting quantum computer quite challenging. On top comes the connection to the outside world and the need for efficient transport and storage of quantum information.

Intrinsic advantages and disadvantages of all technological quantum platforms lead to the emergence of quantum hybrid devices, which ultimatly combine the advantages of the nature of each different physical system [22] and aim for quantum communication and quantum enhanced sensing. Nitrogen vacancy based spin systems [23] with their large coherence times, for example, are hybridized with photons to convert quantum excitation into the optical photon band band for quantum network communication [24, 25] and nuclear spins for quantum memories exceeding over one second [26].

The engineered level structure of a superconducting qubit, basically an artificial atom with designed energy transitions, makes it ideal for the study of the interaction of matter with other physical systems beyond natural limitations [27] and quantum sensing applications [28, 29], which rely on the high sensitivity of any coherent quantum system regarding external influences to precisely measure physical quantities. The sensing of small magnetic fields [30, 31] or the coupling to single electron or nuclear spins with superconducting qubits is of great interest for quantum application. On the other hand, the direct coupling between the spin of a single electron and a superconducting resonator is too weak to reach the coherent coupling

regime. It is therefore necessary to enhance the coupling strength by using a large number of spins in paramagnetic spin ensembles [32], i.e. based on erbium doped crystals [33–35]. Recently, the scope of quantum hybrid system was expanded to collective bulk magnetic excitation.

The general phenomenon of magnetism has been known for a long time in human history and is omnipresent in modern everyday life beyond the field of science. The physical origins of bulk magnetism in solids however, are purely quantum mechanical as stated in the Bohr-van Leeuwen theorem [36, 37]. The exchange interaction between magnetic moments in a ferromagentic material allows for collective spin excitation, phase-coherent precession of the magnetization vector [38, 39], that spread over the crystal lattice and are described as a wave similar to phonon excitation. These spin waves, quantized as magnons [40, 41], are utilized in ferromagnetic resonance (FMR) experiments, which are used as a powerful technique for investigating magnetic properties in materials. The excitation of spin waves by microwave photons via magnetic dipole interaction [42] or Brillouin Light scattering [43], as well as the macroscopic quantum phenomenon of Bose–Einstein condensation of magnons [44] stimulated the field of magnonics [45, 46], aiming at transport and information processing via magnons on the nanoscale.

The concept of a strongly coupled spin-photon hybrid excitation using ferromagnets was proposed [47–49] and realized [50] using gallium doped yttrium iron garnet (YIG), with the hybridized modes forming a cavity magnon polariton quasiparticle [51, 52]. With their large spin-spin coupling and high spin density, ferromagnetic excitations are described by a macro spin, which results in a higher magnon-photon coupling strength compared to paramagnetic spin ensembles. Subsequent cavity magnon polariton experiments using three dimensional microwave cavities explore the system at room temperature [53] and show ultra strong collective coupling [53–55], with the general concept also being expanded to cavity optomagnonics using optical photons [56–59] or mechanical degrees of freedom [57, 60].

Strong coupling approaching the quantum limit of excitation [61–64] opens the door to nonlinear hybrid quantum systems containing magnons and superconducting qubits [65, 66], using the microwave photon as common coupling partner, see Fig.1.1. With all the previous systems being purely harmonic, this allows for the first time to address the quantum properties of single magnons and opens the field of quantum magnonics with strong and coherent interaction between superconducting qubits and magnetostatic modes. With further studies counting magnon excitation [67], single magnon detection [68], and the quantum simulation of quasi-particles consisting of fermions and bosons [69], magnon-based hybrid quantum system offer a large opportunity for new quantum technologies such as quantum sensing [61, 70], quantum transducer [71] or the search for dark matter via

axion to magnon conversion [72–74]. The main challenge hereby is to mediate the opposing nature of magnetic fields and superconductivity, with the need for spatial separation and a quantum bus in a three dimensional approach, or magnetic fields confined in a small volume in two dimensions.

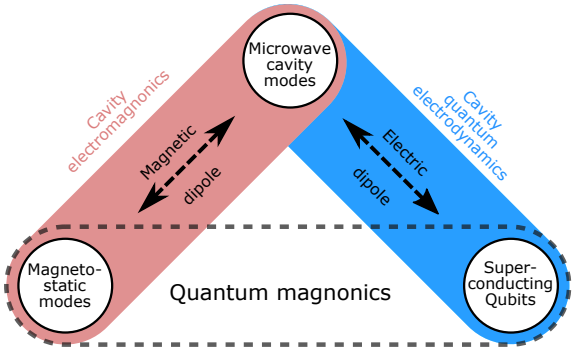

Figure 1.1: Quantum magnonic coupling scheme Quantum magnonics combines collective magnetostatic modes with superconducting qubits via indirect photon-mediated coupling using different components of the electromagnetic field. Inspired by [75].

In this thesis, we study nonlinear quantum circuits based on magnetic materials, with the focus on yttrium iron garnet due to its unmatched low internal damping and high spin density. As the basis for this thesis, we introduce collective spin excitation as a harmonic system and describe the spin-photon coupling mechanism with the focus on cavity-magnonics, where microwave photons in a three dimensional cavity resonator couple with magnons via their magnetic field component. We then establish the superconducting quantum bit as a nonlinear element and discuss how a qubit is operated in a quantum circuit. The following chapter combines the two systems under the concept of quantum magnonics, where we introduce effective coupling mechanisms between magnetic excitation and the qubit via microwave modes. A chapter about the experimental methods used in this thesis and basic resonator characterization measurement prepare for the measurements of various hybrid systems.

The experimental part of the thesis is divided into two main chapters. First, a strongly coupled harmonic magnon-photon system is studied at the experimental working conditions of a superconducting quantum circuit. We probe the system using continuous microwave spectroscopy, with the focus on the magnetic resonance linewidth in order to identify the dominating loss mechanisms of magnetic excitations at various experimental conditions from several kelvin [76] down to millikelvin temperatures and single excitation powers [62]. In addition, we focus on the influence

of the energy mixing ratio between the magnon and photon share in the resulting cavity magnon polariton quasiparticle on the magnetic linewidth.

In the second experimental chapter we add the superconducting qubit to the system, containing now three circuit elements. The nonlinear quantum system is studied in two opposite regimes, which mainly differ in the frequency detuning between the qubit and the microwave frequency. In the dispersive regime, at a large detuning on the order of 100 megahertz, we study the coherent interaction between single magnetic excitation and the superconducting qubit, where we demonstrate indirect qubit-magnon coupling and coupling enhancement by the participating number of spins. We modify the cavity resonance to push the system to the opposite end of the detuning spectrum, where qubit and microwave photon are almost on resonance, with a detuning on the order of ten megahertz. We spectroscopically study the coupling strengths of the tripartite system and find coherent coupling at two working points. Thermally excited multi-photon transitions are observed at various temperatures and identified by simulation. The thesis concludes with time dependent measurements regarding Rabi oscillations on the tripartite system as a prerequisite for more sophisticated implementations of magnetic excitation in nonlinear quantum circuits.

2 Cavity electromagnonics

This chapter presents the basic building blocks of interaction between magnetic excitations (magnons) and microwave cavity photons, which is mediated by the magnetic field component of the photon being the connecting component. We approach the hybrid system from the side of cavity electromagnonics, where photons at a fixed resonator frequency with confined magnetic fields are used to probe magnetic excitations. At matching frequencies, the coupled system is described by a quasiparticle, the cavity magnon polariton. This stands in contrast to traditional ferromagnetic resonance (FMR) experiments, which are usually performed with photons in transmission lines at different frequencies, ranging over several GHz. Despite being able to reduce the excitation number to single digits by reducing thermal excitation, there are no quantum effects present in the coupled system, which in our case is purely harmonic. We begin by discussing microwave resonators and afterwards introduce collective spin excitations in magnetic materials which are described as quasiparticles that represent the bosonic states of a harmonic oscillator. We continue with the coupling between the two systems and their coupling strength, as well as the microwave reflection spectrum of the coupled system. The chapter concludes with a discussion about the used magnetic material and different magnetic loss mechanisms.

2.1 Microwave cavity resonators

We probe the magnetic excitation with microwaves and use the magnetic field component of a three dimensional microwave resonator to excite the magnons. The amount of excitation energy expressed in number of photons is an important experimental parameter, since many effects in the quantum regime are power dependent. We estimate the average photon occupation in the resonator by its characteristic quality factors that describe its ability to couple excitation in and out and pass it to the magnetic sample.

A three dimensional microwave cavity resonator is formed by a closed box, where modes of standing waves of the electromagnetic field form the resonance photon. The

energy is stored within the cavity and dissipated in the metallic walls or the filling dielectric material. While a cavity can hold an infinite number of resonance modes, there is a dominant mode given by the lowest resonance frequency. Resonances in a rectangular cavity are described by their wave number

$$k_{mnl} = \sqrt{\left(\frac{m\pi}{a}\right)^2 + \left(\frac{n\pi}{b}\right)^2 + \left(\frac{l\pi}{d}\right)^2}, \tag{2.1}$$

with m, n, and l describe the number of anti-nodes in the standing wave pattern and a, b, and d the edge length in the x, y, and z direction, respectively. See Fig. 2.1 for a depiction of a rectangular cavity and the electric field components of the transverse electrical (TE) modes TE_{101} and TE_{102}. Our notation here is the same as in Ref. [77]. The resonance frequency of all modes is given by

$$\omega_{mnl}/2\pi = \frac{ck_{mnl}}{\sqrt{\mu_\mathrm{r}\epsilon_\mathrm{r}}} = \frac{c}{\sqrt{\mu_\mathrm{r}\epsilon_\mathrm{r}}}\sqrt{\left(\frac{m\pi}{a}\right)^2 + \left(\frac{n\pi}{b}\right)^2 + \left(\frac{l\pi}{d}\right)^2}, \tag{2.2}$$

with c being the speed of light and μ_r and ϵ_r the filling material's properties.

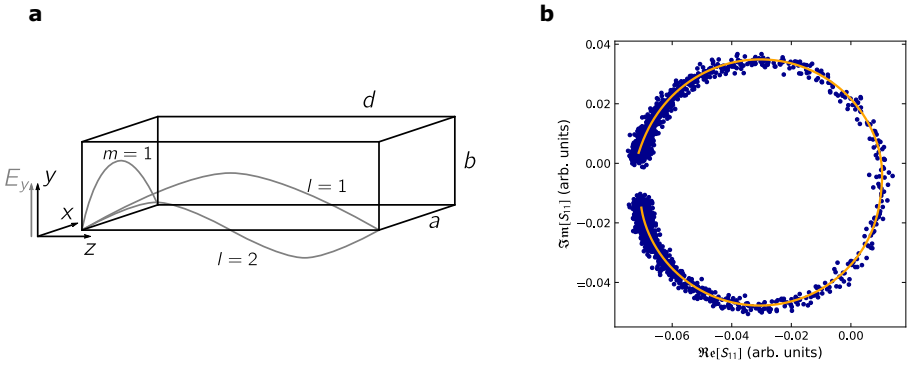

Figure 2.1: Rectangular cavity resonator (a) Electric field variation. The electric field is parallel to the shortest edge of the rectangle, with the number of anti-nodes in each direction indicating the mode. In this case $b < a < d$, the dominant mode is the TE_{101} mode. The magnetic field components circle in a perpendicular plane around the electric field maxima (not shown). (b) Cavity resonance spectrum and corresponding fit to the scattering parameter S_{11} in the complex plane measured in the single photon limit with $-140\,\mathrm{dBm}$ power applied at the SMA port. From the fit we obtain a resonance frequency $\omega_\mathrm{r}/2\pi = 5.239\,\mathrm{GHz}$, and Q factors $Q_\mathrm{l} = 3084.4$, $Q_\mathrm{c} = 5438.9$, and $Q_\mathrm{i} = 7124.9$. The resonator is used for the experiments in Sec. 7.2.

The cavity resonances are excited either capacitively to the electric field using the inner conductor of a coaxial cable, or inductively by a coupling loop penetrated by the magnetic field component. For resonances in the GHz regime the cavity

dimensions are in the range of mm to cm, large enough to store for example a magnetic bulk sample inside. Fabricating (and accessing) the cavity requires a cut in the design. This cut is made in parallel to the electric field to allow an undisturbed flow of electrons in the metallic walls.

2.1.1 Quality factors

The quality factors (Q factors) describe the losses of a resonator at the resonance frequency ω_0. In general a quality factor is defined as the ratio between the stored energy within the resonator E_{tot} and the energy loss rate P_{loss},

$$Q = \omega_0 \frac{E_{\mathrm{tot}}}{P_{\mathrm{loss}}} = \frac{\omega_0}{2\kappa}. \tag{2.3}$$

Here, κ is the half width at half maximum (HWHM) of the resonator's frequency response. There are three different quality factors in a resonator: The total loss of the resonator is described by the loaded quality factor Q_{l}. It is defined as the reciprocal sum of the coupling quality factor Q_{c} and the internal quality factor Q_{i},

$$Q_{\mathrm{l}}^{-1} = Q_{\mathrm{c}}^{-1} + Q_{\mathrm{i}}^{-1}. \tag{2.4}$$

With Eq. (2.3) we find for the corresponding linewidths,

$$\kappa_{\mathrm{l}} = \kappa_{\mathrm{c}} + \kappa_{\mathrm{i}}. \tag{2.5}$$

2.1.2 Scattering parameters

We describe the measurement signal of our resonator by a scattering matrix that contains the reflection coefficient $r(\omega)$ of a probe signal with frequency ω to our resonator, which is capacitively coupled via a coaxial cable to the outside world. The components of the scattering matrix for any generic multiport microwave network relate the amplitude and phase of the signal reflected from port i to the incoming signal of port j,

$$S_{ij} = \frac{V_i^{\mathrm{out}}}{V_j^{\mathrm{in}}}. \tag{2.6}$$

Our resonator has only one port, the reflection coefficient here is the ratio between the outgoing and the incoming voltage signal,

$$r(\omega) = S_{11} = \frac{V_{\mathrm{out}}(\omega)}{V_{\mathrm{in}}(\omega)}. \tag{2.7}$$

We model a lossless resonator by an impedance Z_r that is coupled to an open-ended transmission line with a characteristic impedance Z_0 describing the coaxial cable. Following Refs. [77–80], the charge of the input capacitor plate of the probed resonator is described by a harmonic oscillator that is driven by the incoming waves and damped by the transmission line with damping rate $2\kappa_\mathrm{c} = Z_0/L_\mathrm{r}$, with L_r being the resonator inductance. We find the reflection parameter depending on both impedances

$$r(\omega) = \frac{Z_\mathrm{r}(\omega) - Z_0}{Z_\mathrm{r}(\omega) + Z_0}. \tag{2.8}$$

The resonator impedance near the resonance frequency ω_r is approximated to be

$$Z_\mathrm{r}(\omega) \approx 2\mathrm{j}L_0(\omega - \omega_\mathrm{r}) \tag{2.9}$$

and we find the reflection coefficient

$$r(\omega) = S_{11}(\omega) = \frac{\omega - \omega_\mathrm{r} + \mathrm{j}\kappa_\mathrm{c}}{\omega - \omega_\mathrm{r} - \mathrm{j}\kappa_\mathrm{c}} \tag{2.10}$$

$$= 1 - \frac{2\kappa_\mathrm{c}}{\mathrm{j}(\omega - \omega_\mathrm{r}) + \kappa_\mathrm{c}}. \tag{2.11}$$

The internal losses in the cavity κ_i are accounted for by a complex renormalization of the resonator frequency $\omega_\mathrm{r} \to \omega_\mathrm{r} + \mathrm{j}\kappa_\mathrm{i}$ [81], leaving

$$S_{11} = 1 - \frac{2\kappa_\mathrm{c}}{\mathrm{j}(\omega - \omega_\mathrm{r}) + \kappa_\mathrm{i} + \kappa_\mathrm{c}} = 1 - \frac{2\kappa_\mathrm{c}}{\mathrm{j}(\omega - \omega_\mathrm{r}) + \kappa_\mathrm{l}} \tag{2.12}$$

This allows us to fit the experimental resonance data and characterize a resonator by its resonance frequency and Q factors. We fit the complex reflection coefficient with a circle [82, 83], see Fig. 2.1 (b). The derivation based on the circuit impedances employs the usual electrical engineering sign conversions with the imaginary unit $\mathrm{j} = -\mathrm{i}$ [79], in contrast to the derivation by the input-output formalism which uses the physics notation with the imaginary unit i. We will use the input-output formalism later to describe our coupled systems (Secs. 2.3.1 and 4.2).

2.1.3 Average photon population

The Q factors allow us to estimate the average photon population $\langle n \rangle$ in the resonator by a general power balance of incoming, outgoing, and lost power,

$$P_\mathrm{out} = P_\mathrm{in} - P_\mathrm{loss}. \tag{2.13}$$

With the absolute squared scattering parameter defined to be $|S_{11}|^2 = \frac{P_{\text{out}}}{P_{\text{in}}}$ and the internal Q factor $Q_{\text{i}} = \omega_0 \frac{E_{\text{tot}}}{P_{\text{loss}}} = \hbar\omega_0^2 \frac{\langle n \rangle}{P_{\text{loss}}}$ we find

$$\langle n \rangle = Q_{\text{i}} \frac{P_{\text{loss}}}{\hbar\omega_{\text{r}}^2} = Q_{\text{i}} P_{\text{in}} \frac{1 - |S_{11}|^2}{\hbar\omega_{\text{r}}^2}. \tag{2.14}$$

Evaluating $|S_{11}|^2$ on resonance we find

$$\langle n \rangle = 4 \frac{Q_{\text{l}}^2}{Q_{\text{c}}} \frac{P_{\text{in}}}{\hbar\omega_{\text{r}}^2}. \tag{2.15}$$

P_{in} here is in units of watt, in contrast to the usual dBm used throughout the thesis. Converting the power in Eq. (2.15) into the power level $L_P = 10 \log_{10} \left(\frac{P}{1\,\text{mW}} \right)$ with units dBm we find

$$\left\langle n \left(L_{P_{\text{in}}} \right) \right\rangle = 2 \frac{Q_{\text{l}}^2}{Q_{\text{c}}} \frac{1}{\hbar\omega_{\text{r}}^2} 10^{\frac{L_P}{10}} \cdot 10^{-6}\,\text{W}. \tag{2.16}$$

2.2 Collective magnetic excitations

Magnetic excitations in macroscopic ferromagnetic sample spread across the whole sample and manifest as collective excitation. Similar to phonons they are described as waves. Instead of exciting the crystal lattice, magnetic excitations form spin waves that describe the dynamic eigenmodes of the magnetization in a magnetically ordered medium [84]. Classically, spin waves represent collective, phase-coherent precessional motion of magnetic moments, see Fig. 2.2 that are quantized with their associated quasiparticles called magnons [40, 41]. In the magnetic ground state all spins in the lattice are in parallel. While an excitation can be assumed as one spin at one lattice site j being flipped, this is not an eigenstate of the Heisenberg Hamiltonian for quantum mechanical magnetic exchange interaction, which is based on the Pauli principle. Instead of a single spin flip, a lower-energy delocalized state is excited that is described by a linear combination of all possible spin flips. We describe an ensemble of N_{s} spins in a static external field $\boldsymbol{B} \parallel \boldsymbol{e}_z$ by

$$\hat{H} = -g^\star \mu_{\text{B}} B_z \sum_i^{N_{\text{s}}} \hat{S}_i^z - 2J \sum_{\langle i,j \rangle} \hat{\mathbf{S}}_i \cdot \hat{\mathbf{S}}_j, \tag{2.17}$$

where $g^\star$ is the g-factor, μ_{B} the Bohr magneton, and $\hat{\mathbf{S}}_i$ the spin operator of the ith spin [85, 86]. The first term describes a dipolar Zeeman coupling and the second term the nearest neighbor coupling with exchange coupling $J > 0$ in the ferromagnetic case.

We employ the Holstein-Primakoff transformation [40] to map the spin operators $\hat{\mathbf{S}}_i$ to bosonic creation and annihilation operators $\hat{m}^\dagger$ and $\hat{m}$, quantifying the number of magnetic excitation quasiparticles. Magnons are bosonic eigenstates of a magnetic quantum harmonic oscillator with the number of magnons corresponding to the reduction of the z-component of the total spin (see Fig. 2.3), resulting in a maximum of $2s$ magnons. We find the spin component operators

$$\hat{S}_i^+ = \hat{S}_i^x + \mathrm{i}\hat{S}_i^y = \sqrt{2s - \hat{m}_i^\dagger \hat{m}_i}\, \hat{m}_i, \tag{2.18}$$

$$\hat{S}_i^- = \hat{S}_i^x - \mathrm{i}\hat{S}_i^y = \hat{m}_i^\dagger \sqrt{2s - \hat{m}_i^\dagger \hat{m}_i}, \text{ and} \tag{2.19}$$

$$\hat{S}_i^z = s - \hat{m}_i^\dagger \hat{m}_i, \tag{2.20}$$

with spin s on each lattice site i and commutators $\left[\hat{m}_i,\, \hat{m}_{i'}^\dagger\right] = \delta_{ii'}$ [87].

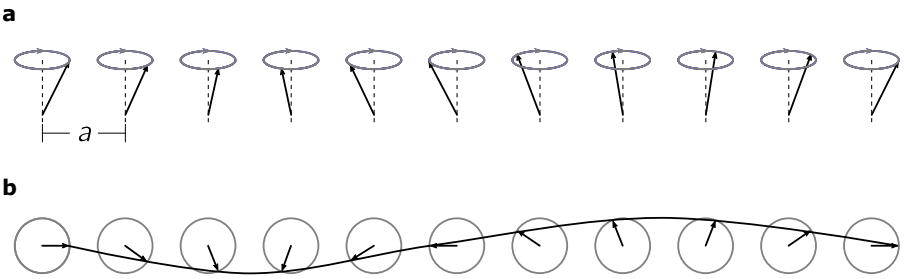

Figure 2.2: Spin wave on a line of spins The spin excitation spreads over the crystal and all spins precess around their equilibrium position forming a spin wave. The picture shows an exemplary spin wave with one wavelength in perspective (a) and from above (b).

Inserting the spin operators into the ferromagnetic Hamiltonian, taking all terms into the quadratic order of the bosonic operators, and Fourier transforming them into momentum space simplifies the ferromagnetic Hamiltonian to

$$\hat{H} = \sum_{\boldsymbol{k}} \hbar\omega_{\mathrm{m}}\left(\boldsymbol{k}\right) \hat{m}_{\boldsymbol{k}}^\dagger \hat{m}_{\boldsymbol{k}}, \tag{2.21}$$

with the wave vector of the spin-wave mode $\boldsymbol{k}$ and the magnon dispersion relation $\omega_{\mathrm{m}}\left(\boldsymbol{k}\right)$ [85, 86] with neglected constant ground state energy E_0. Considering only nearest neighbour interactions and a simple cubic lattice simplifies the dispersion relation in the long-wavelength limit to [66]

$$\hbar\omega_{\mathrm{m}}\left(\boldsymbol{k}\right) \approx g^\star \mu_{\mathrm{B}} B_z + 2sJa_0^2 \left|\boldsymbol{k}\right|^2, \tag{2.22}$$

with the lattice constant a_0. The contribution of the exchange interaction becomes negligible in the limit $a_0 \left|\boldsymbol{k}\right| \ll 1$ and the magnon modes correspond to magnetostatic

modes generated by magnetization oscillation obeying the Landau-Lifshitz-Gilbert equation

$$\frac{\mathrm{d}\boldsymbol{M}}{\mathrm{d}t} = -\gamma \left(\boldsymbol{M} \times \boldsymbol{H}_{\mathrm{eff}} - \frac{\alpha\gamma}{M_{\mathrm{s}}} \boldsymbol{M} \times \frac{\mathrm{d}\boldsymbol{M}}{\mathrm{d}t} \right), \tag{2.23}$$

with the magnetization $\boldsymbol{M}$, the saturation magenetization M_{s}, the effective field $\boldsymbol{H}_{\mathrm{eff}}$, the electron gyromagnetic ratio γ, and the Gilbert damping factor α. For spheroidal samples the modes were solved by Walker [88–90] and in the simplest Walker mode, the Kittel mode [91], all spins precess uniformly in phase with the same amplitude. This reduces Eq. (2.21) to

$$\hat{H} = \hbar\omega_{\mathrm{m}} \hat{m}^{\dagger} \hat{m}, \tag{2.24}$$

$$\text{with } \omega_{\mathrm{m}} = \frac{g^{\star}\mu_{\mathrm{B}}}{\hbar} B_z. \tag{2.25}$$

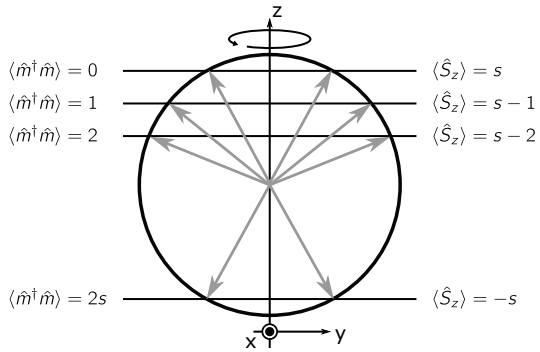

Figure 2.3: Holstein-Primakoff transformation Using the Holstein-Primakoff transformation the collective magnetic excitations are described as bosonic quasiparticles, which are distributed over the whole lattice. The number of magnons $\langle \hat{m}^{\dagger}\hat{m} \rangle$ corresponds to the reduced z-component of the spin quantum number. Inspired by [66].

A Kittel mode magnon corresponds to one single excited spin 1/2 particle in the field B_z, magnons in the macroscopic sample are therefore approximated by a single macrospin. The quantum harmonic oscillator approximation of Kittel mode magnons in the magnetostatic limit is only valid if the number of excited magnons is much smaller than the total number of participating spins, comparable to a small-angle approximation. We are able to tune the magnon frequency by applying a homogeneous magnetic field $\omega_{\mathrm{m}} \propto B_z$, and excite the magnon by a magnetic field oscillating with ω_{m} perpendicular to B_z. A non-uniform ac field results in higher order magnetostatic modes being excitable as well, which can be excited eiter voluntarily [54, 70] or as an involuntary effect [53, 61, 62, 65, 76] together with the Kittel mode.

2.3 Magnetic dipole interaction: cavity and magnon

We describe the interplay between a magnetostatic mode and a microwave cavity mode by a magnetic dipole interaction. The cavity resonance modes are expressed by harmonic oscillator modes with resonance frequency ω_r and creator/annihilator operators $\hat{a}^\dagger/\hat{a}$,

$$\hat{H}_\mathrm{c} = \hbar\omega_\mathrm{r}\hat{a}^\dagger\hat{a}. \tag{2.26}$$

The interaction with the magnetic spins is given by a Zeeman-type interaction Hamiltonian

$$\begin{aligned}\hat{H}_{\mathrm{m-c}} &= g^\star\mu_\mathrm{B}\sum_i^{N_\mathrm{s}} \boldsymbol{B}\left(\boldsymbol{r}_i\right)\cdot\hat{\boldsymbol{S}}_i \\ &= g^\star\mu_\mathrm{B}\sum_i^{N_\mathrm{s}} \boldsymbol{\delta B}\left(\boldsymbol{r}_i\right)\cdot\hat{\boldsymbol{S}}_i\left(\hat{a}+\hat{a}^\dagger\right),\end{aligned} \tag{2.27}$$

with the microwave cavity magnetic field at position $\boldsymbol{r}_i$ of spin i, $\boldsymbol{B}\left(\boldsymbol{r}_i\right) = \boldsymbol{\delta B}\left(\boldsymbol{r}_i\right)\left(\hat{a}+\hat{a}^\dagger\right)$. Using the Holstein-Primakoff transformation, we replace the spin operator by the sum of of magnon operators $\hat{m}^\dagger$ and $\hat{m}$ multiplied by their orthonormal spatial mode functions $\boldsymbol{s}_n\left(\boldsymbol{r}_i\right)$ [66],

$$\hat{\boldsymbol{S}}_i = \sqrt{2s}\sum_n \boldsymbol{s}_n\left(\boldsymbol{r}_i\right)\frac{\hat{m}_n+\hat{m}_n^\dagger}{2}. \tag{2.28}$$

With the coupling strength g much smaller than the resonance frequencies we apply a rotating wave approximation and find

$$\hat{H}_{\mathrm{m-c}} = \frac{g^\star\mu_\mathrm{B}}{2}\sqrt{2s}\sum_n\int_V \mathrm{d}\boldsymbol{r}\,\boldsymbol{\delta B}\left(\boldsymbol{r}\right)\cdot\boldsymbol{s}_n\left(\boldsymbol{r}\right)\left(\hat{a}\hat{m}^\dagger+\hat{a}^\dagger\hat{m}\right) \tag{2.29}$$

$$= \sum_n \hbar g^{(n)}\left(\hat{a}\hat{m}^\dagger+\hat{a}^\dagger\hat{m}\right), \tag{2.30}$$

where V is the sample volume and $g^{(n)}$ the effective coupling strength between the magnetic mode n and the cavity mode.

In the special case of a microwave magnetic field $\boldsymbol{\delta B}\left(\boldsymbol{r}\right)$ uniformly distributed over the magnetic sample, only the Kittel mode leaves a non-vanishing contribution to the integral over the N_s spins within the sample volume. Using the average single spin coupling strength $\bar{g}$ for all participating spins we find a $\sqrt{N_\mathrm{s}}$ enhancement

compared to the single spin coupling, $\bar{g} = \sqrt{\sum_i |g(\boldsymbol{r}_i)|^2 / N_\mathrm{s}}$ [92, 93]. The interaction Hamiltonian and the coupling strength are given by

$$\hat{H}_{\mathrm{m-c}} = \hbar g \left(\hat{a}\hat{m}^\dagger + \hat{a}^\dagger \hat{m} \right) \text{ and} \tag{2.31}$$

$$g = \frac{g^\star \mu_\mathrm{B}}{2\hbar} |\delta \boldsymbol{B}(\boldsymbol{r})| \sqrt{2N_\mathrm{s} s}, \tag{2.32}$$

with the amplitude of the vacuum fluctuations $|\delta \boldsymbol{B}(\boldsymbol{r}_i)|$. This Hamiltonian represents the Tavis-Cummings model, which describes the interaction of multiple identical two-state systems with a single quantum field mode [94]. The collectively enhanced coupling strength accounts for the fact that a single magnon excitation is shared between all participating spins. The coherent superposition of the N_s identical spins are called Dicke states [95]. The magnetic field at point $\boldsymbol{r}$ in the cavity mode is given by [96, 97]

$$\boldsymbol{B}_\mathrm{c} = \mathrm{i} |\delta \boldsymbol{B}(\boldsymbol{r})| \left(\boldsymbol{f}(\boldsymbol{r}) \hat{a} - \boldsymbol{f}^\star(\boldsymbol{r}) \hat{a}^\dagger \right), \tag{2.33}$$

with a dimensionless vector function $\boldsymbol{f}$ describing the spatial structure of the magnetic field mode. This gives a cavity ground state energy

$$\langle 0| \int \frac{1}{\mu_0} |\boldsymbol{B}_\mathrm{c}|^2 \, \mathrm{d}^3\boldsymbol{r} |0\rangle = \frac{\hbar\omega_\mathrm{r}}{2} \tag{2.34}$$

$$\langle 0| \frac{1}{\mu_0} |\delta \boldsymbol{B}|^2 V_\mathrm{mode} |0\rangle = \frac{\hbar\omega_\mathrm{r}}{2} \tag{2.35}$$

$$\Rightarrow |\delta \boldsymbol{B}| = \sqrt{\frac{\mu_0 \hbar \omega_\mathrm{r}}{2V_\mathrm{mode}}} \tag{2.36}$$

with the effective magnetic mode volume $V_\mathrm{mode} = \int |\boldsymbol{f}(\boldsymbol{r})|^2 \, \mathrm{d}^3\boldsymbol{r}$. The overlap between the magnetostatic and the electromagnetic microwave mode is accounted for by an additional factor that $\eta = \sqrt{(B_x^2 + B_z^2) / \max\left\{ |\boldsymbol{B}|^2 \right\}}$ [53, 98], with the xz plane being in parallel to the cavity cut described in Sec. 5.3. The magnon-photon coupling is given by

$$g = \frac{\gamma_\mathrm{e} \eta}{2} \sqrt{\frac{\mu_0 \hbar \omega_\mathrm{r}}{2V_\mathrm{mode}}} \sqrt{2Ns}, \tag{2.37}$$

with the gyromagnetic ratio of the electron $\gamma_\mathrm{e} = g^\star \mu_\mathrm{B} / \hbar$.

Similar to the pure cavity resonator measurements we probe our coupled magnon-photon hybrid system with microwaves and record the reflection spectrum S_{11}. We describe the hybrid system in the Tavis-Cummings model with the Holstein-Primakoff transformation by two coupled harmonic oscillators, Eqs. (2.24), (2.26), and (2.31),

$$\hat{H}_\mathrm{sys} = \hbar\omega_\mathrm{r} \hat{a}^\dagger \hat{a} + \hbar\omega_\mathrm{m} \hat{m}^\dagger \hat{m} + \hbar g \left(\hat{a}\hat{m}^\dagger + \hat{a}^\dagger \hat{m} \right), \tag{2.38}$$

that is used to derive an analytic model for the measured reflection spectrum of the system.

While the Tavis-Cummings model does include the magnon and photon excitation number operators, we work in the first part of this thesis in a purely classical regime, where such a quantum description of the cavity magnon polariton would not be necessary. The model becomes important in Chaps. 4 and 8, where the superconducting qubit as the non-linear circuit element is introduced.

A second, more intuitive approach to magnon-photon coupling treats the system as two coupled harmonic oscillators similar to classical physics lectures. Here, we find an eigenvalue equation of two coupled harmonic oscillators in matrix form [51]

$$\begin{pmatrix} \omega - \tilde{\omega}_\mathrm{r} & g \\ g & \omega - \tilde{\omega}_\mathrm{m} \end{pmatrix} \cdot \begin{pmatrix} x_1 \\ x_2 \end{pmatrix} = 0, \tag{2.39}$$

with constant coupling strength g and the frequencies of the photon and magnon, $\tilde{\omega}_\mathrm{r}$ and $\tilde{\omega}_\mathrm{m}$ respectively, which include complex damping terms. We make a classical rotating wave approximation, where we neglect higher order terms in ω and find the eigenfrequencies of the coupled system in the vicinity of zero detuning

$$\omega_\pm (I) = \frac{\tilde{\omega}_\mathrm{r} + \tilde{\omega}_\mathrm{m} (I)}{2} \pm \sqrt{\frac{\left(\tilde{\omega}_\mathrm{r} - \tilde{\omega}_\mathrm{m} (I)\right)^2}{4} + g^2}. \tag{2.40}$$

We fit the measured dressed frequencies to obtain the bare cavity frequency and the current dependent magnon frequencies as well as the coupling strength.

There is also a third description model of the magnon-photon coupling based on the electromagnetic viewpoint, which reveals best the underlying physics and is the basis of phase coherent effects such as spin-pumping [99], dynamic control of the coupling strenght [100, 101] or coherent time control [102]. However, this treatment of the coupled system is not relevant for the experiments performed during this thesis.

2.3.1 Derivation of the coupled reflection spectrum

We connect the system by coaxial cables to the outside world in order to probe the it with microwaves and measure the reflection spectrum. The probing of the system Hamiltonian is modeled by a bath of photons in the microwave feed line and an interaction term of the bath with the cavity photons where we consider only one

single mode within the cavity and no direct coupling between the bath photons and the magnon excitations (see Fig. 2.4),

$$\hat{H} = \hat{H}_{\text{sys}} + \hat{H}_{\text{bath}} + \hat{H}^{\text{int}}_{\text{bath}}, \tag{2.41}$$

$$\hat{H}_{\text{bath}} = \int_{\infty}^{\infty} \mathrm{d}\omega\, \hbar\omega \hat{b}^{\dagger}_{\omega} \hat{b}_{\omega}, \tag{2.42}$$

$$\hat{H}^{\text{int}}_{\text{bath}} = -\mathrm{i}\hbar \int_{-\infty}^{\infty} \mathrm{d}\omega\, c_{\omega} \left(\hat{b}^{\dagger}_{\omega} \hat{a} - \hat{a}^{\dagger} \hat{b}_{\omega} \right). \tag{2.43}$$

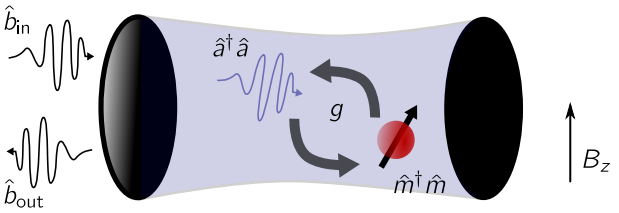

Figure 2.4: Hybrid system probing scheme The coupled cavity photon - magnon system is probed in reflection. The reflection spectrum is modeled with a continuous bath of photons in the feed line that couple only to the cavity photon mode. The excitation is then swapped to the magnon via dipolar exchange coupling.

The interaction with the external bath is purely imaginary, since it acts as an additional source of dissipation for the cavity photons and has a negative sign to ensure a Hermitian Hamiltonian [51]. We employ the input-output formalism [103] and find the field operators for the incoming and outgoing probe field to calculate the reflection spectrum

$$S_{11} = \frac{\hat{b}_{\text{out}}}{\hat{b}_{\text{in}}}. \tag{2.44}$$

From the Heisenberg equations of motion for the field operators

$$\frac{\mathrm{d}\hat{b}_{\omega}}{\mathrm{d}t} = -\frac{\mathrm{i}}{\hbar} \left[\hat{b}_{\omega}, \hat{H} \right] = -\mathrm{i}\omega \hat{b}_{\omega} + c_{\omega} \hat{a} \tag{2.45}$$

$$\frac{\mathrm{d}\hat{a}}{\mathrm{d}t} = -\frac{\mathrm{i}}{\hbar} \left[\hat{a}, \hat{H} \right] = -\frac{\mathrm{i}}{\hbar} \left[\hat{a}, \hat{H}_{\text{sys}} \right] - \int_{-\infty}^{\infty} \mathrm{d}\omega\, c_{\omega} \hat{b}_{\omega} \tag{2.46}$$

$$\frac{\mathrm{d}\hat{m}}{\mathrm{d}t} = -\frac{\mathrm{i}}{\hbar} \left[\hat{m}, \hat{H} \right] = -\frac{\mathrm{i}}{\hbar} \left[\hat{m}, \hat{H}_{\text{sys}} \right] \tag{2.47}$$

we find by solving Eqs. (2.45) and (2.45) for a time t_0 in the past

$$\hat{b}_\omega = \hat{b}_\omega(t_0)\, e^{-\mathrm{i}\omega(t-t_0)} + \int_{t_0}^{t} \mathrm{d}t'\, c_\omega e^{-\mathrm{i}\omega(t-t')} \hat{a}\left(t'\right) \tag{2.48}$$

$$\frac{\mathrm{d}\hat{a}}{\mathrm{d}t} = -\frac{\mathrm{i}}{\hbar}\left[\hat{a},\, \hat{H}_{\mathrm{sys}}\right] - \int_{-\infty}^{\infty} \mathrm{d}\omega\, c_\omega e^{-\mathrm{i}\omega(t-t_0)} \hat{b}_\omega(t_0) - \int_{-\infty}^{\infty} \mathrm{d}\omega \int_{t_0}^{t} \mathrm{d}t'\, |c_\omega|^2\, e^{-\mathrm{i}\omega(t-t')} \hat{a}\left(t'\right). \tag{2.49}$$

The last term in Eq. (2.49) describes the coupling from the bath into the cavity that is given by the corresponding linewidth κ_c. Using Fermi's golden rule we identify

$$2\kappa_\mathrm{c}(\omega_\mathrm{r}) = 2\pi \int \mathrm{d}\omega\, |c_\omega|^2\, \delta(\omega_\mathrm{r} - \omega). \tag{2.50}$$

Employing the Markov approximation, we assume a constant coupling over a frequency range close to resonance and find $c_\omega \approx c = \sqrt{\kappa_\mathrm{c}/2\pi}$. The remaining integrals give a δ function and a factor $2\pi/2$. We identify the second term in Eq. (2.49) with the incoming photon mode [104–106]

$$\hat{b}_{\mathrm{in}}(t) = -\frac{1}{\sqrt{2\pi}} \int_{-\infty}^{\infty} \mathrm{d}\omega\, e^{-\mathrm{i}\omega(t-t_0)} \hat{b}_\omega(t_0). \tag{2.51}$$

Choosing different boundary conditions for the time integral in Eq. (2.48) and defining an output mode with opposite sign compared to Eq. (2.51) we find two solutions for the equation of motion of the cavity operator

$$\frac{\mathrm{d}\hat{a}}{\mathrm{d}t} = -\frac{\mathrm{i}}{\hbar}\left[\hat{a},\, \hat{H}_{\mathrm{sys}}\right] + \sqrt{2\kappa_\mathrm{c}}\hat{b}_{\mathrm{in}} - \kappa_\mathrm{c}\hat{a} \tag{2.52}$$

$$\frac{\mathrm{d}\hat{a}}{\mathrm{d}t} = -\frac{\mathrm{i}}{\hbar}\left[\hat{a},\, \hat{H}_{\mathrm{sys}}\right] - \sqrt{2\kappa_\mathrm{c}}\hat{b}_{\mathrm{out}} + \kappa_\mathrm{c}\hat{a}, \tag{2.53}$$

and the relation of the incoming and outgoing field operators

$$\hat{b}_{\mathrm{in}}(t) + \hat{b}_{\mathrm{out}}(t) = \sqrt{2\kappa_\mathrm{c}}\hat{a}(t). \tag{2.54}$$

This gives a set of two equations for the photon operator, Eq. (2.52), and magnon operator Eq. (2.47),

$$\frac{\mathrm{d}\hat{a}}{\mathrm{d}t} = \left(-\mathrm{i}\omega_\mathrm{r} - \frac{\kappa_\mathrm{c}}{2}\right)\hat{a}(t) - \mathrm{i}g\hat{m}(t) + \sqrt{2\kappa_\mathrm{c}}\hat{b}_{\mathrm{in}}(t) \tag{2.55}$$

$$\frac{\mathrm{d}\hat{m}}{\mathrm{d}t} = -\mathrm{i}\omega_\mathrm{m}\hat{m}(t) - \mathrm{i}g\hat{a}(t). \tag{2.56}$$

We Fourier transform the operators into frequency space, leaving a factor of $-\mathrm{i}\omega$ on both left sides and solve the set of equations for $\hat{a}(\omega)$,

$$\hat{a}(\omega) = \frac{\sqrt{2\kappa_\mathrm{c}}}{\mathrm{i}(\omega_\mathrm{r} - \omega) + \kappa_\mathrm{c} + \frac{g^2}{\mathrm{i}(\omega_\mathrm{m} - \omega)}} \hat{b}_{\mathrm{in}}(\omega). \tag{2.57}$$

With the input-output relation in Eq. (2.54) we find the reflection spectrum of the coupled harmonic oscillator system

$$S_{11}(\omega) = \frac{\hat{b}_{\text{out}}(\omega)}{\hat{b}_{\text{in}}(\omega)} = -1 + \frac{2\kappa_{\text{c}}}{\mathrm{i}(\omega_{\text{r}} - \omega) + \kappa_{\text{c}} + \frac{g^2}{\mathrm{i}(\omega_{\text{m}} - \omega)}}. \tag{2.58}$$

Analog to Sec. 2.1.2 we introduce internal losses in the cavity and magnetic system by a complex renormalization of the resonance frequencies, $\omega_{\text{r}} \to \omega_{\text{r}} - \mathrm{i}\kappa_{\text{i}}$ and $\omega_{\text{m}} \to \omega_{\text{m}} - \mathrm{i}\kappa_{\text{m}}$ [81] and find the reflection spectrum in the general case

$$S_{11}(\omega) = -1 + \frac{2\kappa_{\text{c}}}{\mathrm{i}(\omega_{\text{r}} - \omega) + \kappa_{\text{l}} + \frac{g^2}{\mathrm{i}(\omega_{\text{m}} - \omega) + \kappa_{\text{m}}}}. \tag{2.59}$$

2.4 Yttrium iron garnet

We choose yttrium iron garnet ($Y_3Fe_5O_{12}$, YIG) as the magnetic material for all of our experiments. YIG, an insulating ferrimagnet, is the material of choice in many magnetism focused studies for its unparalleled low damping qualities and high Curie temperature of $T_{\text{C}} = 560\,\text{K}$.

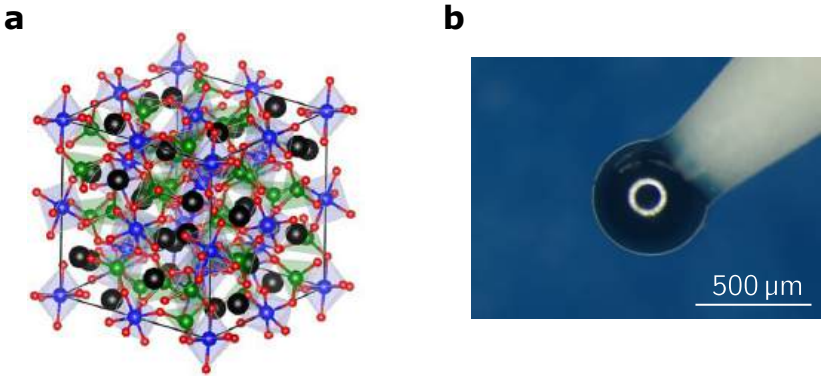

Figure 2.5: Crystal structure and photograph of YIG (a) Conventional unit cell of YIG, where black spheres are yttrium, red spheres are oxygen, and green and blue are iron atoms on two different lattice sites (tetrahedral and octahedral, respectively). From [107]. (b) Photograph of one of our used YIG sample. The white ring is an artifact, showing the reflection the lighting equipment.

While magnon lifetimes in pure iron or the alloy permalloy ($Ni_{81}Fe_{19}$) are on the order of nanoseconds [108, 109] and a spin-wave mean free path typically below 10 µm [110, 111], the low damping in YIG result in a lifetime of a few hundred nanoseconds and spin-wave propagation over centimeter distance.

These properties have led to a broad usage in research studying microwave magnetic dynamics [112], general wave dynamics [113], room temperature Bose-Einstein condensation [44], magnon logic elements [114], as well as cavity-based QED [115] optomagnonics [57], magnomechanics [116], and temperature dependent magnetization dynamics [117]. The low damping properties also resulted in the development of many analog microwave components such as filters, oscillators, and circulators based on YIG. YIG has a bcc lattice structure with 80 atoms per unit cell with a lattice constant of 12.4 Å. The structure is depicted in Fig. 2.5(a) and a zoomed photograph of our sample is shown in Fig. 2.5(b). The magnetic properties originate in the two different sites of the Fe^{3+} ions which, differin the configurations of the neighboring oxygen ions. This results in a strong magnetic exchange interaction, a magnetic moment of a unit cell of $10\,\mu_B$ at low temperatures [118], and an effective spin number $s = 5/2$ [53, 115]. Due to its complexity a lot of research has been spent on the crystal growth process leading to well established single crystal processes since YIG cannot be found naturally.

2.5 Magnetic losses

Employing magnons in hybrid quantum circuits requires their excitation lifetime to exceed the exchange time between system components. The excitation lifetime is represented by the magnon resonance linewidth, which quantifies excitation losses. Measuring excitation losses in magnetic materials has become a standard procedure for material characterization by comparing the magnetic resonance linewidth. Depending on the physics language, this is expressed either by measurements of δH, the linewidth of the magnetic resonance field at constant measurement frequency or by measurements of $\delta\omega$, the linewidth of the resonance frequency at constant magnetic field. The data can be converted between the two representations using

$$\delta H = \frac{\delta\omega}{\partial\omega_0/\partial H_0}, \tag{2.60}$$

with the differential $\partial\omega_0/\partial H_0$ representing the magnetic dispersion relation [119]. We choose the language of microwave engineering and use the resonance frequency linewidth $\delta\omega$ as the magnetic linewidth in this thesis, to which we refer to as κ_m. After the discovery of YIG in the late 1950s there have been multiple studies regarding the main underlying physical contribution to magnetic linewidth in different temperature regimes to further optimize the material quality. The most prominent contribution are found in material impurities, with other rare-earth (RE) elements replacing yttrium on a sample site, and scattering on the rough sample surface. At millikelvin temperatures, quantum defects in the form of two-level systems are found in YIG. Detailed experimental data is given in Chap. 7.

2.5.1 Slow-relaxing impurities

Below room temperature, the linewidth in YIG increases with decreasing temperature, showing a peak between 40 K and 150 K [120–122]. This increase is explained by scattering at RE impurities within the YIG sample, the so called slow-relaxing impurities [119, 123, 124]. The two Fe^{3+} sublattices are strongly coupled and can be considered as one effective sublattice. RE ions that substitute on the yttrium sites couple to this effective sublattice with an exchange interaction about an order of magnitude smaller than the Fe^{3+}-Fe^{3+} exchange interaction [122]. The RE-RE coupling can be neglected for small impurity concentration. The effective Fe^{3+} sublattice couples to the non-interacting rare-earth ions individually. This coupling acts as a loss channel to the lattice for the uniform magnetic mode at a frequency ω, broadening the resonance linewidth.

The motion of the magnetization around the applied static magnetic field changes the exchange field acting on the parasitic RE ions. The time-dependent component parallel to the RE ion spin modulates their Zeeman energy splitting from the unperturbed frequency Ω, the thermal equilibrium population changes, and the system relaxes back to equilibrium by energy level transitions. Due to the finite impurity relaxation time there is a time delay between transition frequency and equilibrium population, which results in the magnetic excitation loss. We model the anisotropic exchange by assuming the impurities with only two energy levels, which approximates them as effective spin $1/2$ systems, with all impurity splittings at the same transition frequency Ω with relaxation rate τ. The linewidth due to slow-relaxing impurities κ_{RE} is found to be

$$\kappa_{\mathrm{RE}} \propto \frac{1}{T} \frac{\exp\left(\hbar\Omega/k_{\mathrm{B}}T\right)}{\left[\exp\left(\hbar\Omega/k_{\mathrm{B}}T\right)+1\right]^2} \frac{\omega\tau}{\tau^2+\omega^2}, \tag{2.61}$$

with a typical impurity frequency on the order of $\Omega/2\pi \sim 2\,\mathrm{THz}$ [119]. Considering a thermal equilibrium population of the impurities

$$n_{\mathrm{th}} = \frac{1}{\exp\left(\hbar\omega/k_{\mathrm{B}}T\right)+1}, \tag{2.62}$$

the effect of slow-relaxing RE impurities freezes out towards single digit kelvin temperatures.

2.5.2 Two-magnon scattering

The dominant relaxation process for the magnetic excitation of the uniform mode going towards liquid helium temperatures is found to be two-magnon scattering

processes in imperfections on the sample surface [125–127]. The "two-magnon" expression originates in the second quantization formalism, where the process can be modeled as a magnon in the uniform mode being destroyed and a $\boldsymbol{k} \neq 0$ mangon at the same frequency being created [128]. Because the number of magnons stays constant, so does the z-component of the macro spin, but the destruction of a uniform mode magnon reduces the total spin by one. This makes it a scattering process only for the transversal component of the magnetic moment. The pit-scattering theory of Sparks, Loudon, and Kittel considers scattering at spherical diamagnetic inclusions at the sample surface. The linewidth contribution due to surface scattering κ_{surface} for a spherical sample of radius r with pits of radius r_{pit} and the saturation magnetization M_{s} is well approximated by

$$\kappa_{\text{surface}} \propto \frac{\pi^2}{2} M_{\text{s}} \frac{r_{\text{pit}}}{r} \tag{2.63}$$

for the uniform precession mode [129].

2.5.3 Two-level systems

At temperatures reaching the millikelvin regime the dominant loss mechanism in amorphous solids are two-level systems (TLSs). This rather generic loss mechanism was first described in experiments at ultrasonic properties of glasses [130–132], but has also been successfully applied to describe decoherence and fluctuations in superconducting quantum circuits [133, 134]. Additionally, TLS effects were observed in micro- and nanomechanical resonators [135–137], within amorphous reflective coating in optical devices [138] or field effect transistors [139].

In the standard tunneling model a two-level system is described as a double-well potential with a small energy difference δ and a tunneling rate δ_0, sketched in Fig. 2.6. The origin of this loss mechanism is not based on impurities but rather on the amorphous structure of the material. The TLS exists in one of the states and can change its state either by thermal activation or quantum tunneling. The general TLS Hamiltonian

$$\hat{H} = \frac{1}{2} \begin{pmatrix} -\delta & \delta_0 \\ \delta_0 & \delta \end{pmatrix} \tag{2.64}$$

is written in the basis of its eigenstates with energy $E = \sqrt{\delta^2 + \delta_0^2}$ and the Pauli matrix $\hat{\sigma}_z = \begin{pmatrix} 1 & 0 \\ 0 & -1 \end{pmatrix}$ as

$$\hat{H} = \frac{1}{2} E \hat{\sigma}_z. \tag{2.65}$$

The excitation loss in a TLS can be understood as a scattering process. If excitation and TLS are close in energy there is a resonant absorption process that depends on the occupation of the TLS. The general temperature dependence of the resonance broadening due to TLSs can be obtained by looking at the occupation number difference of the two states.

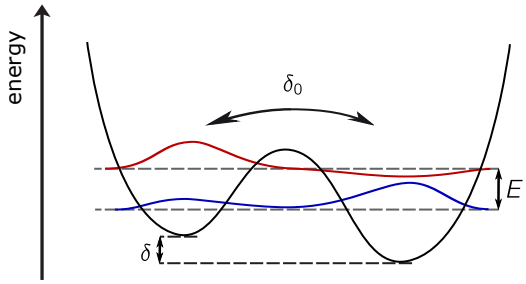

Figure 2.6: Double-well potential modeling a TLS The energy of the two states is given by the ground state energy difference δ and the tunneling rate δ_0. The barrier can be overcome by thermal excitation or quantum tunneling.

With the total density of TLSs n_{TLS}, the individual densities of TLSs in the lower and upper state, n_1 and n_2, and assuming a Boltzmann distributed occupation ratio between n_1 and state n_2, we find

$$n_{\mathrm{TLS}} = n_1 + n_2 \tag{2.66}$$

$$\frac{n_1}{n_2} = \exp\left(-E/k_{\mathrm{B}}T\right). \tag{2.67}$$

The TLS broadened resonance linewidth is proportional to the occupation number [131, 140],

$$\kappa_{\mathrm{TLS}} \propto \delta n = n_2 - n_1. \tag{2.68}$$

With Eqs. (2.66) and (2.67) we find

$$\kappa_{\mathrm{TLS}} \propto \tanh\left(\frac{E}{2k_{\mathrm{B}}T}\right). \tag{2.69}$$

For excitation frequencies ω in the single digit GHz range the TLSs saturate at temperatures above a few kelvin, $\hbar\omega \approx k_{\mathrm{B}}T$. The TLS occupation is not only dependent on temperature but also on excitation power P. The Hamiltonian in Eq. (2.65) is expanded by an interacting Hamiltonian modeling a drive field with transversal and longitudinal components. This system is equivalent to a spin 1/2 particle in a magnetic field

$$\hat{H} = -\hbar\gamma\left(\boldsymbol{B_0} + \boldsymbol{B}^{\mathrm{int}}\right)\cdot\boldsymbol{S}, \text{ with } \frac{\mathrm{d}}{\mathrm{d}t}\boldsymbol{S} = \gamma\boldsymbol{S}\times\left(\boldsymbol{B_0} + \boldsymbol{B}^{\mathrm{int}}\right). \tag{2.70}$$

with a gyromagnetic ratio γ. This gives the well known Bloch equations [141] for the expectation values of the individual spin components. Calculating the magnetic susceptibilities using

$$S_i(t) \propto \hbar\gamma B_i^{\text{int}}(t), \tag{2.71}$$

approximating a small amplitude in the interaction magnetic field, assuming only transverse coupling, and integrating the TLS energy with respect to the asymmetry, tunnel barrier and the transverse components we find an additional power dependent linewidth contribution [82, 142]

$$\kappa_{\text{TLS}} \propto \frac{1}{\sqrt{1+\frac{P}{P_{\text{c}}}}}, \tag{2.72}$$

with the critical power P_{c} at which the TLSs start to saturate. We obtain the total TLS linewidth contribution

$$\kappa_{\text{TLS}} = \kappa_{\text{TLS}}^0 \frac{\tanh\left(\frac{\hbar\omega}{2k_{\text{B}}T}\right)}{\sqrt{1+\frac{P}{P_{\text{c}}}}}, \tag{2.73}$$

where all material constants are combined into the not further specified linewidth κ_{TLS}^0.

The microscopic origin of TLSs in any system is still not yet fully understood and part of active research regarding its nature and position in amorphous oxides. The possible theories range from a literal movement of single tunneling atoms or a group of atoms [143], dangling OH bonds [144], electron tunneling [145] to spins and magnetic impurities [146–148].

3 Cavity quantum electrodynamics

The previous chapter describes a purely linear and classical hybrid system. In order to explore quantum features, we need an additional element in our system. This chapter introduces the needed nonlinearity, a superconducting transmon quantum bit (qubit). First, we give an introduction to the general concept of quantum bits and describe the concept of superconductivity and the Josephson effect, which makes our qubit nonlinear in the first place upon which our quantum bit is founded. After that, we elaborate the working principles and features of our superconducting qubit type, the transmon. The coupling of the quantum bit to the outside world via a microwave cavity photon concludes this chapter.

3.1 The quantum bit

A qubit is the quantum analogue to the classical binary bit, an artificial quantum mechanical two level system. The qubit is represented by its state vector $|\psi\rangle$, a superposition of ground and excited states $|\mathrm{g}\rangle$ and $|\mathrm{e}\rangle$, respectively,

$$|\psi\rangle = \alpha\,|\mathrm{g}\rangle + \beta\,|\mathrm{e}\rangle\,, \tag{3.1}$$

with normalized complex mixing coefficients α and β. The basis of the qubit eigenstates is spanned by $|\mathrm{g}\rangle$ and $|\mathrm{e}\rangle$, which can be represented by eigenvectors of the Pauli matrix $\hat{\sigma}_z$,

$$|\mathrm{g}\rangle = \begin{pmatrix} 0 \\ 1 \end{pmatrix},\ |\mathrm{e}\rangle = \begin{pmatrix} 1 \\ 0 \end{pmatrix},\ \text{and } \hat{\sigma}_z = \begin{pmatrix} 1 & 0 \\ 0 & -1 \end{pmatrix}. \tag{3.2}$$

With the qubit states quantized along the z-axis we find the creation and annihilation operators $\hat{\sigma}_\pm = \left(\hat{\sigma}_x \pm \mathrm{i}\hat{\sigma}_y\right)/2$, where $\hat{\sigma}_-\,|\mathrm{e}\rangle = |\mathrm{g}\rangle$.

Typically, the Bloch sphere representation is used to illustrate arbitrary qubit states, but also the impact of decoherence. Any pure qubit state $|\psi\rangle$ is represented by a point on the sphere surface characterized by a Bloch vector and corresponding Euler angles θ and φ,

$$|\psi\rangle = \cos\frac{\theta}{2}\,|\mathrm{g}\rangle + \sin\frac{\theta}{2}\mathrm{e}^{\mathrm{i}\varphi}\,|\mathrm{e}\rangle\,, \tag{3.3}$$

depicted in Fig. 3.1. In analogy to Sec. 2.5.3 we attribute a transition energy $\hbar\omega_q$ to the qubit states. The time evolution operator rotates a pure qubit state with the qubit frequency ω_q around the z-axis, resulting in a Larmor precession. Usually this rotation is accounted for by looking at the qubit Bloch vector from a rotating frame.

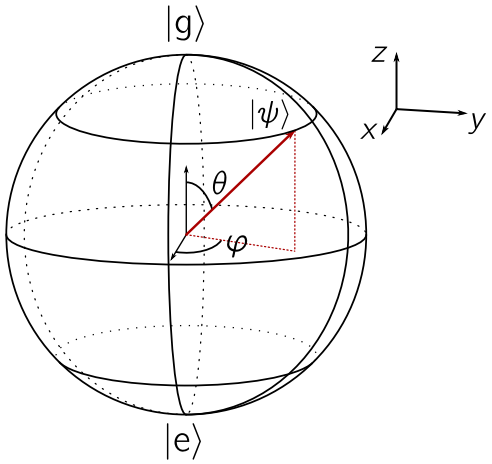

Figure 3.1: Qubit state on a Bloch sphere A pure qubit state $|\psi\rangle$ is represented by a point on the Bloch sphere's surface. The ground and excited state of the qubit are eigenvectors of $\hat{\sigma}_z$. By convention, the ground state is located on the Bloch sphere's positive pole. The Bloch vector of the qubit state is defined by the Euler angles θ and φ.

The qubit dynamics in the presence of energy relaxation and decoherene are described by the Lindblad master equation [96, 149] that results in the time evolution of a qubit state driven by a frequency ω_D. The two relevant decoherence mechanisms are the energy relaxation and pure dephasing. Energy relaxation acts on the qubit with the decay operator $\hat{L}_1 = \hat{\sigma}_-$, relaxing any excited state to the ground state at a rate Γ_1. Pure dephasing results in phase fluctuations of the Lamor precession in the equatiorial plane at a rate Γ_τ. Here, the decay operator is given by $\hat{L}_2 = \hat{\sigma}_z/\sqrt{2}$. In the Bloch sphere representation, the energy relaxation operator $\hat{\sigma}_-$ maps the $|e\rangle$-component of the state to the ground state eigenvector, while the dephasing operator describes a Larmor-type precession of the state around the quantization axis, describing the dynamics in the equatorial plane.

Solving the Lindblad equation [80] we find two characteristic time scales for the decoherences. $T_2^\star = 1/\Gamma_2^\star$ describes the timescale on which the qubit loses all phase information and $T_1 = 1/\Gamma_1$ is the energy relaxation time.. Neglecting pure dephasing, $\Gamma_\tau = 0$, we find the dephasing time limited by

$$T_2^\star \leq 2T_1. \tag{3.4}$$

The dephasing is measured by performing a Ramsey experiment [150], where the qubit is prepared in a state on the equatorial plane and rotated back on the quantization axis before reading out its state. Preparing the qubit state along the x-axis, the probability to find the qubit in its excited state after the second rotation decays exponentially with the dephasing rate $\Gamma_2^\star = \frac{1}{2}\Gamma_1 + \Gamma_\tau$, modulated by $\cos \Delta\omega t$ with $\Delta\omega = \omega_\mathrm{q} - \omega_\mathrm{D}$ with the drive frequency ω_D. The oscillation due to the frequency detuning $\Delta\omega \neq 0$ are referred to as Ramsey fringes.

Driving the qubit by an oscillating drive or pulse, its state vector rotates continuously between $|\mathrm{g}\rangle$ and $|\mathrm{e}\rangle$. The qubit drive is modeled by

$$\hat{H}_\mathrm{d} = \hbar\Omega_\mathrm{R} \cos(\omega_\mathrm{D} t)\, \hat{\sigma}_x, \tag{3.5}$$

with the Rabi frequency Ω_R [151]. Rotating the qubit state continuously allows us to calibrate pulse lengths required to prepare a specific state. Transforming the Hamiltonian into a frame rotating with the drive frequency and applying the rotating wave approximation by neglecting fast rotating terms, we find the probability to find the qubit in the ground state using

$$\mathcal{P}_{|\mathrm{g}\rangle} = \left| \langle \mathrm{g} \,|\, \hat{U}(t) \,|\, \mathrm{g} \rangle \right|^2 \tag{3.6}$$

with the time evolution operator in the rotating frame $\hat{U}(t)$. For zero detuning we find the ground state probability [152]

$$\mathcal{P}_{|\mathrm{g}\rangle}(\Delta\omega = 0) = \frac{1}{2}\left(1 + \cos \Omega_\mathrm{R} t\right). \tag{3.7}$$

The Rabi frequency increases with increasing drive power [153].

3.2 Superconductivity and Josephson junction

The transition from the concept and theoretical description of a qubit towards fabricating a measurable and controllable device that exhibits quantum coherence requires a manageable amount of effective degrees of freedom. We chose a solid state approach by using superconductors as our engineering platform for realizing a qubit. Superconductors essentially allow for a macroscopic quantum coherent flow of charge due to a long-range order parameter [154]. Although the typical implementation of a superconducting qubit has a spatial size on the mm length scale containing around 10^{15} atoms it is still possible to describe them with a single degree of freedom [79]. For the scope of this thesis it is sufficient to focus on the macroscopic phenomena of superconductors [155] without exploring the details

of the underlying microscopic description by the BCS theory, whose developer ultimately were awarded a Nobel prize in 1972 [156].

At a critical temperature T_c a superconductor undergoes a second-order phase transition where its electrons forms a Cooper pair condensate. Cooper pairs consist of two electrons with opposite spin and momentum, resulting in zero effective spin and a boson-like nature. The weak net attraction between the two usually repulsive electrons is mediated by an interaction with lattice phonons. The Cooper pairs undergo a Bose-Einstein condensation, leaving them in a macroscopic quantum state described by a single macroscopic wave function $\Psi(\mathbf{r}) = |\Psi| e^{i\varphi(\mathbf{r})}$ [85] with the collective phase $\varphi(\mathbf{r})$ and the amplitude $|\Psi|$ being related to the Cooper pair density. The flowing supercurrent is determined by the spatial dependence of φ and is a quantum coherent motion of the condensate as a whole. The Cooper pair condensate is broken by a finite pair breaking excitation 2Δ per Cooper pair as lowest possible excitation. Scattering processes below this minimal energy are prohibited, resulting in a non-dissipative current flox. This behavior was first observed in 1911 in mercury [157]. The scale of the gap is on the order of tens of GHz or several kelvin, i.e. for aluminium, $\Delta_{Al} \approx 41\,\mathrm{GHz}$ [85]. In addition to a vanishing electrical resistance a superconductor exhibits perfect diamagnetism [158], expelling magnetic fields from the bulk.

A strip of superconductor forms a harmonic LC oscillator similar to a metallic antenna. The resonance frequency (and higher harmonics) is determined by the spatial extension and the effective dielectric constant of the medium. The inductance and capacitance of such a system are given by a geometric part, storing energy in magnetic and electric fields and a kinetic part, storing energy in the motional degrees of freedom of the charge carriers. Frequent electron scattering in normal metals prevents the storage of any significant amount of kinetic energy, but due to the suppressed low-energy states in superconductors, the kinetic inductance term becomes more important, especially in non-uniform superconducting materials as oxidized aluminium [159–161]. Similar to the three dimensional cavity case in Sec. 2.1 we can couple superconducting resonators via their electromagnetic dipole moment to the outside world.

Connecting two superconductors by an insulating tunnel junction (see in Fig. 3.2(a)) leads to an overlap and hybridization of the two individual macroscopic wave functions due to tunneling effects. This ideal tunnel junction, together with the intrinsic capacitances of the electrodes, creates a Josephson junction [162] as depicted in Fig. 3.2(c). The Schrödinger equation for the hybridized wave function connects

the supercurrent across the barrier I_J with the superconducting phase difference $\phi = \varphi_1 - \varphi_2$ and the critical supercurrent I_c,

$$I_J = I_c \sin \phi \tag{3.8}$$

and connects the voltage drop across the junction V with the flux quantum $\Phi_0 = h/2e$,

$$V = \frac{\Phi_0}{2\pi} \frac{\mathrm{d}}{\mathrm{d}t} \phi. \tag{3.9}$$

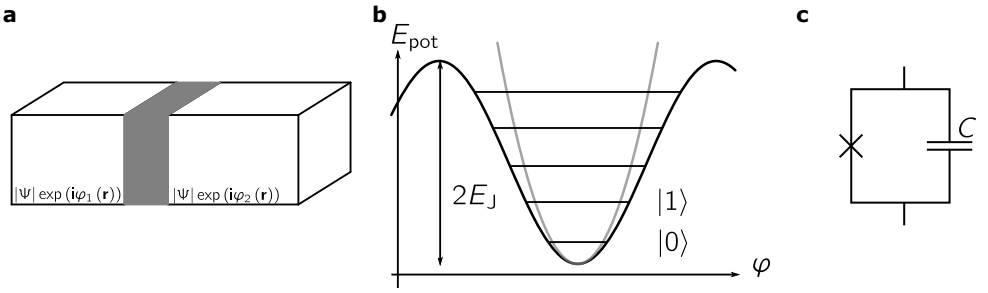

Figure 3.2: Josephson junction and anharmonic potential (a) Two superconducting electrodes connected by an insulating tunnel barrier form a Josephson junction. The current and voltage dynamics of the tunnel current are determined by the phase difference $\phi = \varphi_1 - \varphi_2$ leading to a nonlinear inductance. The amplitudes of both macroscopic wave functions are considered identical. (b) The non-linear inductance leads to an anharmonic potential and non-equidistant eigenenergies of the corresponding states of the oscillator. The energetically lowest states are used as the two levels of a superconducting qubit. A sketched harmonic potential shows the impact of the nonlinearity on the potential landscape. (c) Circuit diagram of a Josephson junction. The cross symbolizes the insulating tunnel junction, with the intrinsic self capacitance in parallel.

The Josephson junction allows for a zero-voltage supercurrent of Copper pairs to tunnel across the barrier, before the junction becomes resistive at a pair-breaking current I_c. Inserting the Josephson equations Eqs. (3.8) and (3.9) into the definition of the response of a inductor $V = -L\frac{\mathrm{d}I}{\mathrm{d}t}$ we obtain a non-linear inductance for the Josephson junction,

$$L_J(\phi) = \frac{\Phi_0}{2\pi I_c \cos \phi}. \tag{3.10}$$

The corresponding Josephson energy is given by

$$E_J = \frac{\hbar}{2e} I_c \tag{3.11}$$

and we find a charging energy $E_C = e^2/2C$, accounting for the isolated superconductors acting as a small capacitor. The sinusoidal inductance alters the total inductance

of the equivalent LC circuit and the energy levels of the corresponding oscillator become non-equidistant as depicted in Fig. 3.2(b). This anharmonic oscillator is the basis for superconducting qubits, where the lowest two energy levels are used as the ground and excited states of a qubit.

3.3 The transmon qubit

In this thesis we use a transmon qubit as the qubit type of choice. The transmon qubit [163] builds on the design of the single Cooper pair box (CPB) [14, 164] which consists of a superconducting island that is connected to a Cooper pair reservoir via a Josephson junction. Both, CPB and transmon qubit are described by the excess Cooper pairs $\hat{N}$ on the island and the superconducting phase $\hat{\phi}$ across the Josephson junction. The number operator is given by

$$\hat{N} = \sum_N N \left|N\right\rangle \left\langle N\right| \tag{3.12}$$

and its conjugate phase operator $\hat{\phi}$,

$$\left[\hat{N}, \hat{\phi}\right] = -\mathrm{i}. \tag{3.13}$$

The basis states are related via Fourier transformation

$$\left|N\right\rangle = \frac{1}{2\pi} \int_0^{2\pi} \mathrm{d}\phi \, \mathrm{e}^{-\mathrm{i}N\phi} \left|\phi\right\rangle \tag{3.14}$$

$$\left|\phi\right\rangle = \sum_{N=-\infty}^{\infty} \mathrm{e}^{\mathrm{i}N\phi} \left|N\right\rangle, \tag{3.15}$$

Cooper pair tunneling through the Josephson junction is described by [165]

$$\hat{H}_\mathrm{J} = -\frac{E_\mathrm{J}}{2} \sum_{N=-\infty}^{\infty} \left|N\right\rangle \left\langle N+1\right| + \left|N+1\right\rangle \left\langle N\right|, \tag{3.16}$$

where N is the number of Cooper pairs on one electrode connected to the Junction, later the island electrode. This allows to define a charge operator

$$\hat{Q} = -2e\hat{N}. \tag{3.17}$$

This results in the Josephson junction Hamiltonian from Eq. (3.16) to become

$$\begin{aligned} \hat{H}_\mathrm{J} &= -\frac{E_\mathrm{J}}{2} \frac{1}{2\pi} \int_0^{2\pi} \mathrm{d}\phi \, \left(\mathrm{e}^{\mathrm{i}\phi} + \mathrm{e}^{-\mathrm{i}\phi}\right) \left|\phi\right\rangle \left\langle \phi\right| \\ &= -E_\mathrm{J} \cos\hat{\phi} \end{aligned} \tag{3.18}$$

For the intrinsic Josephson junction capacitance we find

$$\hat{H}_{\mathrm{C}} = \frac{\hat{Q}^2}{2C} = 4E_{\mathrm{C}}\hat{N}^2. \tag{3.19}$$

This results in an effective Hamiltonian for the Josephson junction

$$\hat{H}_{\mathrm{JJ}} = \hat{H}_{\mathrm{J}} + \hat{H}_{\mathrm{C}} = 4E_{\mathrm{C}}\hat{N}^2 - E_{\mathrm{J}}\cos\hat{\phi}. \tag{3.20}$$

Transitioning to the CPB we introduce an additional term representing the offset charge n_g on the superconducting island and find a Hamiltonian similar to the single Josephson junction,

$$\hat{H} = 4E_{\mathrm{C}}\left(\hat{N} - n_{\mathrm{g}}\right)^2 - E_{\mathrm{J}}\cos\hat{\phi}. \tag{3.21}$$

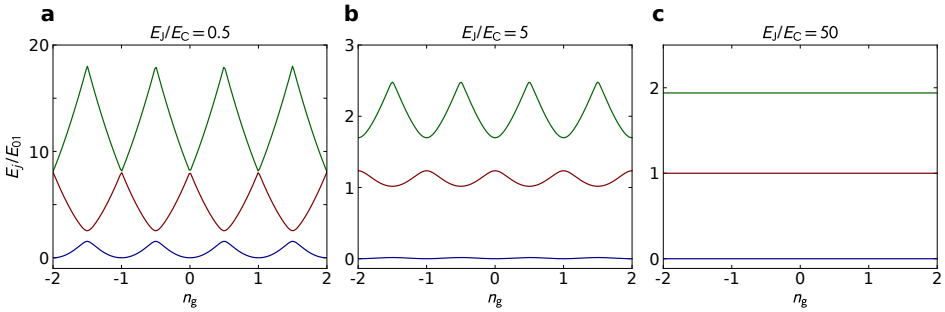

Figure 3.3: Qubit eigenenergy dispersions for different ratios $\mathbf{E_J/E_C}$ Eigenenergies E_m for $m = 0,\ 1,\ 2$ as a function of the offset charge n_g for different characteristic energy ratios E_J/E_C. The energies are normalized to the first transition energy E_{01} at the degeneracy point $n_g = 1/2$. (a) In the charge regime of the Cooper pair box, the transistion frequency is sensitive to changes in the offset charge, with charge sweet spots at half-integer n_g. In the transmon case (c), the charge dispersion flattens and the transition frequencies become insensitive to the offset charge. This comes with the cost of a reduced anharmonicity, described by a weak anharmonic potential. (b) shows the transition regime. Figure similar to [163].

Figure 3.3(a) shows color coded the lowest three eigenenergies E_j of the CPB. We treat the lowest two states as our qubit, with the qubit transition frequency being the energy difference between them. Usually, the CPB is biased to operate at half integer n_g, creating a coherent superposition of charge states.

With the parabolic energy dependence on the offset charge, the qubit frequency is sensitive to charge fluctuations. The transmon qubit was proposed to operate in a regime where the ratio of Josephson energy and charging energy is increased [163], $E_J/E_C \gtrsim 50$. This increased ratio reduces the anharmonicity (non-equidistant energy level spacing) but decreases the charge noise sensitivity. Figure 3.3 shows the

eigenenergies for the CPB Hamiltonian for different E_J/E_C ratios. For large ratios the charge dispersion is nearly flat and the qubit transition frequencies are effectively constant with respect to the offset charge. A transmon qubit design eliminates the need for a gate to tune the qubit into its charge sweet spot at half integer n_g to minimize noise effects. The large characteristic energy ratio is realized by adding a large shunt capacitance in parallel to the Josephson junction that increases the charging energy with $E_C \propto C^{-1}$. The CPB Hamiltonian, Eq. (3.21), is still valid, but with the dominant Josephson term the phase instead of the charge becomes the well-defined variable due to the uncertainty principle.

With the nearly harmonic energy level structure, the transmon resembles a simple harmonic LC-resonator where the inductance is replaced by the nonlinear Josephson junction. This nonlinearity creates a weakly anharmonic potential and allows the distinct excitation of the individual transitions. The transmon eigenstates and eigenenergies are approximated by expanding the cosine term in the potential energy up to fourth order in $\hat{\phi}$, which is valid for large E_J/E_C. The system resembles a harmonic oscillator with a quartic perturbation that describes the leading order anharmonicity,

$$\hat{H} = \sqrt{8E_C E_J}\left(\hat{b}^\dagger\hat{b} + \frac{1}{2}\right) - E_J - \frac{E_C}{12}\left(\hat{b} + \hat{b}^\dagger\right)^4, \tag{3.22}$$

with the approximated harmonic oscillator creation and annihilation operators, $\hat{b}$ and $\hat{b}^\dagger$. The eigenenergies are corrected in the leading quartic order by

$$E_j^{(1)} = -\frac{E_C}{12}\langle j|(\hat{b} + \hat{b}^\dagger)^4|j\rangle \simeq -\frac{E_C}{12}\left(6j^2 + 6j + 3\right), \tag{3.23}$$

where $|j\rangle$ are the purely harmonic oscillator states. The transmon eigenenergies of state m are approximated by

$$E_m \simeq -E_J + \sqrt{8E_C E_J}\left(m + \frac{1}{2}\right) - \frac{E_C}{12}\left(6m^2 + 6m + 3\right), \tag{3.24}$$

with the transition frequencies $E_{mn} = E_m - E_n$. As with the CPB, the lowest two states are used as our qubit two-level system. Overall, the transmon can be viewed as an artificial atom with multiple individual level transitions. The absolute transmon anharmonicity is given by the difference between the first two energy levels and is approximated by the charging energy,

$$\alpha = E_{12} - E_{01} \simeq -E_C, \tag{3.25}$$

with the relative anharmonicity

$$\alpha_r = -\sqrt{8E_J/E_C}. \tag{3.26}$$

3.4 Jaynes-Cummings model

For manipulation and readout, we couple the qubit via photons in the form of confined microwave cavity modes to the outside world. In general, this is described as light-matter interaction of an atom and a single resonator mode. In our experiments this is realized via the electric dipole of the transmon qubit, $\hat{\mathrm{d}} \propto \hat{\sigma}_x$, which is in parallel to the electric field of the cavity, $\hat{\mathrm{E}} \propto \hat{a}^\dagger + \hat{a}$. We find a coupling Hamiltonian

$$\hat{H}_\mathrm{c} = \hbar g \hat{\sigma}_x \left(\hat{a}^\dagger + \hat{a} \right) \tag{3.27}$$

that describes the transverse coupling between atom and resonator, with $\hat{\sigma}_x$ having only off-diagonal terms. Approximating the atom to only two levels with energy difference $\hbar\omega_{01}$ that interact with a single quantized mode of a microwave cavity at frequency ω_r we find the quantum Rabi Hamiltonian [151, 166]

$$\hat{H}/\hbar = \frac{1}{2}\omega_{01}\hat{\sigma}_z + \omega_\mathrm{r}\hat{a}^\dagger\hat{a} + g\hat{\sigma}_x \left(\hat{a}^\dagger + \hat{a} \right), \tag{3.28}$$

with creators/annihilators in the Fock space of the oscillator mode $\hat{a}^\dagger/\hat{a}$. The systems is usually described in a regime, where the coupling is small compared to the frequencies, $g \ll \omega_\mathrm{r}, \omega_{01}$. We use $\hat{\sigma}_\pm = 1/2\,(\hat{\sigma}_x \pm \hat{\sigma}_-)$ and apply a rotating wave approximation to Eq. (3.28) where we neglect the counter rotating terms proportional to $\hat{\sigma}_+\hat{a}^\dagger$ and $\hat{\sigma}_-\hat{a}$. We remain with the Jaynes-Cummings Hamiltonian for the interaction of a qubit with a microwave cavity mode [167],

$$\hat{H}_\mathrm{JC}/\hbar = \frac{1}{2}\omega_{01}\hat{\sigma}_z + \omega_\mathrm{r}\hat{a}^\dagger\hat{a} + g\left(\hat{a}^\dagger\hat{\sigma}_- + \hat{\sigma}_+\hat{a} \right). \tag{3.29}$$

3.5 Dispersive qubit state readout

The transverse coupling of qubit and readout cavity enables us to determine the qubit state by meseuring the cavity frequency. Having a large detuning between qubit and readout resonator frequency $\Delta = \omega_{01} - \omega_\mathrm{r}$ compared to the coupling strength, $g/\Delta \ll 1$, we are able to perform a dispersive readout of the qubit state [16, 17]. In the dispersive regime we find a shift of qubit and resonator frequency by a factor $\chi = g^2/\Delta$ for a perfect two level system, which allows for the qubit state to be measured along its quantization axis in a quantum nondemolition measurement [168]. Due to the low anharmonicity of the transmon, its dispersive shift consists of two contribution with opposite signs, $\chi = \chi_{01} - \chi_{12}/2 \simeq \frac{g^2 E_\mathrm{C}}{(\hbar\Delta - E_\mathrm{C})\Delta}$ for large $E_\mathrm{J}/E_\mathrm{C}$ [163]. Applying a unitary transformation

$$\hat{U} = \exp\left\{ \frac{g}{\Delta} \left(\hat{a}\hat{\sigma}_+ - \hat{a}^\dagger\hat{\sigma}_- \right) \right\} \tag{3.30}$$

diagonalizes Eq. (3.29). Expanding it up to the second order of χ we find [17]

$$\hat{U}\hat{H}_{\mathrm{JC}}\hat{U}^{\dagger}/\hbar \approx \frac{\omega'_{01}}{2}\hat{\sigma}_z + \left(\omega'_{\mathrm{r}} + \chi\hat{\sigma}_z\right)\hat{a}^{\dagger}\hat{a}, \tag{3.31}$$

with the renormalized frequencies $\omega'_{01} = \omega_{01} + \chi_{01}$ and $\omega'_{\mathrm{r}} = \omega_{\mathrm{r}} - \chi_{12}/2$ due to the cavity qubit interaction. The dressed frequency of the readout resonator depends on the state of the qubit, $\omega\left(\hat{\sigma}_z\right) = \omega_{\mathrm{r}} \pm \chi$. By probing the resonator, the qubit Bloch vector collapses into one of the eigenstates of the $\hat{\sigma}_z$ operator, $|0\rangle$ or $|1\rangle$. This interaction with the quantum mechanical system minimizes this impact on its time evolution and preserves the eigenstates of a qubit. Such a measurement scheme is referred to as a quantum nondemolition measurement.

We plot the transmon population on a scale from 0 to 1, with 0 corresponding to the the qubit being in the ground state $|0\rangle$ and accordingly for 1, and repeat the single projective measurements for statistic purpose.

4 Quantum Magnonics

In this chapter we describe the combination of the physical systems discussed in Ch. 2, coupling of magnons and photons, and Ch. 3, coupling of a transmon qubit, an artificial atom, to photons. With the qubit as a non-linear element in the system and using a photon mode in a microwave cavity as a bus system, we are able to create a nonlinear hybrid system containing magnetic excitations.

We explore the quantum hybrid system in two configurations. First the dispersive regime, where qubit and magnon are on resonance, far detuned from the cavity [65, 66]. Here, the effective qubit-magnon interaction is mediated by an effective coupling via the resonator coupling mode. Such a system with an effective qubit-harmonic oscillator coupling was studied in the past using photons regarding photon number states [169, 170], coherent superposition states [171] and Schrödinger cat states [172]. Recently, the first experiment regarding counting excitation number states was successfully carried out using magnons [67]. In the second configuration we describe a strongly coupled tripartite system, where all modes are degenerate and the strong coupling is directly observable in the reflection spectrum.

We discuss the overall coupling scheme in the dispersive regime regarding the expected effective coupling strength between qubit and magnon $\tilde{g}_{\mathrm{qm}}$ and describe the eigenfrequencies of the tripartite system by a set of three coupled harmonic oscillators and its reflection spectrum by expanding the input-output formalism to three participating components, where the transmon energy spectrum is truncated to only include the ground and excited qubit state. The chapter concludes with a short discussion of the influence of the applied magnetic field to the qubit frequency.

4.1 Dispersive regime

In the dispersive regime, the qubit frequency and the Kittel mode frequency are far detuned from the cavity resonator. Since there is negligible direct qubit-magnon coupling, the effective coupling is mediated by a virtual photon coupling using the cavity modes, with the nearest mode bearing the greatest share. The system is probed and read out similar to the bare qubit in the dispersive regime, monitoring

the state dependent resonance frequency of a higher cavity mode. On qubit-magnon resonance and given a strong effective coupling, the dispersive shift shows a magnon-vacuum-induced Rabi splitting [65]. For the system Hamiltonian we model the TE_{10p} mode resonance of the cavity and the Kittel mode resonance as harmonic oscillators and treat the qubit as an anharmonic oscillator with anharmonicity $\alpha \simeq -E_\mathrm{C} < 0$,

$$\hat{H}_\mathrm{sys}/\hbar = \sum_p \omega_{10p} \hat{a}_p^\dagger \hat{a}_p + \left[\left(\omega_\mathrm{q} - \frac{\alpha}{2} \right) \hat{q}^\dagger \hat{q} + \frac{\alpha}{2} \left(\hat{q}^\dagger \hat{q} \right)^2 \right] + \omega_\mathrm{m} \hat{m}^\dagger \hat{m}, \tag{4.1}$$

with the resonance frequency ω_{10p} of the $\mathrm{TE}_{10\mathrm{p}}$ cavity mode and the qubit and Kittel mode frequencies ω_q and ω_m, and the corresponding creation/annihilation operators $\hat{a}_p^\dagger/\hat{a}_p$, $\hat{q}^\dagger/\hat{q}$, and $\hat{m}^\dagger/\hat{m}$ for the cavity mode, the qubit, and the Kittel mode magnon, respectively. We neglect direct qubit-magnon coupling and write the interaction Hamiltonian for the remaining components,

$$\hat{H}_\mathrm{int}/\hbar = \sum_p g_{\mathrm{q},10p} \left(\hat{q}^\dagger \hat{a}_p + \hat{a}_p^\dagger \hat{q} \right) + \sum_p g_{\mathrm{m},10p} \left(\hat{m}^\dagger \hat{a}_p + \hat{a}_p^\dagger \hat{m} \right), \tag{4.2}$$

with $g_{\mathrm{q},10p}$ and $g_{\mathrm{m},10p}$ being the coupling strength of the $\mathrm{TE}_{10\mathrm{p}}$ mode with the qubit and the Kittel mode, respectively.

In the dispersive regime, the detuning of qubit and Kittel mode from the cavity modes much larger than any other energy regarding coupling strengths. Tuning the Kittel mode frequency towards the qubit transition, in the regime where $g_{\mathrm{q},10p},\ g_{\mathrm{q},10p} < |\omega_\mathrm{r} - \omega_\mathrm{m}|$, the interaction Hamiltonian is expressed in the rotating frame of the system Hamiltonian under perturbative approximation to the first order [173] as

$$\begin{aligned}
\hat{H}_\mathrm{int}/\hbar \approx & \sum_p \frac{g_{\mathrm{m},10p}^2}{\omega_{10p} - \omega_\mathrm{m}} \hat{a}_p^\dagger \hat{a}_p - \sum_p \frac{g_{\mathrm{m},10p}^2}{\omega_{10p} - \omega_\mathrm{m}} \hat{m}^\dagger \hat{m} \\
& - \sum_p \sum_{l>0} \lambda_{10p}^{(l)} |l\rangle_{\mathrm{q}\,\mathrm{q}} \langle l| + \sum_p \left(\chi_{10p} |0\rangle_{\mathrm{q}\,\mathrm{q}} \langle 0| + \sum_{l>0} \chi_{10p}^{(l)} |l\rangle_{\mathrm{q}\,\mathrm{q}} \langle l| \right) \hat{a}_p^\dagger \hat{a}_p \\
& - \sum_p \frac{1}{N} \frac{2 g_{\mathrm{m},10p}^2}{\omega_{10p} - \omega_\mathrm{m}} \hat{a}_p^\dagger \hat{a}_p \hat{m}^\dagger \hat{m},
\end{aligned} \tag{4.3}$$

where the first two terms describe dispersive shifts due to the cavity-magnon coupling, the third and fourth term describes the qubit frequency's Lamb shift and ac Stark shift, and the last term describes the static interaction between the cavity modes and the Kittel mode [66].

When the qubit and the Kittel mode frequency are degenerate, the detuning is smaller than the couling strengths and their coupling is mediated through virtual

photons in the far detuned cavity modes. The qubit-magnon detuning smaller than the coupling strength allows to transform the interaction Hamiltonian in the corresponding rotating frame using the Schrieffer-Wolff transformation [47], which eliminates the virtual photons. The effective qubit-magnon coupling on resonance is approximated by,

$$\hat{H}_{\mathrm{int}}/\hbar \approx \tilde{g}_{\mathrm{qm}} \left(\hat{m}^{\dagger} \hat{\sigma}_{-} + \hat{\sigma}_{+} \hat{m} \right), \tag{4.4}$$

with an effective coupling strength

$$\tilde{g}_{\mathrm{qm}} = \sum_{p} \frac{g_{\mathrm{m,10p}} g_{\mathrm{q,10p}}}{\omega_{10p} - \omega_{\mathrm{q}}}. \tag{4.5}$$

4.2 Tripartite system: light-matter-spin

In contrast to the dispersive regime, the detunings of the component frequencies in the tripartite system are smaller than the coupling strengths. The system is inspired by strong light-matter interaction experiments [16], where coherent interaction between qubit and microwave photon create an anticrossing in the reflection spectrum due to vacuum Rabi oscillations. Additionally, we tune the magnon frequency through the dressed qubit-photon states to further split up the reflection spectrum. The general coupling scheme is depicted in Fig. 4.1. Increasing the coupling from the uncoupled case (subfigure (a)) to the full qubit-resonator coupling (subfigure (b)) creates the dressed states. The magnon adds a third degree of freedom into the system, resulting in three modes with field dependent detunings Δ_1 and Δ_2 (subfigure (c)).

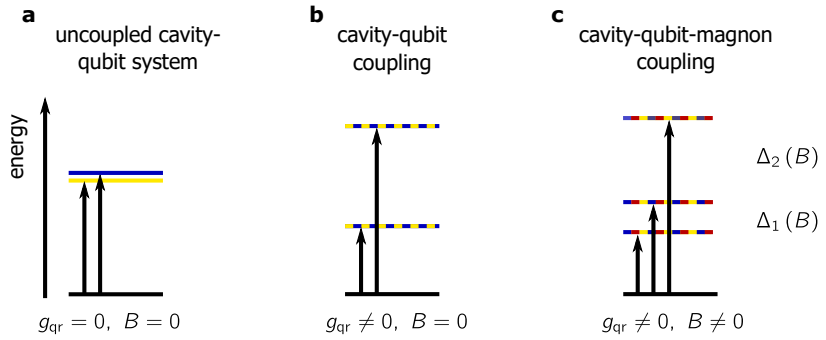

Figure 4.1: Schematic energy diagram of the strongly coupled tripartite system With nearly degenerate photon (yellow) and qubit (blue) frequencies the system forms dressed mixed states in the strong coupling regime that are not tunable (b). (c) The magnon (red) frequency is tuned with the applied magnetic field and the coupled system has three degrees of freedom that form three hybrid states with variable frequency spacing $\Delta_1(B)$ and $\Delta_2(B)$. (a) shows the zero coupling case in the presence of a strong probe drive.

We expand the general coupling scheme between two harmonic oscillators, Eq. (2.39), to three components, with the qubit treated as a harmonic oscillator in the weak-excitation approximation, and find the 3×3 coupling matrix

$$A = \begin{pmatrix} \omega_- \tilde{\omega}_\mathrm{r} & g_\mathrm{rm} & g_\mathrm{qm} \\ g_\mathrm{rm} & \omega_- \tilde{\omega} \omega_\mathrm{m} & g_\mathrm{qr} \\ g_\mathrm{qm} & g_\mathrm{qr} & \omega_- \tilde{\omega} \omega_\mathrm{q} \end{pmatrix}, \tag{4.6}$$

with the eigenvalues resulting in the dressed frequencies $\omega_{1/2/3}$. With the characteristic polynomial being a cubic function we obtain the eigenvalues by numerical calculation.

4.2.1 Reflection spectrum

We describe the reflection spectrum S_{11} of the tripartite system using the input-output formalism as described in Sec. 2.3.1. For this, the system Hamiltonian in the rotating wave approximation is expanded by the qubit contribution, that is approximated with the $\hat{\sigma}_z$ operator as a perfect two level system, and the respective coupling strengths,

$$\begin{aligned} \hat{H}_\mathrm{sys} = {} & \hbar \omega_\mathrm{r} \hat{a}^\dagger \hat{a} + \hbar \omega_\mathrm{m} \hat{m}^\dagger \hat{m} + \frac{\hbar \omega_\mathrm{q}}{2} \hat{\sigma}_z \\ & + \hbar g_\mathrm{qr} \left(\hat{a}^\dagger \hat{\sigma}_- + \hat{\sigma}_+ \hat{a} \right) + \hbar g_\mathrm{rm} \left(\hat{m}^\dagger \hat{a} + \hat{a}^\dagger \hat{m} \right) + \hbar g_\mathrm{qm} \left(\hat{m}^\dagger \hat{\sigma}_- + \hat{\sigma}_+ \hat{m} \right), \end{aligned} \tag{4.7}$$

with the frequency and creator/annihilator operators of the resonator, qubit, and magnon, ω_r and $\hat{a}^\dagger / \hat{a}$, ω_q and $\hat{\sigma}_+ / \hat{\sigma}_-$, and ω_m and $\hat{m}^\dagger / \hat{m}$, respectively. The indexes in the different coupling strengths indicate the participating components. The Hamiltonians describing the photon bath in the feed line and the system-to-bath coupling are the same as in Eqs. (2.42) and (2.43), respectively, which results in the same equation of motion for the resonator operator as in Eq. (2.52).

We use the weak-excitation approximation and assume the qubit to be in the ground state, $\langle \hat{\sigma}_z \rangle = -1$ [81, 174, 175], and find the set of three differential equations

$$\frac{\mathrm{d}\hat{a}}{\mathrm{d}t} = \left(-\mathrm{i}\omega_\mathrm{r} - \frac{\kappa_\mathrm{c}}{2} \right) \hat{a}\,(t) - \mathrm{i} g_\mathrm{rm} \hat{m}\,(t) - \mathrm{i} g_\mathrm{qp} \hat{\sigma}_-\,(t) + \sqrt{2\kappa_\mathrm{c}} \hat{b}_\mathrm{in}\,(t) \tag{4.8}$$

$$\frac{\mathrm{d}\hat{m}}{\mathrm{d}t} = -\mathrm{i}\omega_\mathrm{m} \hat{m}\,(t) - \mathrm{i} g_\mathrm{rm} \hat{a}\,(t) - \mathrm{i} g_\mathrm{qm} \hat{\sigma}_-\,(t) \tag{4.9}$$

$$\frac{\mathrm{d}\hat{\sigma}_-}{\mathrm{d}t} = -\mathrm{i}\omega_\mathrm{q} \hat{\sigma}_-\,(t) - \mathrm{i} g_\mathrm{qr} \hat{a}\,(t) - \mathrm{i} g_\mathrm{qm} \hat{m}\,(t)\,. \tag{4.10}$$

The system is then Fourier-transformed and solved for the individual annihilation operators. We insert the resonator annihilator into the relation of the reflection

spectrum to the incoming and outgoing field operators $\hat{b}_{\mathrm{in}}/\hat{b}_{\mathrm{out}}$, Eq. (2.44), and include the complex renormalization of the resonance frequencies $\omega_j \to \omega_j - \mathrm{i}\kappa_j$ to account for internal losses in component j,

$$S_{11} = -1 + \frac{2\kappa_{\mathrm{c}}}{R + \frac{g_{\mathrm{qr}}^2}{Q+\frac{g_{\mathrm{qm}}^2}{M}} + \frac{g_{\mathrm{rm}}^2}{M+\frac{g_{\mathrm{qm}}^2}{Q}} - \frac{2\mathrm{i}g_{\mathrm{qr}}g_{\mathrm{rm}}g_{\mathrm{qm}}}{MQ+g_{\mathrm{qm}}^2}}, \text{ with} \tag{4.11}$$

$$R = \mathrm{i}\left(\omega_{\mathrm{r}} - \omega\right) + \kappa_{\mathrm{l}}, \tag{4.12}$$

$$Q = \mathrm{i}\left(\omega_{\mathrm{q}} - \omega\right) + \kappa_{\mathrm{q}}, \text{ and} \tag{4.13}$$

$$M = \mathrm{i}\left(\omega_{\mathrm{m}} - \omega\right) + \kappa_{\mathrm{m}}. \tag{4.14}$$

Comparing this to the spectrum containing two components, Eq. (2.59), we identify the second term in the denominator as resonator-qubit coupling with a subsequent coupling to the magnon. Similarly, the third term describes the resonator-magnon coupling with subsequent coupling to the qubit. The last term in the denominator is attributed to a correction of the qubit-magnon coupling that is counted in twice.

The approximation to truncate the qubit to its two lowest level breaks down when other qubit levels are excited by multi-photon transitions or due to thermal excitation. In this case, the Hamiltonian in Eq. (4.7) with one qubit frequency is not valid anymore and the full transmon Hamiltonian, described in Sec. 3.3, with its anharmonic level structure and coupling strengths of the individual transitions to the other system components is used and we simulate the spectrum numerically.

4.3 Superconducting qubit in magnetic field

By tuning the frequency of the magnon excitation we expose the superconducting transmon qubit to an in-plane magnetic field. We work with a 3D transmon qubit design, see Sec. 5.2, with one single Josephson junction whose critical current I_{c} is periodically suppressed by the magnetic field which results in the shape of a Fraunhofer diffraction pattern [176],

$$I_{\mathrm{c}}\left(B\right) = I_{\mathrm{c}}^{0}\left|\mathrm{sinc}\left(\frac{B}{B_{\Phi_0}}\right)\right|, \tag{4.15}$$

with B_{Φ_0} being the magnetic field corresponding to one flux quantum in the effective junction cross section area. Approximating the sinc function, $\mathrm{sinc}\left(x\right) =\approx 1 - \frac{x^2}{6} + \mathcal{O}(x^4)$, and with $E_{\mathrm{J}} \propto I_{\mathrm{c}}$, we assume a linear dependence with negative slope of the fundamental qubit transition frequency on the applied magnetic field. The single qubit fabrication step eliminates unwanted additional Josephson junctions,

whose large overlapp surface results in a higher sensitivity to applied magnetic fields and the I_c dependence is described as a complex trigonometric relation of the two junctions [177]. The coherence of the transmon qubit decreases with increasing magnetic field, with the T_1 time being reduced by dissipation due to entering flux vortices in the aluminium thin film and their movement due to the rf current [178] and dissipation through quasiparticle losses [179–181].

5 Experimental methods

This chapter presents details about the sample fabrication process and the used experimental setup during this work. Our samples consists of three components, a commercially obtained magnetic sample, a machine-milled copper cavity resonator, and a nanostructured superconducting qubit. We briefly discuss the details of the magnetic sample, provide the basic fabrication concept for superconducting qubits using a Josephson tunnel junction, and discuss the cavity resonator. In order to access the quantum regime with our samples we perform the experiments at millikelvin temperatures. This strongly suppresses classical thermal noise and higher energy levels do not get populated thermally. We describe the cryogenic measurement setup and briefly discuss the working scheme of a ^{3}He/^{4}He dilution refrigerator. The samples are probed by microwave excitations with respect to different magnetic bias fields, which requires certain hardware and wiring components. After that, we focus on the employed measurement technique using spectroscopic and time-resolved measurement schemes as well as the used measurement software package.

5.1 Magnetic sample

Throughout this thesis we use two different commercially available magnetic YIG samples that we obtained from Ferrisphere, Inc.[1]. The single crystal YIG samples come diamond polished to a spherical shape with diameters of 0.5 mm and 1.0 mm, giving them an estimated 50 nm surface roughness. The spheres are already pre-mounted to a ceramic beryllium oxide rod oriented along the [110] crystal direction.

5.2 Qubit sample

The qubit samples fabricated during this thesis are in-house fabricated in the cleanroom facilities of the Nanostructure Service Laboratory of the Center of

[1] Ferrisphere, Inc., `https://www.ferrisphere.com` - accessed Oct. 18, 2019

Functional Nanostructures at the KIT. A detailed step-by-step list of the different cleanroom fabrication steps can be found in Appendix A.

All samples are fabricated on intrinsic silicon wafers with a thickness of 380 µm and a dielectric constant of $\epsilon_r = 11.5$. Prior to any fabrication the substrate is cleaned with N-Ethyl-2-pyrrolidone (NEP) to remove organic residues. The Josephson tunnel junction and the remaining qubit structures are fabricated using electron beam lithography and shadow angle evaporation.

The basic principle of the Dolan bridge technique [182] is to create a free-hanging bridge of resist and to evaporate metal from two different directions onto the substrate. This creates two electrodes with an overlap area forming the Josephson junction. We spin coat a $20 \times 20\,\mathrm{mm}^2$ wafer chip with a dual resist stack of LOR/PMMA. The resists have different critical doses regarding the electron exposure. At a certain dose, only one of the exposed resist is removed by the developer afterwards, which results in washing out the LOR under a free hanging PMMA bridge.

The deposition of both metal layers is done thermally by evaporating an aluminium (Al) target in a PLASSYS Bestec MBE550S machine. Leftover resist residue is cleaned by a cleaning plasma with a 8 : 1 argon/oxygen mixture plasma before evaporating the metal. The the first Al layer is evaporated with a positive tilt angle before an insulating tunnel barrier is formed by dynamic in-situ oxidation. A controlled amount of oxygen is led into the chamber and the background pressure is adjusted via continuous oxygen input and pumping output. The 30 min exposure to the oxygen creates a ~ 1 nm thin insulating AlOx layer. The second Al layer is evaporated under a negative tilt angle and forms the Josephson junction, the connection between both electrodes. The two evaporation steps form the rest of the qubit as well.

We evaporate 30 nm and 50 nm Al, resulting in an overall thickness of 80 nm throughout the chip. The remaining resist is removed in a lift-off process, leaving only the written metallic structure on the chip. The chips are diced into $14 \times 2\,\mathrm{mm}^2$ strips, each containing a single qubit.

5.3 Cavity resonator

The cavity resonators are machine milled by our in-house mechanical workshop out of oxygen-free copper. For the experiments we use two similar cavities only differing in one dimension of the resonance volume. The nominal resonance volumes are $83 \times 40 \times 3\,\mathrm{mm}^3$ and $83 \times 37 \times 3\,\mathrm{mm}^3$, respectively, with rounded 1.5 mm corner radii in the xz-plane due to fabrication restraints. The boxes feature a cut in

parallel to the xz-plane to access the cavity cutout and insert the other components of the sample.

A hole with a diameter of 1 mm is drilled into one end of the box at half height to hold the magnetic sample in place. This is a point of maximum magnetic field of the resonance photon and the point where the external bias field is applied. The lower part of the opened box features a cutout to hold the qubit chip which is oriented in parallel to the electric field component of the resonance field. In order to lower the impact of the applied magnetic field to the performance of the superconducting qubit by worsen its coherence properties, the qubit chip and the magnetic sample are mounted on opposite ends of the resonator cutout.

The cavity resonance gets excited by an 50 Ω matched straight terminal SMA connector, with the inner conductor extending into the cavity volume in parallel to the electric field. The bottom part of the boxes feature several M3 threads to hold it in place in the cryostat and establish a thermal connection. The assembled sample is depicted in Fig. 5.1(c).

5.4 Cryogenic setup

All experiments are carried out in an Oxford Instruments Triton 200 dry dilution refrigerator, depicted in Fig. 5.1(a).

The cryostat setup consists of five gold-coated copper plates at different temperatures. The two highest plates, the PT1 and PT2 stage at about 50 K and 3 K, respectively, are cooled mechanically via a pulse tube cryocooler. Pressurized helium is used as a heat exchange gas and pumped from a room temperature compressor to the heat exchangers at these two plates. Releasing the pressure of the helium, the gas picks up heat at the heat exchangers and cools the connected PT1 and PT2 plate. The heat of the compressed gas is drawn off at room temperature. The three lower plates, still plate, intermediate plate, and the base plate containing the mixing chamber, are cooled via a secondary pre-cooler circulating the ^{3}He/^{4}He mixture. The mixture is cooled at both pulse tube stages and picks up heat at the other plates on its way back to room temperature. We pump the volume inside the cryostat to vacuum to avoid any thermal contact between the different plates via air molecules.

Cooling the fridge further down towards millikelvin temperatures, we employ a standard technique by using the phase separation of the He mixture. The warm mixture (75 L overall volume with nearly 15 % of ^{3}He) is injected into the circulation lines with a pressure of about 2.5 bar. The mixture condenses in the still volume

making use of the Joule-Thomson effect, cooling the still, intermediate, and base plate down to about 1.2 K. The circulation process starts when all mixture is liquefied.

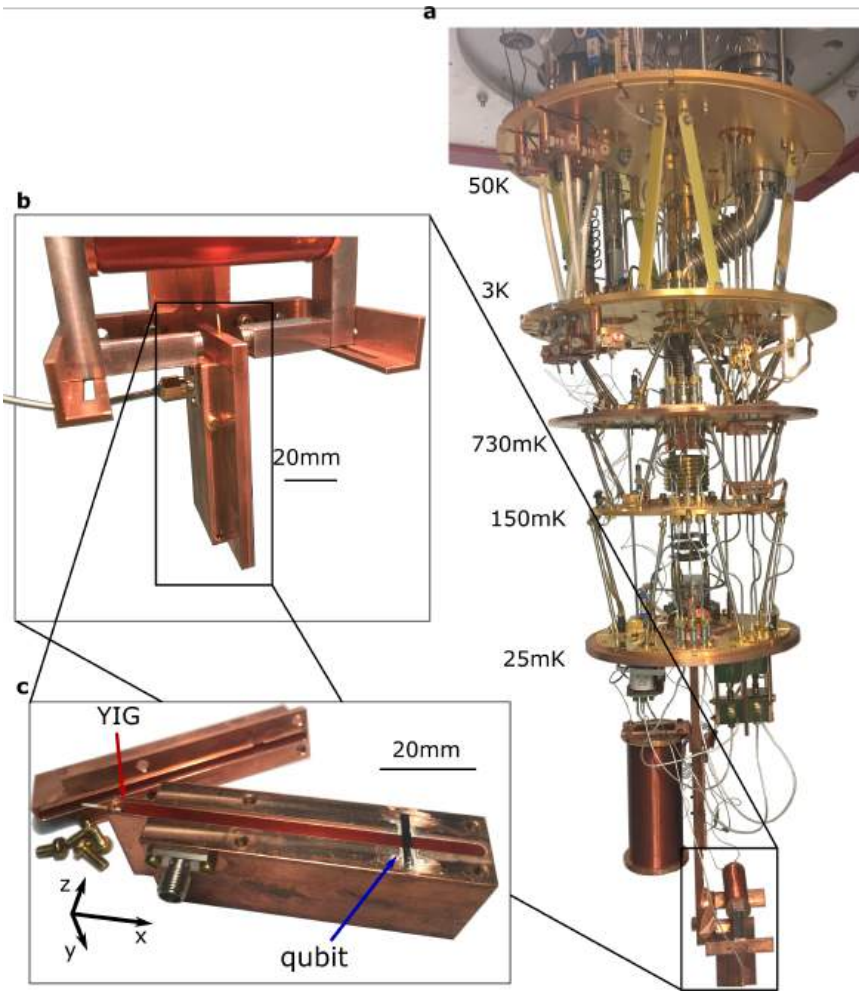

Figure 5.1: Opened dilution refrigerator and sample box (a) Picture of the opened dilution refrigerator with the sample located at the very bottom. The temperatures of the stages decreases from top to bottom. (b) We apply an external magnetic field at the position of the YIG. A pure iron yoke with a superconducting coil and additional SmCo permanent magnets provide the magnetic field strength to tune the Kittel mode resonance frequency to the gigahertz regime. (c) The used copper box features a milled cavity, the YIG sphere mounted to a BeO rod positioned in an anti-node of the magnetic field, and the superconducting transmon qubit positioned in parallel near the maximum anti-node of the electric field of the cavity. The distance between YIG and qubit decreases the magnetic field influence on the superconducting Al.

Below a critical temperature of about 870 mK, the helium mixture undergoes a spontaneous phase transition in a ^{3}He-rich and a ^{4}He-rich phase [183], which is forced out of equilibrium and the system extract energy from the environment to regain equilibrium. The ^{3}He-rich phase floats on top and consists of almost pure ^{3}He, with the ^{4}He-rich phase containing about 6.6 % of ^{3}He. The circulated ^{3}He is pumped into the ^{4}He-rich phase and disturbs the equilibrium concentration. The system relaxes back into equilibrium by bringing ^{3}He into the ^{3}He-rich phase, a process that effectively absorbs thermal energy from the base plate. The almost pure ^{3}He is pumped out of the still volume, cleaned at room temperature using a liquid nitrogen cold trap, and injected back into the mixing chamber from above. The warm gas is cooled on its way down by exchange cooler, using colder ^{3}He coming from the mixing chamber to the still. A dilution refrigerator reaches single digit mK temperatures employing this cooling process. Without additional sample wiring we are able to measure a base temperature of 9.8 mK in our cryostat using a ^{60}Co-based nuclear orientation primary thermometer, thereby calibrating our ruthenium oxide resistance thermometer for further cool-downs. Fully equipped our cryostat reaches working temperatures of about 25 mK.

The cooper box with the cavity resonator and all other components of our sample are thermally and mechanically anchored with additional copper connections to the base plate of the cryostat.

5.4.1 Magnetic field bias

We require a homogeneous static magnetic field at the position of the magnetic sample in order to tune the frequency of our magnetic resonance. Tuning these resonances in the GHz regime requires fields on the order of several hundred millitesla at the mixing chamber stage of the cryostat at millikelvin temperatures.

We utilize a pure-iron magnetic yoke construction to provide the field bias to our sample. The field itself is created by a homemade superconducting coil made out of a wire containing 54 niobium-titanium (NbTi) alloy filaments in a copper matrix with a total of about 4500 winding turns. Additional cylindrical samarium-cobalt permanent magnets, each yoke side equipped with one $\varnothing$10 mm $\times$ 5 mm and three $\varnothing$10 mm $\times$ 1 mm disks, create an offset field of about 178 mT, see Fig. 5.1(b). The magnetic field is concentrated around the magnetic sample inside the cavity resonator. We can tune the magnetic field with a rate of about 4.35 mT/A, the actual current-field conversion factor changes between different cool-downs due to hysteresis effects in the permanent magnet and are also temperature dependent during a single cool-down.

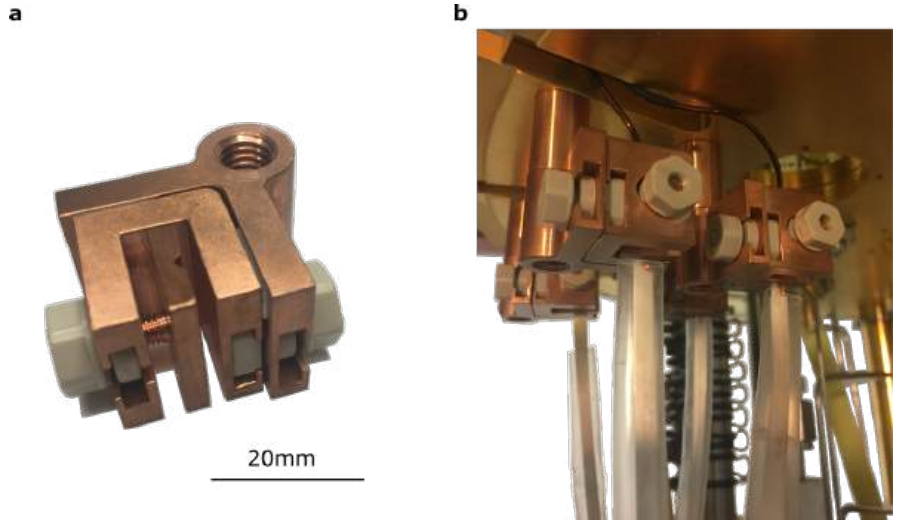

Figure 5.2: Clamping connection We use a clamping mechanism to create a low resistance, non-soldered connection between two superconducting wires. The inner copper clamps are electrically isolated from the outer holder by insulating sapphire wafers that are thermally conductive at low temperatures and pass the heat dissipated by the contact resistance to the cryostat plates. Insulating polyether ether ketone (PEEK) screws connect both parts. This mechanism is used at both pulse tube cooled stages where the cooling power is large enough to cope with the additional thermal input. (a) Closeup of the clamping mechanism. (b) Installation below the PT1 stage, connecting normal conducting copper wires to superconducting YBCO strips.

With these tuning rates we require current values in the range of single digit amperes to perform our experiments. We use normal conducting ∅1.5 mm copper wires from room temperature to the PT1 stage that are connected to a stainles steel strip coated with yttrium barium copper oxide (YBCO), a high-T_c superconductor provided to us by the group of Prof. Bernhard Holzapfel of the Institute for Technical Physics (ITP) at KIT. Since we cannot solder YBCO to the copper we utilize a clamping mechanism to press both wires together, leaving only a small contact resistance. The dissipated heat has to be transferred to the thermal anchoring point at the plate while at the same time maintaining galvanic isolation between current leads and cryostat ground. We use two interleaved clamps made out of copper with a small gap in between that is filled with several sapphire wafer pieces and insulating polyether ether ketone (PEEK) screws that connect both parts. Sapphire is an insulating material regarding charge transport but a well conducting material at low temperatures regarding thermal excitation. The clamps were designed and fabricated by our mechanical workshop and are depicted in Fig. 5.2. The same technique is employed at the PT2 stage, connecting the YBCO wire to the low-T_c superconductor NbTi wire with $T_c \sim 10\,\mathrm{K}$ that is used for the magnetic coil.

Any further thermal anchoring at the still plate and intermediate plate is done by winding the wire around a copper post and gluing it with epoxy, with the insulation coating of the wire preventing an electrical short to ground. Between the lower plates, thermal conduction of phonons within the copper matrix is prevented by wet etching of the copper between the still and intermediate stage, as well as the intermediate stage and the mixing chamber. We etch the copper with with a 30 % nitric acid (HNO_3) solution over a distance of several centimeters and glue the bare NbTi filaments with GE low temperature varnish to account for the reduced mechanical stability. This setup is tested up to currents of 10 A with the temperatures of the cryostat at the normal operating levels.

5.4.2 Microwave setup

In order to minimize the thermal load to the stages, we use coaxial cables of different material between the different temperature stages for the microwave wiring. We further minimize additional thermal noise input by attenuators and maximize our signal strength on the output side by amplifies and filtering.

On the input side we use stainless steel cables all the way down to the base plate with thermal anchoring at all plates. All microwave components influencing the microwave signal such as attenuators, circulators, and amplifiers must therefore operate in this frequency range as well as the temperature of their local environment. Microwave attenuators are inserted at different temperature stages to reduce the microwave signal power and to avoid thermal excitation at higher temperatures plates. We insert 20 dB attenuators and thermally anchor them at the PT2 stage, still stage, and base plate at typical temperatures of $T_{\mathrm{PT2}} = 3\,\mathrm{K}$, $T_{\mathrm{still}} = 730\,\mathrm{mK}$, and $T_{\mathrm{base}} = 25\,\mathrm{mK}$ to reduce the Johnson-Nyquist noise power by a factor of 100 at each stage. We attribute additional 15 dB attenuation to the microwave cables and connections at our measurement frequencies prior to the sample input.

The reflected measurement signal from the sample is separated from the input signal by two cryogenic circulators connected in series. We therefore avoid the signal carrying the measurement data to be attenuated by the incoming lines and are able to further amplify the signal. On the outgoing side, we avoid cable losses by using superconducting niobium coaxial cables from the mixing plate to the PT2 stage. Additionally, the circulators shield the sample from unwanted incoming electric noise created by the amplifiers. We use two Quinstar QCY circulators operating between 4 GHz and 8 GHz that are shielded against 100 mT of magnetic field. At the PT2 stage we band-pass filter the signal by a MiniCircuit VHF-3100+ limiting the measurement to a band between 3.4 GHz and 9.9 GHz, before it is amplified by a Low Noise Factory LNF-LNC4_8C s/n 301C high electron mobility transistor (HEMT)

amplifier. The HEMT has a dedicated amplification band between 4 GHz and 8 GHz with an amplification of 40 dB and an added noise equivalent temperature of 2.0 K.

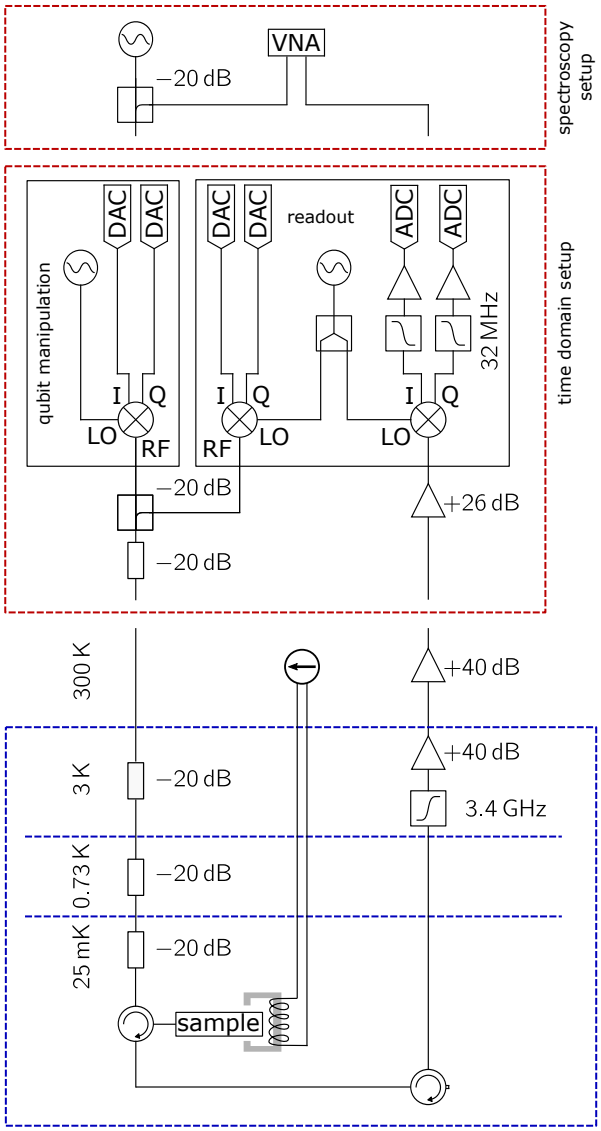

Figure 5.3: Schematic setup for spectroscopic and time resolved measurements Depending on the type of experiment we either use the spectroscopy setup or the time domain setup (red) to measure the sample in the cryostat (blue). The components in between sit at room temperature and are used as part of both measurement schemes.

We use copper-nickel wires for the connection from the PT2 stage to room temperature. A second amplifier at room temperature is used to amplify the signal again before being recorded. We use a broadband Narda-MITEQ AMF-5D-00101200-23-10P amplifier with a gain of 40 dB in an operating frequency range between 1 GHz and 12 GHz.

5.5 Spectroscopic measurements

In spectroscopic measurements we probe the sample with continuous microwave signals from a Keysight E5071C vector network analyzer (VNA) that measures the complex scattering matrix element S_{21}. While we measure the reflection characteristics of our sample, the wiring through the cryostat is built to appear as a transmission signal for the VNA. By analyzing the amplitude and phase response we extract resonator parameters or measure the hybrid systems by varying the excitation power or the applied magnetic field. An additional microwave tone, for example to measure the AC stark shift of the qubit, is provided by an Anritsu MG37020A microwave source and is fed into the input line by a directional coupler. The spectroscopic measurement setup is schematically depicted in Fig. 5.3.

5.6 Time resolved measurements

The time-dependent properties of the qubit are measured by manipulating its state with pre-defined microwave pulses and record the response of the system after a free evolution time Δt. The pulses rotate the Bloch vector around different axis of the Bloch sphere, while the final measurement always is an averaged qubit state measurement.

We use a field programmable gate array (FPGA)-based setup developed by the group of Prof. Marc Weber of the Institute for Data Processing and Electronics (IPE) at KIT [184]. The FPGA board handles the pulse sequence and trigger as well as the data recording, while an analog microwave front-end is used to ensure synchronized pulses, amplification, and attenuation as well as frequency conversion to and from gigahertz frequencies. A schematic sketch of the setup is depicted in Fig. 5.3.

The FPGA hardware platform runs a Linux operating system that eliminates the need for an external control computer during the experiment. With the whole experiment, data collection, and data processing being handled by the FPGA we are able to shorten the overall experimental time compared to traditional setup using an arbitrary waveform generator. A sequencer controls the pulse generation and

triggering for manipulation, readout, and data recording. It operates at 125 MHz clock frequency, leading to a time resolution of 8 ns. For convenience, the pulse sequences of frequently used qubit characterization experiments are pre-programmed, with only the time delays as input parameter. The sequencer triggers the pulse generator that feeds the amplitude modulated pulse to a digital-to-analog-converter (DAC) as the intermediate frequency (IF) for further analog signal processing. The MHz IF signal is mixed by an I/Q mixer with a local oscillator (LO) GHz signal, resulting in the sum and the difference of both frequencies. This converts the signal to the qubit or readout resonator into the GHz regime. The response from the system with respect to the readout pulse is down-converted using the same power divided LO signal as the up-converted readout pulse. The signal is low-pass filtered, 28 dB amplified, digitized by the analog-to-digital-converted (ADC), and recorded by the FPGA module.

We use a Xilinx Zync UltraScale+ MPSoC ZCU 102 evaluation board with a Zync UltraScale+ XCZU9EG-2FFVB1156I multiprocessor system-on-chip together with two Texas Instrument evaluation cards as ADC (ADS54J69EVM) and DAC (DAC39J84EVM). Two Anritsu MG37022A microwave sources are used as local oscillators for manipulation and readout. We use a Marki IQ-0318L mixer for the manipulation signal and a Marki MLIQ-0416L mixer for the readout and recording signal. Manipulation and readout input into the fridge are combined by a Marki C20-0R520 directional coupler where the readout is −20 dB attenuated and the down-converted recording signals are amplified by Mini-Circuits ZFL-1000H amplifiers. The LO signal for readout and recording is split by a Mini-Circuits ZFRSC-123S+ power divider.

5.7 Calibration routine before fitting the reflection spectrum

The measurement setup, with its cable damping, cable connections, and all other added microwave components, contributes to the overall measured signal of the VNA due to frequency dependent attenuation and combined standing waves because of impedance mismatches and reflections in the coaxial cables. In order to separate the signal from the setup and from the sample we estimate the magnetic field independent baseline signal and consider it during the fitting process of the reflection spectrum of the coupled system. The procedure is detailed for the magnon-photon hybrid system, but is also used for the tripartite system considering the three hybridized modes. At the same time we reduce the number of free fit parameters, where we

obtain numerical values from different fit procedures and fix these values in the fit of the adapted spectrum.

5.7.1 Baseline estimation

Hybridizing magnon and photon results in two resonance dips in the in the reflection spectrum. While the measured signal outside of the dips stems from the measurement setup, the dip signal is a combination of setup and system. We estimate the setup baseline by via the field dependent hybridized modes, with which we identify the probe frequencies which contain only background information for each magnetic field value. We track the resonance minima of both cavity magnon polariton branches and cut a frequency band with a width of three times the loaded resonator linewidth below and above the tracked dressed frequencies from the original data. These system responses are influenced by the underlying physical system. Due to the strong coupling in our system, the two polariton branches separate in the anticrossing enough from each other to allow access to the measurement background of the setup even at the original resonator frequency. We determine the background by mediating the respective data for each probe frequency ω_P over all occurring current values and create an estimated response signal of the measurement setup.

5.7.2 Adapting the fit routine

The frequency dependent background $|S_{11}|_\mathrm{back}(\omega_\mathrm{P})$ is included into the fitting process of the reflection spectrum to only fit the signal of the underlying physical system. This is realized either by normalizing the original data and fitting it to Eq. (2.59) or by modifying the fit function and fit it to the original data. We adapt the fit function for the amplitude of the reflection spectrum to

$$\begin{aligned} |S_{11}|_\mathrm{fit}(\omega_\mathrm{P}) &= |S_{11}|(\omega_\mathrm{P}) \cdot |S_{11}|_\mathrm{back}(\omega_\mathrm{P}) \\ &= \left| -1 + \frac{\kappa_\mathrm{c}}{\mathrm{i}(\omega_\mathrm{r} - \omega_\mathrm{P}) + \frac{\kappa_\mathrm{l}}{2} + \frac{g^2}{\mathrm{i}(\omega_\mathrm{m} - \omega_\mathrm{P}) + \frac{\kappa_\mathrm{m}}{2}}} \right| \cdot |S_{11}|_\mathrm{back}(\omega_\mathrm{P}) \,. \end{aligned} \tag{5.1}$$

Since $|S_{11}|_\mathrm{back}(\omega_\mathrm{P})$ is a single, known number for each ω_P we do not increase the number of fit parameters.

We further reduce the number of fit parameters from six to only one, the internal magnetic linewidth κ_m, by determining system parameters from different measurements or data analysis. The bare cavity resonator frequency ω_r, the field dependent magnon frequency $\omega_\mathrm{m}(I)$ and the coupling strength g are determined by fitting the

tracked minima of the two branches to the eigenvalues $\omega_\pm$ of the 2×2 coupling matrix in the set of equations describing the two coupled harmonics oscillators, Eq. (2.40). The two resonator linewidths κ_l and κ_c are obtained by the zero-current measurements of the cavity resonator, table 6.1, which are independent of the applied magnetic field.

5.8 Measurement software: qkit

We perform our experiments with qkit, an open-source Python software suite developed at KIT [185]. The main focus lies on standardized measurement routines such as sweeps of multiple parameters in spectroscopic measurements and an integration of time-resolved qubit measurements. Instrument drivers handle the device communication and make the measurement code independent of the specific devices. This makes measurements flexible and adaptable for new users and new measurement ideas.

The software has its roots, in particular the basic device communication, in the QTLab software package[2], written by R. Heeres. We adapt his approach to our needs and the software is publicly available in a repository on the GitHub development platform. Our main focus is to build a common platform for all measurements in our lab with a powerful dynamical data viewer based on the PyQtGraph package[3] and an efficient data storage using the HDF format[4]. Qkit now provides a measurement environment for microwave and transport measurements, typically controlled via Jupyter Notebook[5]. It features data acquisition, storage, and visualization as well as some basic analysis tools for microwave resonators.

[2] QTLab, `http://www.pyqtgraph.org` - accessed Oct. 18, 2019
[3] PyQtGraph, `https://www.pyqtgraph.org` - accessed Oct. 18, 2019
[4] HDF Group, `https://www.hdfgroup.org` - accessed Oct. 18, 2019
[5] Project Jupyter, `https://jupyter.org` - accessed Oct. 18, 2019

6 Cavity resonator characterization

In this chapter we present the microwave spectroscopy characterization of the two cavities used throughout this thesis. This resonance characteristics are relevant not only for fitting parameters, but also define the number of photon excitation of the system. For both cavities we focus especially on the resonance spectrum of the TE_{102} mode, since the photons exciting these resonances are used as a component in our hybrid systems. The additional TE_{101} and TE_{103} modes are only used for second tone excitation or readout purposes, where only the resonance frequency is relevant. We take a closer look to the *mk_3* cavity resonances, used in experiments without qubit, with respect to the excitation power. This allows us to attribute any power dependent changes to the corresponding component of the hybrid system.

6.1 *mk_3* cavity charaterization

We characterize the TE_{102} resonance of the *mk_3* cavity at $T = 55\,\mathrm{mK}$ for various probe powers corresponding to the experiments in Sec. 7.2 by using a circle fit routine. The cavity cutout responsible for the resonance has a spacial volume of $83 \times 40 \times 3\mathrm{mm}^3$.

Table 6.1: Resonance parameters cavity *mk_3* TE_{102} resonance mode. The table includes the zero-current resonator frequency $\omega_\mathrm{r}^{I=0}$ and the loaded, coupling, and internal quality factors Q_l, Q_c, and Q_i.

$\omega_\mathrm{r}^{I=0}/2\pi$ (GHz)	Q_l	Q_c	Q_i
$5.239474 \pm (2 \cdot 10^{-6})$	3084.4 ± 5.1	5438.9 ± 4.1	7124.9 ± 34.3

Since the magnetic part of the measurement setup features permanent magnets, we already apply a magnetic field to the YIG sample at any time that slightly dresses the bare resonator frequency ω_r. At zero applied current we measure a dressed resonance frequency $\omega_\mathrm{r}^{I=0}$. With a probe power $P = -140\,\mathrm{dBm}$, the fit determines a zero-current resonance frequency $\omega_\mathrm{r}^{I=0} = 5.239\,474\,\mathrm{GHz} \pm 2\,\mathrm{kHz}$ and quality factors

$Q_l = 3084.4 \pm 5.1\,\mathrm{MHz}$, $Q_c = 5438.9 \pm 4.1\,\mathrm{MHz}$, and $Q_i = 7124.9 \pm 34.3\,\mathrm{MHz}$, see Figs. 6.2(a), (c), and (e). We compare the measured resonance frequency with finite integration simulation using CST Studio Suite [1], which results in a simulated $\omega_r^{sim} = 5.212\,\mathrm{GHz}$ that matches well the measurement. Besides an initial change of the quality factors we observe the TE_{102} resonance parameters to be constant with the applied power, see Fig 6.1.

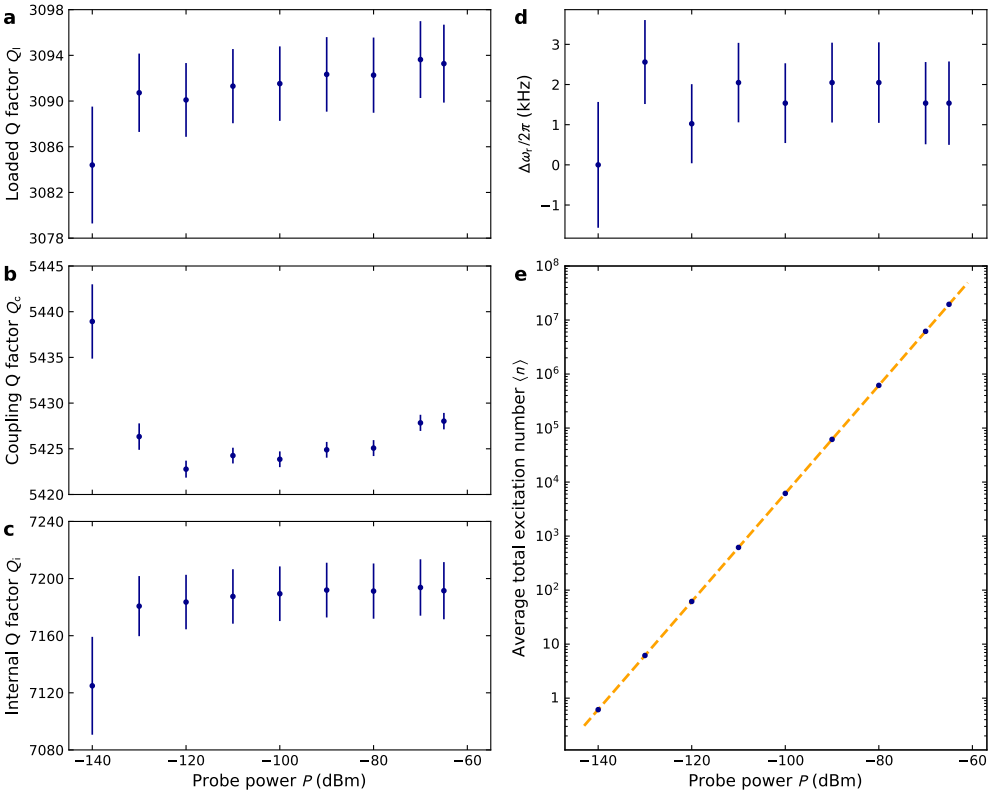

Figure 6.1: Resonator parameters of the TE_{102} resonance of the *mk_3* cavity (a-c) Loaded, coupling, and internal quality factors of the cavity resonance against probe power. The data was taken at $T = 55\,\mathrm{mK}$ with zero current applied to the magnetic coil and does not show a power dependent behavior. (d) Shift of the fitted cavity frequencies $\Delta\omega = [\omega_r(P) - \omega_r(P = -140\,\mathrm{dBm})]$ with compared to the measurement at lowest probe power at zero current. Similar as with the quality factors, the cavity frequency does not show a power dependence. (e) Calculated average photon number in cavity against probe power. The fit shows a linear dependence of the photon number calculated with Eq. (2.15) to the input power. Note that this plot features a log-log scale, making the fit linear again. The errors on the average photon number are estimated to be smaller than 0.35 % and are not visible in this plot.

[1] Dassault Systèmes Simulia, `https://www.3ds.com` - accessed Oct. 18, 2019

We estimate the average excitation $\langle n \rangle$ in the cavity corresponding to the applied power with Eq. (2.15) and obtain

$$\langle n \rangle = 62.046 \cdot P_{\text{in}}^{1.0003}\,\text{fW}^{-1}. \tag{6.1}$$

The single photon parameters of the TE_{102} resonance of the *mk_3* cavity at $T = 25\,\text{mK}$ are also listed in table 6.1. In addition, we obtain the TE_{101} and TE_{103} resonance frequencies at $\omega_{\text{r},101}^{I=0} = 4.174\,811\,\text{GHz} \pm 5\,\text{kHz}$ and $\omega_{\text{r},103}^{I=0} = 6.644\,516\,\text{GHz} \pm 8\,\text{kHz}$, respectively. From simulation we obtain the resonance frequencies $\omega_{\text{r},101}^{\text{sim}} = 4.162\,\text{GHz}$ and $\omega_{\text{r},103}^{\text{sim}} = 6.606\,\text{GHz}$. All simulations match the measurements with an error of less than 0.6 %, with the simulated values all being larger than the measurements.

6.2 *mk_4* cavity charaterization

The *mk_4* cavity is used for the experiments on the strongly coupled magnon-photon-qubit system. Since the resonance frequency of the TE_{102} almost matches the first qubit transition frequency, both systems hybridize and form dressed state at low powers.

Table 6.2: Resonance parameters cavity *mk_4* TE_{102} resonance mode. The table includes the zero-current resonator frequency $\omega_{\text{r}}^{I=0}$ and the loaded, coupling, and internal quality factors Q_{l}, Q_{c}, and Q_{i}.

$\omega_{\text{r}}^{I=0}/2\pi$ (GHz)	Q_{l}	Q_{c}	Q_{i}
$5.453271 \pm (8 \cdot 10^{-6})$	1639.4 ± 3.0	2076.4 ± 2.2	7790.2 ± 56.4

The difference in resonance frequency compared to the *mk_3* cavity is realized by changing the resonance volume to $83 \times 37 \times 3\text{m}^3$. We access the pure cavity resonance parameters by applying a large probe power that decouples both components. The fit determines a zero-current resonance frequency $\omega_{\text{r}}^{I=0} = 5.453\,271\,\text{GHz} \pm 8\,\text{kHz}$ and quality factors $Q_{\text{l}} = 1639.4 \pm 3.0\,\text{MHz}$, $Q_{\text{c}} = 2076.4 \pm 2.2\,\text{MHz}$, and $Q_{\text{i}} = 7790.2 \pm 56.4\,\text{MHz}$ with $P = -80\,\text{dBm}$, Figs. 6.2(b), (d), and (f). We determine the TE_{101} and TE_{103} resonance frequencies at $\omega_{\text{r},101}^{I=0} = 4.468\,080\,1\,\text{GHz} \pm 0.8\,\text{kHz}$ and $\omega_{\text{r},103}^{I=0} = 6.799\,464\,4\,\text{GHz} \pm 0.4\,\text{kHz}$, respectively. From simulation we obtain the resonance frequencies $\omega_{\text{r},101}^{\text{sim}} = 4.337\,\text{GHz}$, $\omega_{\text{r},102}^{\text{sim}} = 5.345\,\text{GHz}$, and $\omega_{\text{r},103}^{\text{sim}} = 6.690\,\text{GHz}$. All simulations match the measurements with an error of less than 3 %, with the simulated values here all being smaller than the measurements. Looking at the resonance parameters of the *mk_3* cavity, we assume constant resonance

parameters in this cavity with respect to power as well. The resonance parameters of the the TE_{102} resonance of the *mk_4* cavity at a probe power $P = -80\,\mathrm{dBm}$ and a temperature of $T = 25\,\mathrm{mK}$ are also listed in table 6.2.

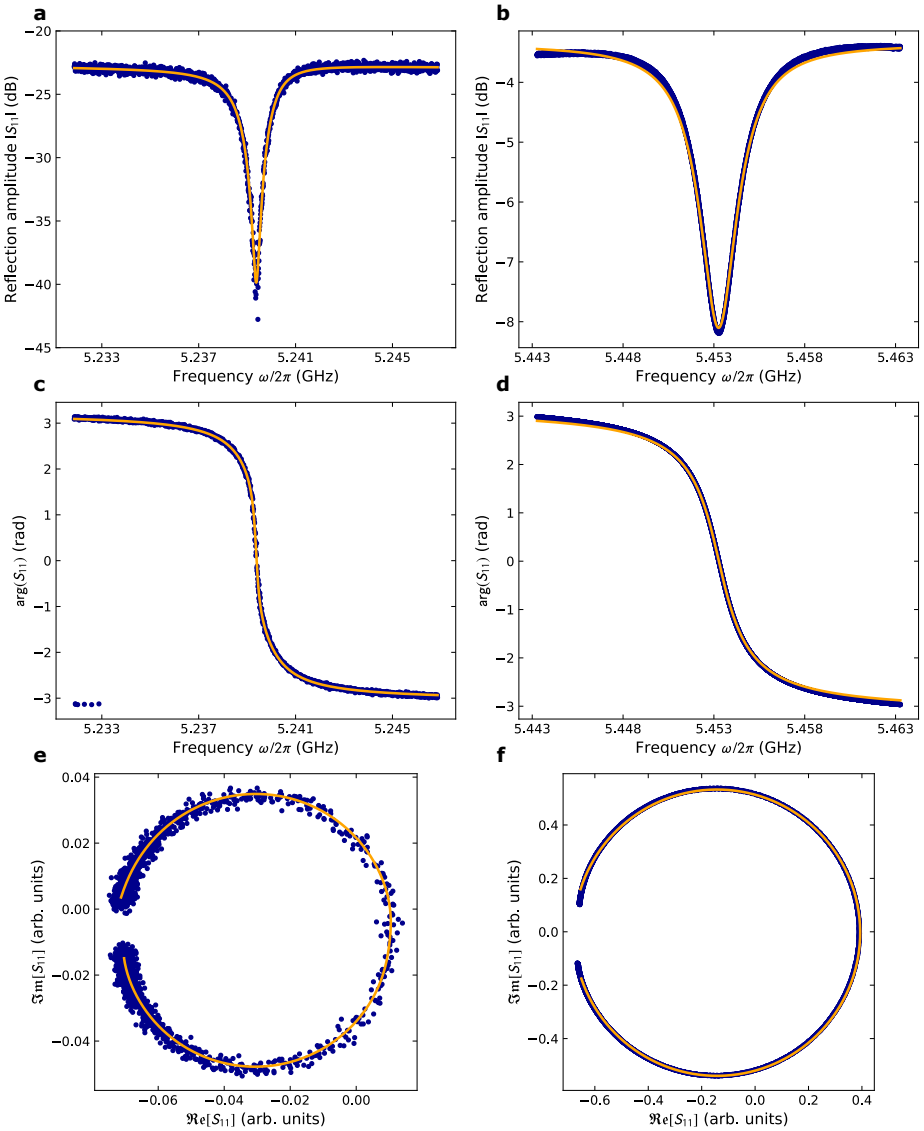

Figure 6.2: Cavity resonance measurements We plot the reflection spectra of the TE_{102} resonances and plot the amplitude $|S_{11}|$ and phase $\arg(S_{11})$ against the probe frequency, and the spectra's imaginary part $\mathfrak{Im}[S_{11}]$ against the real part $\mathfrak{Re}[S_{11}]$ for both the *mk_3* ((a), (c), and (e) at $T = 55\,\mathrm{mK}$ and $P = -140\,\mathrm{dBm}$) and the *mk_4* cavity ((b), (d), and (f) at $T = 25\,\mathrm{mK}$ and $P = -80\,\mathrm{dBm}$). The baseline difference of about 20 dB between plots (a) and (b) is the result of an additional attenuator in the system.

7 Magnetic linewidth measurements

This chapter focuses on experiments on a coupled magnon-photon system as described in Ch. 2. A coupling of these two excitations results in a harmonic hybrid system. While we are able to decrease excess excitation by the temperature of the environment and can control the excitation power we use to probe the system, the excitation is still Boltzmann-distributed over all possible evenly spaced excitation levels.

We focus on the internal magnon linewidth that we extract from the microwave reflection spectrum of the coupled system and sweep temperature and excitation power to identify the dominant loss mechanism in the different environment regimes. This is an important step towards more sophisticated utilization of magnetic components in combination with superconducting qubits, which are operated at millikelvin temperatures in the single photon regime.

7.1 Linewidth from 300 K to 2.4 K

In a cooperation with the University of Mainz, we first characterize our YIG sample in a different measurement setup at higher temperatures. We measure the magnetic linewidth of a YIG sphere from room temperature down to about 2.4 K [76]. The measurements are carried out similarly to the ones at millikelvin temperatures described in more detail in Ch. 5, but at fixed microwave excitation power.

The system consits of a YIG sphere with a diameter of $d = 0.5\,\mathrm{mm}$ mounted in a reflection cavity with a frequency of 6.53 GHz. With a ^{4}He continuous flow cryostat we are able to sweep the temperature from 2.4 K to 290 K in a single measurement run and apply the required static magnetic field of 227 mT with a superconducting coil. The exact experimental details and measurement data can be found in Ref. [76]. The evaluated data for the magnon linewidth κ_m is shown in Fig. 7.1.

We observe an increase of the magnon linewidth with increasing temperatures from $\kappa_\mathrm{m}/2\pi = 1.16 \pm 0.14\,\mathrm{MHz}$ at $T = 2.4\,\mathrm{K}$ towards a dominant peak at about 40 K and decreasing with a relatively broad second maximum around 100 K to about

$\kappa_m/2\pi = 1.61 \pm 0.25\,\mathrm{MHz}$ at room temperatures. The main contribution to the linewidth in this temperature range is attributed to slow-relaxing rare-earth ion impurity scattering [119, 123, 124], see Sec. 2.5.1.

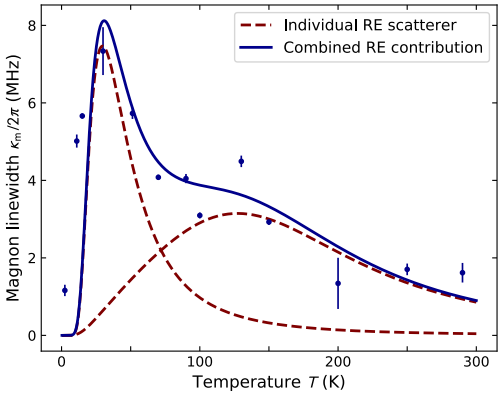

Figure 7.1: Magnon linewidth for temperatures from 2.4 K to 290 K We model the linewidth with two separate curves considering two rare-earth impurity scatterers with temperatures $\hbar\Omega_1/k_B = 43\,\mathrm{K}$ and $\hbar\Omega_2/k_B = 90\,\mathrm{K}$ (dashed red lines). These contributions sum up to the blue line. The measured magnon linewidth at single kelvin temperatures is attributed to two-magnon scattering processes at the rough sample surface. The estimated contribution of $\kappa_{surface}/2\pi \approx 1.1\,\mathrm{MHz}$ compares well to the measured $1.61 \pm 0.25\,\mathrm{MHz}$ at 2.4 K.

Using Eq. (2.61), we are able to model the linewidth data with two separate RE scatters with temperatures of $\hbar\Omega_1/k_B = 43\,\mathrm{K}$, a linewidth of 7 MHz and $\hbar\Omega_2/k_B = 90\,\mathrm{K}$ with a linewidth of 3.5 MHz (red dashed lines), and combine them to the blue line, which matches our linewidth data well.

At the lowest temperatures our data deviate from the curve modeling the slow-relaxing impurities that vanishes at 10 K. We attribute this to contributions from two-magnon scattering processes at the rough sample surface [125–127], see Sec. 2.5.2. We use Eq. (2.63) to model the influence of the surface scattering to our linewidth data. We describe the surface by hemispherical pits with a size of 2/3 of the roughness of the polishing material [128], $r_{pit} = 2/3 \times 50\,\mathrm{nm}$. We determine the saturation magnetization to be $\mu_0 M_s = 282\,\mathrm{mT}$. This results in a surface scattering contribution of $\kappa_{surface}/2\pi \approx 1.1\,\mathrm{MHz}$, matching well our measured linewidth of $\kappa_m/2\pi\,(T = 2.4\,\mathrm{K}) = 1.61\,\mathrm{MHz}$.

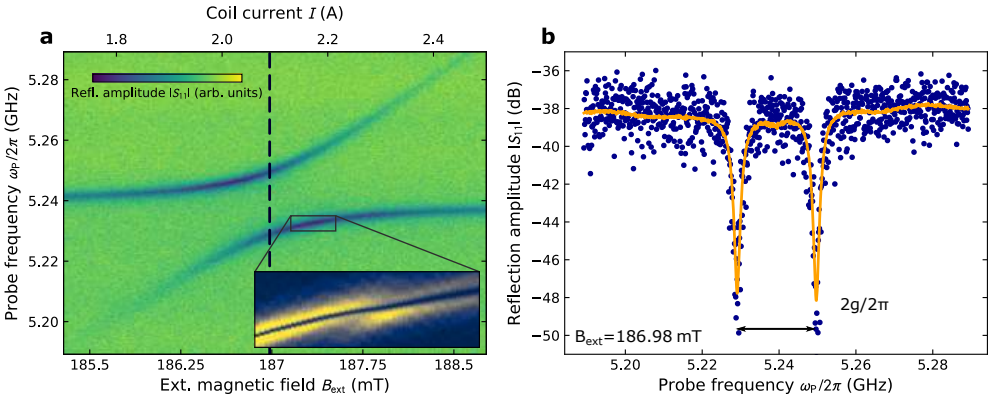

Figure 7.2: Cavity magnon polariton in the quantum regime of excitation (a) We plot the absolute value of the reflection spectrum $|S_{11}|$ (color coded) with respect to the probe frequency and the applied current at a temperature $T = 55\,\text{mK}$ and a probe power $P = -140\,\text{dBm}$. The resonance dips show the dressed photon-magnon states, which form an avoided level crossing towards a frequency degeneracy point at $I_0 = 2.09\,\text{A}$, corresponding to an applied magnetic field of $B_0 = 186.98\,\text{mT}$ (dashed vertical line). The inset displays the squared gradient of the zoomed-in amplitude data. The kink in the data represents a weakly coupled magnetostatic mode. (b) Raw data of the cross section at the center of the avoided level crossing (black) and fit to input-output formalism following an adapted fit procedure (green). The data is normalized by the field independent background before fitting and the background is multiplied back to the fit to display it over the raw data. The fit yields a magnon linewidth of $\kappa_m/2\pi = 1.82 \pm 0.18\,\text{MHz}$ at these conditions.

7.2 Cavity magnon polariton in the quantum regime

We use a (different) YIG sphere with a diameter $d = 0.5\,\text{mm}$ together with the *mk_3* microwave cavity for further investigation on the loss mechanism of magnons in the quantum regime of excitations. The color-coded amplitude signal of a typical microwave reflection spectrum of the hybridized magnon-photon system for different magnetic field values is displayed in Fig. 7.2(a). The data was taken at a temperature of 55 mK with an excitation power of $-140\,\text{dBm}$ at the SMA input port of the cavity resonator. This power corresponds to an average number of $\langle n \rangle \approx 0.6$ total excitations in the system, shared between magnon and photon. We observe a large anticrossing as the Kittel mode hybridizes with the cavity photon at constant frequency and we see the two branches of the dressed system. Due to the strong coupling with a mode splitting of $2g$, we observe the two modes well outside of the frequency degeneracy point. In addition to the large anticrossing we observe a second smaller feature at slightly higher field strength, indicating the coupling of the photon mode to an additional magnetostatic mode within the YIG shpere. We enhanced the visibility of this feature by plotting the squared gradient of the data in the zoom-in insert plot. Since the second mode is only weakly coupled it does not form an anticrossing,

but only appears as a kink in the data. Such a magnetostatic mode is excited by a non-uniform ac magnetic field of the cavity resonance and are also reported in comparable experimental systems [61, 76].

Fig. 7.2(b) shows the raw data of the amplitude of the reflection spectrum (black) and the corresponding fit derived by input-output theory (green) for matching magnon and photon frequencies $\omega_m(B_0) = \omega_r$ at an applied coil current of $I_0 = 2.086\,\mathrm{A}$, corresponding to an applied external magnetic field of $B(I_0) = B_0 = 186.98\,\mathrm{mT}$. The current-to-field conversion derives from the known FMR dispersion relation for the Kittel mode in YIG and differs for different measurement dates and temperatures due to hysteresis effects in the permanent magnets.

7.2.1 System parameters

For the measurement depicted in Fig 7.2 we fit a bare resonator frequency $\omega_r/2\pi = 5.23902 \pm 2 \cdot 10^{-5}\,\mathrm{GHz}$, a 452 kHz decrease compared to the zero-current measurement, see table 6.1. The magnetic field created by the permanent magnets slightly dresses the resonator frequency even at zero current, which leads to an increase compared to the bare frequency. The magnon frequency is given by

$$\begin{aligned}\omega_m(I)/2\pi &= \omega_m^{I=0}/2\pi + c_m \cdot I \\ &= 4.9817 \pm 2 \cdot 10^{-4}\,\mathrm{GHz} + 122.0 \pm 0.1\,\frac{\mathrm{kHz}}{\mathrm{A}} \cdot I,\end{aligned} \tag{7.1}$$

which indicates a zero-current magnetic field of about $B_{\mathrm{off}} = 177.8\,\mathrm{mT}$. We find a coupling strength $g/2\pi = 10.39 \pm 0.17\,\mathrm{MHz}$ that is in good agreement with the theoretically predicted value of $g^{\mathrm{th}}/2\pi = 12.48\,\mathrm{MHz}$ from Eq. (2.32).

Table 7.1: Geometric system parameters For the theoretically predicted value of the coupling strength between magnon and cavity photon g_{th}, we simulate different parameters with finite element simulations. The table includes the mode volume V_{mode}, the overlap factor η, the sphere diameter d, the corresponding number of participating spins N_s, and the spin number s.

$V_{\mathrm{mode}}\ (\mathrm{m}^3)$	η	$d\ (\mathrm{mm})$	N_s	s
$5.406 \cdot 10^{-6}$	0.536	0.5	$1.37 \cdot 10^{18}$	5/2

We obtain the overlap factor $\eta = 0.535$, the ratio of mode volume in the cavity volume and the sample volume, used in the theoretical coupling formula from finite

element simulations using ANSYS HFSS [1]. For a sphere diameter $d = 0.5\,\mathrm{mm}$ we assume a total number of participating spins $N_\mathrm{s} = 1.37 \cdot 10^{18}$ with a spin number $s = 5/2$. The geometric system parameters are also listed in table 7.1.

We estimate the background signal strength from the measurement setup (Sec. 5.7) and fit the reflection spectrum at the degeneracy point, i.e. at matching magnon and photon frequencies to the modified formula derived by the input-output formalism, Eq. (5.1) and extract an intrinsic magnon linewidth $\kappa_\mathrm{m}/2\pi = 1.82 \pm 0.18\,\mathrm{MHz}$. The coupling strength exceeds both the total resonator linewidth κ_l and the internal magnon linewidth of κ_m, thus being well in the strong coupling regime. While the linewidth is comparable to the value for room temperature measurements, it is significantly larger than the one at $T = 2.4\,\mathrm{K}$ [76]. The fit results for all relevant system parameters are also listed in table 7.2.

Table 7.2: Cavity magnon polariton fit parameters The hybrid system parameters are determined by multiple measurements and fit routines to reduce the total number of free fit parameters per routine. The table includes the bare resonator frequency ω_r, the zero-current magnon frequency $\omega_\mathrm{m}^{I=0}$, the coupling strength g, and the offset magnetic field created by the permanent magnets B_off.

$\omega_\mathrm{r}/2\pi$ (GHz)	$\omega_\mathrm{m}^{I=0}/2\pi$ (GHz)	$g/2\pi$ (MHz)	B_off (mT)
$5.23902 \pm 2 \cdot 10^{-5}$	$4.9817 \pm 2 \cdot 10^{-4}$	10.39 ± 0.17	177.8

7.2.2 TLS losses in magnets

In order to identify the dominant magnetic loss mechanism at mK temperatures we study the magnetic linewidth with respect to small temperature and power changes compared to the quantum excitation limit. At the degeneracy point we evaluate κ_m at two power values, $-140\,\mathrm{dBm}$ and $-65\,\mathrm{dBm}$ in a temperature range between 55 mK and 1.8 K and for detailed power sweeps with the input varying between $-140\,\mathrm{dBm}$ and $-65\,\mathrm{dBm}$ at two constant temperatures, 55 mK and 200 mK. The evaluated data are shown in Fig. 7.3. The cavity parameters and the coupling strength are not influenced by these temperature changes. By performing the data evaluation for each temperature stage on its own we compensate the hysteresis in magnetic field performance in the temperature sweep. The applied excitation power result on average in magnon numbers from $\langle m \rangle = 0.31$ to $\langle m \rangle = 9.85 \cdot 10^6$, with the corresponding scale also plotted in the the upper x-axis of Fig. 7.3(b). The

[1] ANSYS, Inc., `https://www.ansys.com` - accessed Oct. 18, 2019

number of magnons is still much smaller than the number of participating spins on the order of 10^{18}, therefore we expect a fully linear behavior of the magnons in contrast to intrinsic non-linear magnon behavior that is observed at magnon numbers comparable to the number of participating spins [58].

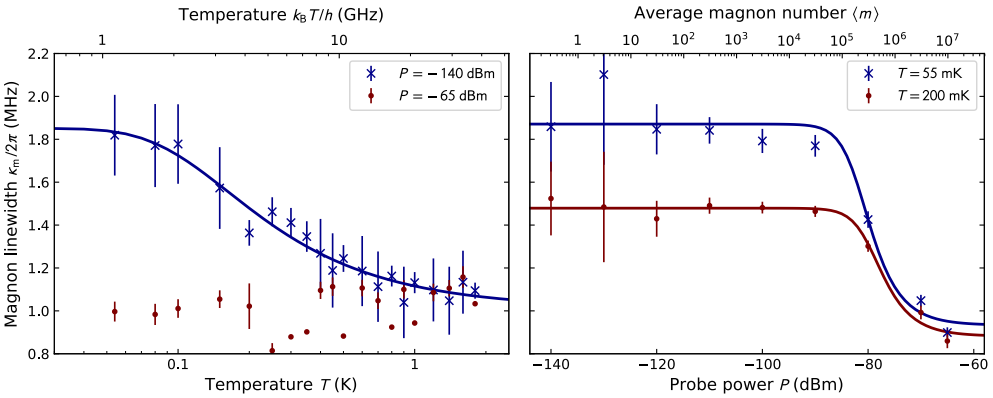

Figure 7.3: Magnon linewidth in the quantum regime of excitation (a) Temperature dependence of the magnon linewidth κ_m for different probe powers. At low powers, the linewidth decreases with increasing temperature. We fit the $\tanh(1/T)$ trend from the standard tunneling model to the data, indicating that the linewidth is TLS loss limited in the quantum regime of excitation. The data at high powers (circles) do not follow this trend. The TLSs are already saturated by thermal excitation and the linewidth remains constant. (b) Power dependence of the magnon linewidth κ_m for $T = 55\,\mathrm{mK}$ and 200 mK. The temperature curves show a similar behavior. The linewidth stays constant for low probe powers and we observe a drop in κ_m at powers of about $-90\,\mathrm{dBm}$. We fit a $1/\sqrt{(1 + P/P_c)}$ trend of the TLS model to both data sets and retrieve a similar critical power as well as matching κ_0 and κ_{off} for both temperatures. All linewidth data shown here are extracted from the fit at matching frequencies.

The magnetic linewidth decreases going to higher temperatures at small excitation power, but stays constant for the measurements at high excitation power, with the strong excitation linewidth matching the high temperature data at small excitation, Fig. 7.3(a). In the power sweep, κ_m decreases at both temperatures with increasing excitation power, Fig. 7.3(b). We attribute this behavior to excitation losses into a bath of two level systems, see Sec. 2.5.3. The TLSs become saturated either by thermal energy at higher temperatures or resonant power absorption by the strong excitation. At strong excitation in the temperature sweep, all TLSs are saturated and κ_m stays constant. We expand the function describing TLS losses, Eq. (2.73), by an offset linewidth κ_{off}, which describes the magnetic linewidth without TLS influence,

$$\kappa_m(T,\ P) = \kappa_0 \frac{\tanh(\hbar\omega_r/2k_B T)}{\sqrt{1 + P/P_c}} + \kappa_{off}. \tag{7.2}$$

From the fit, we determine the low temperature limit of the linewidth describing the TLS bath within the sample $\kappa_0/2\pi = 1.05 \pm 0.15\,\mathrm{MHz}$ and the critical power $P_c = -81.0 \pm 6.5\,\mathrm{dBm}$ at the SMA port. We obtain the offset linewidth $\kappa_{off}/2\pi = 0.91 \pm 0.11\,\mathrm{MHz}$ as a lower boundary for the internal linewidth without any TLS contribution in the saturation limit. We neglect the power dependence $1/\sqrt{1+P/P_c}$ in the fit to the temperature sweep data in Fig. 7.3(a) since we operate in the single excitation regime with $P \ll P_c$. The fit parameters to the TLS models are also listed in table 7.3.

The high power data in Fig. 7.3(a) increases slightly at temperatures of about 1 K. We attribute this to the increasing contribution of scattering losses at rare earth impurities within the sample, which we also observe in Ref. [76].

Table 7.3: Fit parameters to the TLS loss model The table includes the low temperature limit of the magnon linewidth κ_0, its lower boundary without TLS contribution κ_{off}, and the critical excitation power P_c.

$\kappa_0/2\pi$ (MHz)	$\kappa_{off}/2\pi$ (MHz)	P_c (dBm)
1.05 ± 0.15	0.91 ± 0.11	-81.0 ± 6.5

The linewidth decrease in the temperature sweep shows the thermal excitation of the resonator, where we recover the temperature corresponding to the resonator frequency, $\hbar\omega_r = k_B T_r$, with $T_r = 251.4\,\mathrm{mK}$ at half the TLS-induced linewidth change. The corresponding frequency scale to express the temperature is plotted on the upper x-axis in Fig. 7.3(a).

With our measurements and the fits in Fig. 7.3, we can confirm incoherent coupling in a bath of TLSs as the dominant loss mechanism of magnons in the quantum limit of excitation and extend temperature dependent measurements [61] by including the power dependent measurements and analysis as well [62]. A similar behavior is also reported in thin film YIG structures [64].

7.2.3 Linewidth outside of the anticrossing

So far, only the magnetic linewidth at zero frequency detuning was considered, where the energy in the system is equally shared between magnon and photon. We now want to observe the power dependence of the magnon linewidth at constant input power and instead control the energy in the magnon via frequency detuning. At constant input power, the magnon excitation depends on the frequency detuning

because fewer magnons are excited at off-resonant applied fields. Figure 7.4 shows the magnetic linewidth with respect to the applied magnetic field at temperatures $T = 55\,\mathrm{mK}$ (subplot (a)) and $T = 200\,\mathrm{mK}$ (subplot (b)). The corresponding magnon frequency is displayed on the upper x-axes and dashed horizontal lines mark the cavity resonance frequency. The different excitation powers are color coded and the legend is valid for both plots. We only display the highest excitation powers that show the decrease in linewidth. The x- and y-axis scaling is identical for both plots.

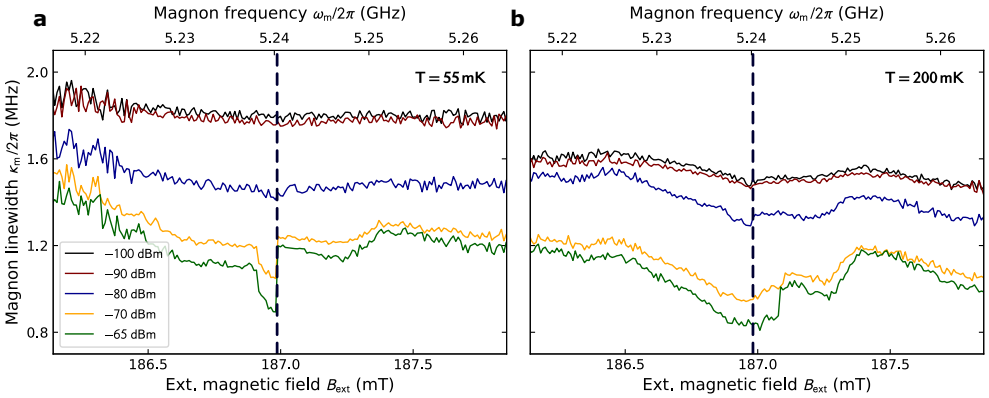

Figure 7.4: Magnon linewidth outside of the anticrossing We plot κ_m against the external magnetic field for different probe powers at $T = 55\,\mathrm{mK}$ (a) and $T = 200\,\mathrm{mK}$ (b). The depicted probe powers correspond to the ones at the linewidth decrease in Fig. 7.1(b). The linewidth shows a global minimum in the anticrossing (dashed line), here we observe the strongest TLS saturation effects since the number of excited magnons is at its maximum. We observe local minima at 187.25 mT external magnetic field that correspond to the coupling to an additional magnetostatic mode within the sample (see inset of Fig. 7.2(a)). The linewidth increases with higher frequency detuning and reaches the TLS-influenced values outside of the crossing.

For both temperatures we find a minimum of the magnon linewidth at matching frequencies at an external magnetic field of about 187 mT and the linewidth increases with the frequency detuning $\Delta = \omega_\mathrm{r} - \omega_\mathrm{m}$ to match the low power values.

At highest powers we observe for both temperatures a second local minimum at about 187.25 mT external field. We attribute this to the coupling to an additional magnetostatic mode within the YIG sphere, due to a non-uniform microwave magnetic field at the sample. This magnetostatic mode is also faintly visible in the color plot of the anticrossing. The inset plot in Fig. 7.2(a) shows the squared gradient of the zoomed-in amplitude data, where the small kink shows the weak coupling to the second magnetic mode. This accidental excitation of a magnetic mode has also been reported in similar experimental data [61, 76]. Coupling to a second mode increases the number of excited magnons and saturates more TLSs, which results

in the local minimum in the linewidth data. We cannot explain the instantaneous increase in linewidth in the $T = 55\,\mathrm{mK}$ data in the vicinity of the anticrossing.

We further quantify the energy ratio by which the Kittel mode is excited. Two resonating system that hybridize mix by a given amount depending on the frequency detuning. Since we only have direct access to the cavity, we calculate the energy stored in both branches as seen from the cavity and than weigh the energy ratio in the with the corresponding magnon/photon mixing ratio in each branch. Each anticrossing is separeted in its upper (+) and lower (-) branch, where we individually fit the resonances in each branch at the tracked dressed resonance frequencies with the circle fit algorithm [82, 83]. From the fit we obtain the total energy in units of excitations numbers for each branch,

$$E_{\pm} = 4\frac{Q_{\mathrm{l},\pm}^2}{Q_{\mathrm{c},\pm}}\frac{1}{\hbar\omega_{\mathrm{r},\pm}^2}P_{\mathrm{in}}. \tag{7.3}$$

with corresponding energy ratios

$$E_{\pm}^{\mathrm{ratio}} = \frac{E_{\pm}}{E_{+}+E_{-}}. \tag{7.4}$$

The used quality factors are the ones determined by circle fits of both Lorentzian dips and not the ones obtained by the pure cavity measurements.

Each branch has a distinct mixing ratio of magnon and photon share, depending on the frequency detuning. This is reflected in the components of the eigenvectors $X_{\pm}$ of the coupling matrix A in Eq. (2.39),

$$X_{\pm} = \begin{pmatrix} X_{\pm}^{(1)} \\ X_{\pm}^{(2)} \end{pmatrix} = \frac{1}{\sqrt{2\Omega}}\begin{pmatrix} \pm\sqrt{\Omega \mp \Delta} \\ \sqrt{\Omega \pm \Delta} \end{pmatrix}, \tag{7.5}$$

with $\Omega = \sqrt{\Delta^2 + 4g^2}$. The magnon/photon mixing ratio is given by the squares of the corresponding components of the eigenvectors. Due to symmetry reasons the magnon share m in one branch is equal to the photon share p in the other branch at any given Δ. Since we monitor the resonance mode of the cavity, we always observe a photon ratio larger than (or equal to) the magnon ratio. This leaves us with

$$m_{\pm} = p_{\mp} = \left|X_{+}^{(1/2)}\right|^2. \tag{7.6}$$

The total energy ratio in the magnon $E_{\mathrm{m/p}}^{\mathrm{ratio}}$ is the sum of the magnon/photon energy from both branches,

$$E_{\mathrm{m}}^{\mathrm{ratio}} = \left|X_{+}^{(1)}\right|^2 E_{+}^{\mathrm{ratio}} + \left|X_{+}^{(2)}\right|^2 E_{-}^{\mathrm{ratio}} \tag{7.7}$$

$$E_{\mathrm{p}}^{\mathrm{ratio}} = \left|X_{+}^{(2)}\right|^2 E_{+}^{\mathrm{ratio}} + \left|X_{+}^{(1)}\right|^2 E_{-}^{\mathrm{ratio}} = 1 - E_{\mathrm{m}}^{\mathrm{ratio}}. \tag{7.8}$$

The energy ratios for the measurements at -65 dBm excitation power are displayed in Fig. 7.5 with the same x- and y-axes and scaling for both subplots and representing the same magnetic field section as in Fig. 7.4. As expected, we observe the maximum magnon excitation ratio at zero detuning with 50 % of excitation and a decrease to 20 % excitation share at the borders of the subplots. The coupling to the second magnetic mode and the increase in magnon number is also visible as a local maximum at both temperatures.

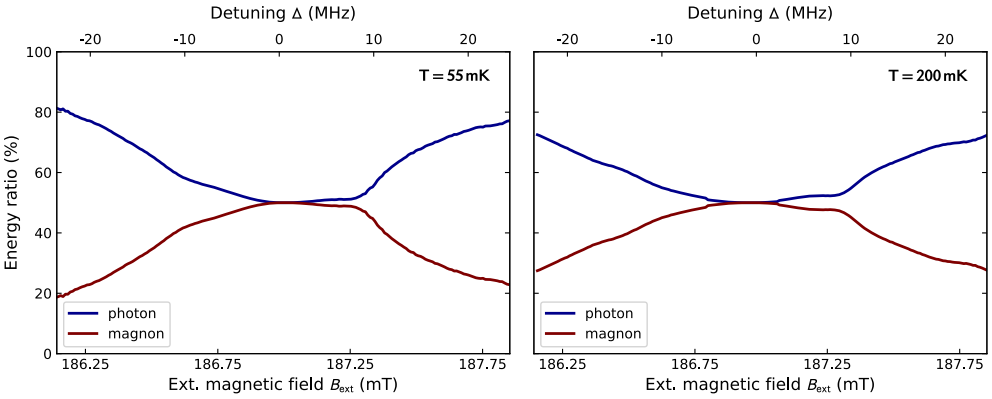

Figure 7.5: Energy ratio stored in the magnetic sample and the cavity photon The magnon energy ratio shows the coupling to the second magnetostatic mode at 187.25 mT. The ratio drops from the maximum at $\Delta = 0$ to 20 % at the plot boundaries. The x-axes scaling is the same as in Fig 7.4. (a) 55 mK, (b) 20 mK.

7.2.4 Possible origin models for magnetic TLSs

The microscopic origins of TLS losses in magnetic material (and for that matter, dielectric TLSs as well) is not fully understood yet and part of ongoing research. There are multiple possible explanations why TLS losses are observed, such as magnetic TLSs, surface spins or magnon-photon coupling.

Magnetic TLSs were proposed with an analog behavior to electric dipolar coupled TLSs [186–189] and measured in spin glasses by thermal conductivity, susceptibility and magnetization measuements at low temperatures [190, 191]. Amorphous YIG shows spin glass behavior [192] and therefore it is plausible to observe these effects in our crystalline YIG sample as well. With already observed rare earth impurities in our sample [76], it is likely that it contains structural crystal defects as well. This is again analogous to materials with electric dipolar coupled TLSs, where TLSs appear largely in disorderd crystals but were also detected in smaller densities in single crystals [193].

Another possible origin of the losses could be surface spins, since they were observed as an important loss mechanism in cQED experiments [147, 148] showing TLS loss behavior. In such a case we would find a changing number of participating spins in our system. We evaluate the coupling strength g to find a power or temperature dependence and observe such a change in N_s, see Fig. 7.6. We find an increase in the coupling strength of about 1 % at the saturation conditions for the TLSs. With $g \propto \sqrt{N_s}$ this translates to an increase in the number of participating spins on the order of 2 %, possibly due to an increased participation of spins on the surface that do not contribute to the coupling strength at low excitation.

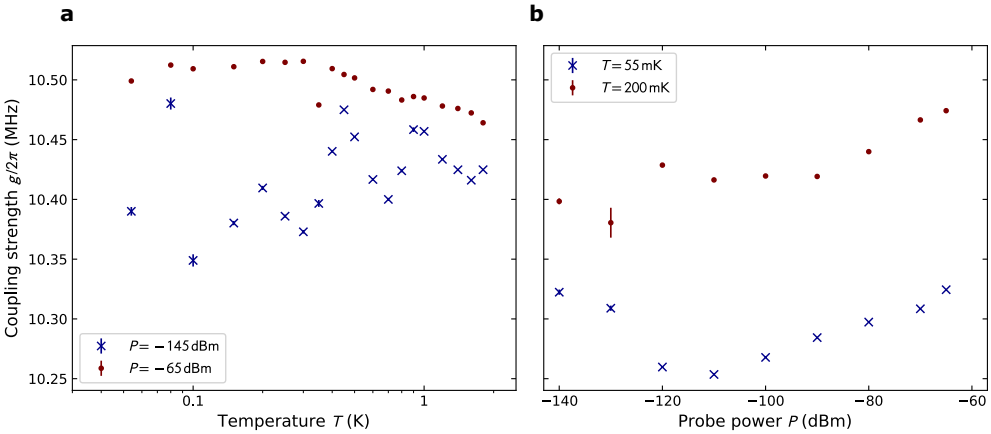

Figure 7.6: Power and temperature dependence of the coupling strength The temperature dependence (a) and power dependence (b) of the coupling strength evaluated at the same conditions as shown in Fig. 7.3. At constant input power, the coupling strengths shows no conclusive temperature trend with little changes. At constant temperatures it increases by an order of 1 % at high excitation powers. From these increase in coupling strength we obtain an increase in participating spins on the order of 2 %. Due to the small calculation error, most error bars are not visible in the plot. The numerical values for the coupling strength at matching conditions in both subplots do not necessarily match, since these measurements were carried out during different cool-downs which influences the exact geometric shape of the copper cavity.

A loss mechanism by magnon-phonon coupling and subsequent phonon losses due to TLS coupling is neglected because these magnon losses are expected to be much smaller than the Gilbert damping [194] for Kittel mode magnons with wave vector $\mathbf{k} = 0$ in YIG.

8 Magnon based nonlinear quantum system

In this chapter we introduce the transmon qubit as a nonlinear element into the experimental system. Coupling the qubit to the magnetic excitations allows us to individually address single magnons in the system. We explore two different coupling regimes with two different microwave cavities. First, we create an indirectly coupled qubit-magnon system that is located in the dispersive regime and read out via standard qubit measurements. In a second step, we match the cavity frequency to the qubit frequency and create a strongly coupled system of all three components; magnon, photon, and qubit.

First, the qubit is characterized in the cavity with spectroscopic and time resolved measurements without any applied current. We then measure the coupled system in the dispersive limit and focus lastly on the strong coupling regime, where we perform power and temperature sweeps complemented by corresponding analytic fits and simulations.

8.1 Qubit characterization

We first characterize the Josephson junction in the transmon qubit with resistance measurements at room temperature. From spectroscopic measurements at millikelvin temperatures we obtain the qubit transition frequencies and determine the characteristic qubit energies E_J and E_C. We calibrate the excitation number in the TE_{103} mode by the ac Stark shift [16], a power dependent shift of the qubit frequency, to later operate our system in the single photon regime, and measure the dissipative dynamics with pulsed time domain measurements. All these measurements are performed using the *mk_3* cavity without any applied current.

Fig. 8.1 shows a false-colored micrograph image of the used transmon qubit chip. The design is largely dominated by the pads of the shunt capacitor on both sides of the Josephson junction. The junction itself a size of approximately $100 \times 95\,\mathrm{nm}^2$ and cannot be resolved in the optical images even at a 100x optical zoom level and is

sketched schematically into the picture. The normal state resistance of the junction $R_n = 7.51\,\mathrm{k}\Omega$, is obtained with a 2-point probe setup at room temperature. Using the Ambegaokar-Baratoff relation between junction resistance and the critical current I_c [195] we find

$$I_c = \frac{\pi\Delta}{2e}\frac{1}{R_n} = 71.11\,\mathrm{nA}, \tag{8.1}$$

with the superconducting gap energy of Al, $\Delta = 3.4 \cdot 10^{-4}\,\mathrm{eV}$. This critical current translates to a Josephson energy $E_J^{300} = 35.3\,\mathrm{GHz} \cdot h$, which we combine with the simulated charging energy $E_C^{\mathrm{sim}} = 277.8\,\mathrm{MHz} \cdot h$ to result in a characteristic energy ratio $E_J/E_C = 127.1$ and an expected qubit transition frequency $\omega_{01}^{300}/2\pi = 8.58\,\mathrm{GHz}$ based on the room temperature measurements. Comparing these values with the measured qubit frequency and energy ratio measured at millikelvin temperatures and discussed below, where we find a significant deviation from the expected value.

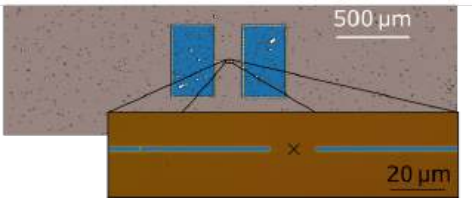

Figure 8.1: Transmon qubit chip False colored micrograph of the transmon qubit. The capacitor pads dominate the geometrical design of the structure, with only small connecting Al strips leading to the Josephson junction. The junction itself with an estimated size of $100x95\,\mathrm{nm}^2$ is too small to be seen here even in the zoom-in and is only depicted schematically.

8.1.1 Spectroscopic measurements

We install the qubit chip into the cavity box, cool the system down to 25 mK, and probe it with continuous microwaves using the spectroscopy setup to measure the qubit transition frequency and the coupling strength between qubit and cavity resonator. The qubit transition frequencies are observed as dips in the dispersive shift measurements of the TE_{103} readout mode frequency at $\omega_{103}/2\pi = 6.64\,\mathrm{GHz}$ with respect to the qubit probe frequency and probe power, see Fig. 8.2(a). We observe multiple dips appearing and broadening at increasing probe powers, of which we identify the two dips at the highest frequencies with the energetically lowest qubit transitions. The fundamental $|0\rangle \rightarrow |1\rangle$ transition at $\omega_{01}/2\pi = 5.4315\,\mathrm{GHz}$ and the

two photon $|0\rangle \rightarrow |2\rangle$ transition at $\frac{1}{2}\omega_{02}/2\pi = 5.3526\,\mathrm{GHz}$. With Eq. (3.24) we find for the characteristic energies

$$E_\mathrm{C} = 2\left(E_{01} - \frac{1}{2}E_{02}\right) = 167.8\,\mathrm{MHz}\cdot h, \tag{8.2}$$

$$E_\mathrm{J} = \frac{(E_{01}+E_\mathrm{C})^2}{8E_\mathrm{C}} = 23.355\,\mathrm{GHz}\cdot h, \text{ and} \tag{8.3}$$

$$E_\mathrm{J}/E_\mathrm{C} = 139.2. \tag{8.4}$$

This positions our qubit well in the transmon regime. We identify the third dip in the dispersive shift spectrum at 5.252 GHz as the $|1\rangle \rightarrow |2\rangle$ and the three photon $|0\rangle \rightarrow |3\rangle$ transitions, which are expected at the same frequency. Based on the calculated parameters we would expect these transition at $\omega_{12}/2\pi = 5.265\,\mathrm{GHz}$, indicated by the corresponding dashed line in Fig 8.2(a).

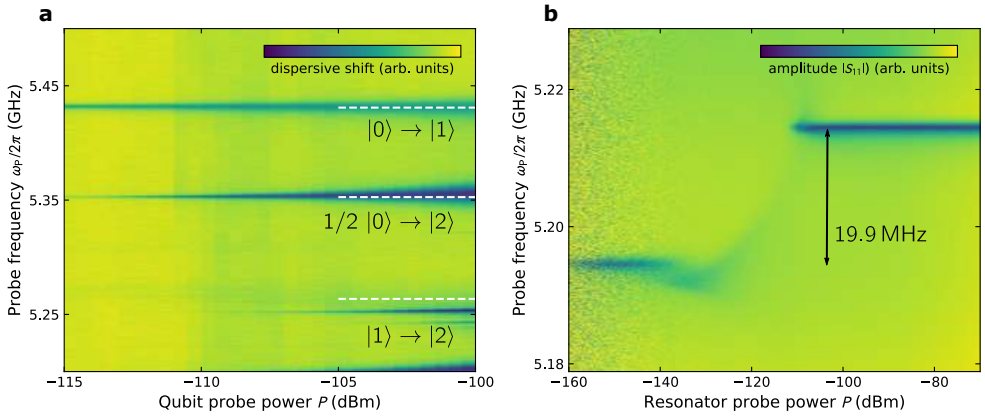

Figure 8.2: Spectroscopic measurements, qubit transitions and qubit-resonator coupling (a) The first transitions frequencies are obtained by evaluating the dips in the dispersive shift spectrum of the TE_{103} readout mode that is $\Delta_{103}/2\pi = 1.14\,\mathrm{GHz}$ detuned from the qubit. The transition frequencies and the non-equidistant frequency spacing determine the characteristic qubit energies; $E_\mathrm{J} = 23.355\,\mathrm{GHz}\cdot h$, $E_\mathrm{C} = 167.8\,\mathrm{MHz}\cdot h$, and $E_\mathrm{J}/E_\mathrm{C} = 139.2$. The calculated $|1\rangle \rightarrow |2\rangle$ transition matches well with the corresponding signal. (b) The TE_{102} cavity mode (coupling mode) becomes dressed by the qubit presence (low power). At higher powers the qubit is saturated and the system decouples. The shift of nearly 20 MHz relates to a coupling between qubit and coupling mode of $g_{\mathrm{q},102}/2\pi = 66.26\,\mathrm{MHz}$.

The measured fundamental transition frequency and the characteristic energies differ significantly from the room temperature measurements. The simulated charging energy is 65 % higher than the measured E_C and the Josephson energy obtained from the critical current measurement is 51 % higher than the value of the millikelvin measurement. With the relative deviations similar for both energies, the characteristic

energy ratios match within 10 % accuracy. This results in a fundamental frequency that is 3.15 GHz lower than initially expected. However, this does not play a role in the usability of the qubit chip for further experiments.

We measure the coupling strength $g_{\mathrm{q},102}$ between qubit and the TE_{102} coupling mode via its Lamb shift. The cavity resonator frequency is influenced by the presence of the qubit, similar to the Lamb shift in atoms. The qubit-cavity coupling $g_{\mathrm{q},102}$ results from the frequency detuning between qubit and resonator mode, $\Delta_{102} = \omega_{102} - \omega_{01}$, and the frequency shift χ between the coupled and uncoupled resonator. We probe the system with varying powers around the cavity resonance to saturate the qubit and measure the bare resonator frequency, see Fig. 8.2(b) and find the resonator mode power shifted by $\chi_{102}/2\pi = -19.9\,\mathrm{MHz}$. With the frequency difference between cavity mode and qubit $\Delta_{102}/2\pi = -220.6\,\mathrm{MHz}$ we find [163]

$$\chi = \frac{g^2}{\Delta} \rightarrow g_{\mathrm{q},102}/2\pi = \sqrt{\chi_{102}\Delta_{102}}/2\pi = 66.26\,\mathrm{MHz}. \tag{8.5}$$

These measurements position our qubit in the dispersive regime with respect to the cavity resonances, where the frequency detuning between any resonator TE_{10p} mode is much larger than its coupling strength with the qubit, $\Delta_{10p} \gg g_{q,10p}$. This allows for the system to be described with the Jaynes-Cummings Hamiltonian, Eq. (3.29).

8.1.2 Excitation number calibration

In contrast to the estimation in the magnon-polariton case, Sec. 6.1, we are here able use the ac Stark shift, a photon number dependent shift of the qubit frequency, to exactly calibrate the number of excitations $\langle n \rangle$ in the TE_{103} mode [16, 196–198], which is used as a reference for further experiments.

The approximately diagonalized Jaynes-Cummings Hamiltonian,

$$\hat{U}\hat{H}_{\mathrm{JC}}\hat{U}^{\dagger}/\hbar \approx \frac{1}{2}\left(\omega_{01} + \chi + 2\chi\hat{a}^{\dagger}\hat{a}\right)\hat{\sigma}_z + \omega_{\mathrm{r}}\hat{a}^{\dagger}\hat{a}, \tag{8.6}$$

contains a mixed term $\frac{g^2}{\Delta}\hat{\sigma}_z\hat{a}^{\dagger}\hat{a}$ that can be interpreted as a photon number dependent contribution to the qubit frequency, with

$$\Delta\omega_{01} = \frac{g_{\mathrm{q},103}^2}{\Delta_{103}}\langle n \rangle \tag{8.7}$$

describing the ac Stark shift of the qubit frequency.

We measure the qubit transition frequency versus the applied drive power at a probe power $P = -140\,\mathrm{dBm}$, see Fig 8.3(a). At an increased readout power we observe a

shift of the dressed transmon levels away from the readout mode, in our case to lower frequencies. We track the shifted qubit frequencies and fit the linear dependence on the excitation number,

$$\langle n_{103} \rangle = 12.69 \cdot P_{\text{in}}^{0.995} \text{fW}^{-1}, \tag{8.8}$$

with the coupling of the qubit to the TE_{103} readout $g_{103}/2\pi = 70.05\,\text{MHz}$ and a frequency difference $\Delta_{103}/2\pi = 1.14\,\text{GHz}$, see Fig. 8.3(b). This is a reduction of about a factor of 4.9 compared to the estimation of the population of the TE_{102} mode, Chap. 6. We attribute this to comparable Q factors at a higher resonance frequency, which leads to an overall smaller excitation number for the higher cavity mode. Based on the fit we perform the spectroscopic experiments in the dispersive limit at a readout power of $P_{\text{D}} = -130\,\text{dBm}$ corresponding to a single photon excitation.

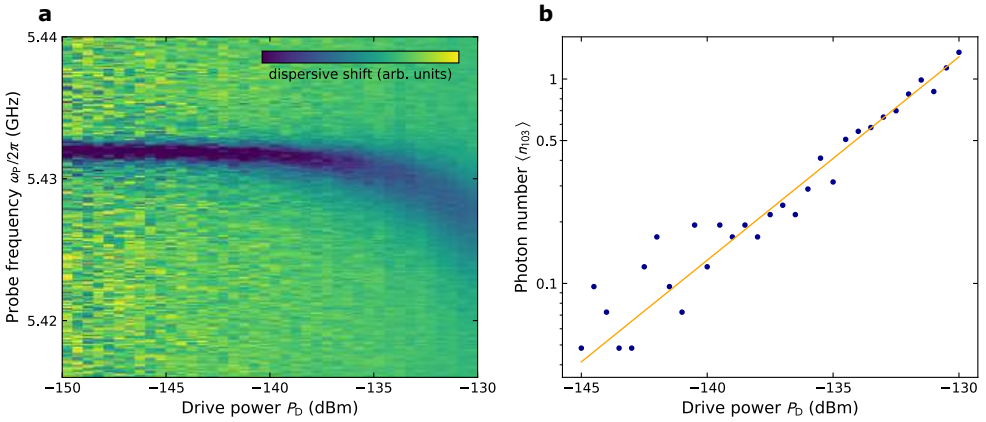

Figure 8.3: AC Stark measurement (a) By increasing the drive power on the readout resonator we populate the cavity with more photons. The qubit frequency becomes dressed and shifts away from the readout frequency. (b) We track the shift in qubit frequency in the AC Stark measurement and calculate the exponentially power dependent photon occupation in the cavity. This improves the accuracy compared to the estimation done in the magnon polariton experiments.

8.1.3 Time resolved measurements

We obtain the dissipation dynamics of the qubit, the energy relaxation time T_1 and the decoherence time $T_2^\star$, by pulsed measurements using the FPGA-based measurement setup described in Sec. 5.6.

We measure the energy relaxation time T_1 by applying a previously calibrated π pulse with a length of $T_\pi = 161.0\,\text{ns}$ that excites the qubit from $|0\rangle$ to $|1\rangle$ and measuring the qubit state after different waiting times Δt, see Fig. 8.4(a). Fitting an

exponential decay to the averaged qubit inversion, a measure for the probability to find the qubit in the excited state, we obtain $T_1 = 402.9\,\text{ns}$.

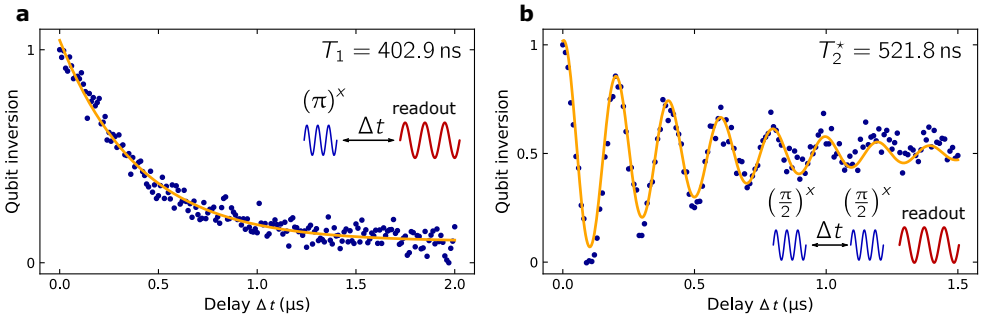

Figure 8.4: Measurement of the qubit lifetimes (a) Applying a previously calibrated π pulse rotates the qubit into the excited state. We measure the qubit state after different waiting times Δt and obtain an energy relaxation time $T_1 = 402.9\,\text{ns}$. (b) The decoherence time $T_2^\star = 521.8\,\text{ns}$ is measured with a Ramsey experiment, where the qubit state is rotated in a superposition state, evolves freely for times Δt on the equatorial plane, and is then rotated further around the x-axis. The applied pulse is frequency detuned from the qubit frequency by 5 MHz.

We measure the dephasing time $T_2^\star$ by a Ramsey pulse sequence, where we excite the qubit by a $\pi/2$ pulse in a superposition state on the equator of the Bloch sphere and let it evolve freely for times Δt without additional echo pulses, before rotating it by the same pulse and measuring the qubit state, see Fig. 8.4(b).

Table 8.1: Transmon parameters The table includes the first qubit transition frequency ω_q, the anharmonicity α, the characteristic energy ratio E_J/E_C, and the characteristic qubit times T_1 and $T_2^\star$.

$\omega_q/2\pi$ (GHz)	$\alpha/2\pi$ (MHz)	E_J/E_C	T_1 (s)	$T_2^\star$ (s)
5.4315	−179.5	139.2	402.9	521.8

The excitation pulse is detuned from the qubit frequency which results in Ramsey fringes [199], since the detuned $\pi/2$ pulse adds an additional oscillation to the qubit state that decays exponentially. Fitting our data, we recover the 5 MHz detuned excitation pulse and extract a dephasing time $T_2^\star = 512.8\,\text{ns}$. All transmon lifetimes are also listed in table 8.1.

We estimate the losses due to spontaneous Purcell emission via the cavity linewidth κ_r into the connected feed line to be $T_P = 1/\gamma_P = 1.138\,\mu s$ with

$$\gamma_P = \kappa_r \frac{g_{q,102}^2}{\Delta_{102}^2}. \tag{8.9}$$

While the 220 MHz detuning of the qubit to the TE_{102} coupling mode is quite small and leads to a relatively strong Purcell effect, our measured qubit lifetimes do not seem to be limited by these radiation losses.

8.2 Magnon-vacuum Rabi splitting in the dispersive limit

We create the quantum hybrid system between the Kittel mode and the superconducting transmon qubit in the dispersive limit with the magnon resonance frequency matching the fundamental qubit transition. The nonlinearity of the qubit allows us to address the individual energy levels of the system and access single magnon excitation, in contrast to the previously discussed purely classical experiments connecting magnon excitation with harmonic photon modes, where we simultaneously excited all energy levels with a Boltzmann distribution. While the direct coupling between the components is negligible, both couple to the TE_{102} coupling mode, which leads to an effective coupling via virtual photon exchange between qubit and magnon. The system stays in the dispersive regime with both frequencies far detuned from the coupling mode.

We tune the magnon frequency towards the qubit transition and monitor the dispersive shift of the TE_{103} readout mode while driving the system with a second tone in the vicinity of the qubit frequency in the single photon regime. The dispersive shift features a splitting in the qubit transition frequency that is attributed to a level hybridization due to a coherent exchange of excitation of the qubit and the Kittel mode with an effective coupling strength $\tilde{g}_{qm}^{0.5\,mm}/2\pi = 3.35 \pm 0.16\,MHz$, see Fig. 8.5. The coupling is mediated mainly by the TE_{102} mode, with an effective interaction Hamiltonian in the corresponding rotating frame, see Sec. 4.1,

$$\hat{H}_{int} = \hbar \tilde{g}_{qm}^{th} \left(\hat{q}^\dagger \hat{\sigma}_- + \hat{q} \hat{\sigma}_+ \right), \text{ with}$$
$$\tilde{g}_{qm}^{th} = \sum_p \frac{g_{m,10p} g_{q,10p}}{\omega_{10p} - \omega_q}.$$

Due to the unwarranted effort to create the needed magnetic field strength to measure $g_{m,103}$, applying a current of nearly 14 A, we only consider the contributions

of the TE_{101} and the TE_{102} mode to predict the effective coupling. With the measured coupling strengths connecting the individual components to the resonator modes we find

$$\tilde{g}_{\mathrm{qm}}^{\mathrm{th}\,0.5\,\mathrm{mm}}/2\pi \approx \left(\frac{5.89 \cdot 38.80}{1265.1} + \frac{10.39 \cdot 66.26}{220.6}\right) \mathrm{MHz} = 3.30\,\mathrm{MHz}. \tag{8.10}$$

We do expect the approximation to be valid, given a TE_{101} contribution to $\tilde{g}_{\mathrm{qm}}$ of only 0.18 MHz $\approx$ 5.4 %, and the estimated coupling strength matches well the measurement. The expected effective coupling strength is found as half the distance of the hybridized modes in Fig. 8.5(a) but, given the participating linewidths $\kappa_{\mathrm{r}}/2\pi = 850\,\mathrm{kHz}$, $\kappa_{\mathrm{m}}/2\pi = 1.8\,\mathrm{MHz}$, and $\kappa_{\mathrm{q}}/2\pi = \frac{1}{T_2^\star} = 1.95\,\mathrm{MHz}$, the effective coupling does not place the system in the strong coupling regime.

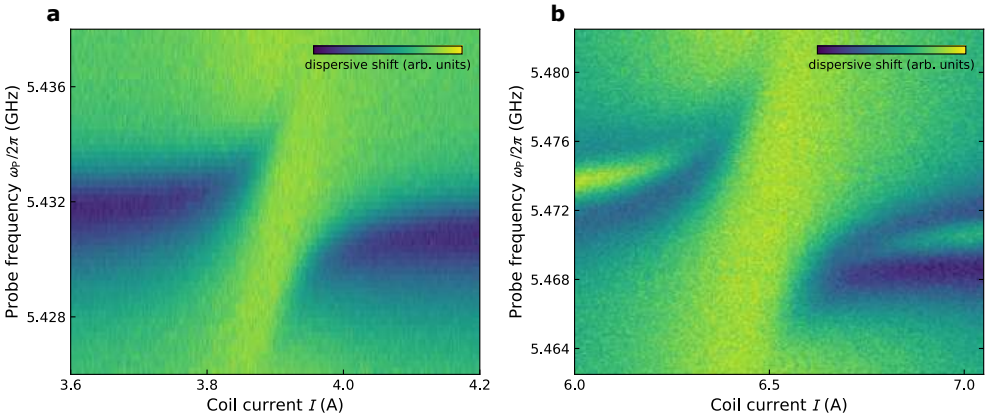

Figure 8.5: Magnon-vacuum Rabi splitting We hybridize the magnon and qubit excitation and measure the resulting magnon-vacuum induced Rabi splitting in the dispersive shift measurement of the driven system. The coupling strength is increased by exchanging the 0.5 mm YIG sphere (a) with a 1.0 mm YIG sphere (b), but the system does not stand in the strong coupling regime.

In order to increase the effective coupling we install a larger YIG sphere with a diameter of 1.0 mm, compared to the previously used 0.5 mm sphere, into the cavity. This results in a factor of $2^3 = 8$ times more participating spins and an expected increase of the effective qubit-magnon coupling by a factor of $\sqrt{8}$ to $\tilde{g}_{\mathrm{qm}}^{\mathrm{th}\,1.0\,\mathrm{mm}}/2\pi = 9.34\,\mathrm{MHz}$, which would position the system in the strong coupling regime. While the increased effective coupling strength of $\tilde{g}_{\mathrm{qm}}^{1.0\,\mathrm{mm}}/2\pi = 8.21 \pm 0.11\,\mathrm{MHz}$ is well visible in the the dispersive shift measurement in Fig. 8.5(b) and matches the expected value with an error on the order of 10 %, the overall signal to noise ratio is too weak to unambiguously show two resonance minima for one magnetic field value. Nevertheless, we clearly observe the effective qubit-magnon coupling in the dispersive limit and are able

to confirm the square root dependence of the coupling strength on the number of participating spins. All coupling strengths are presented together in table 8.2.

Table 8.2: Effective qubit-magnon coupling strength in the dispersive limit The table includes the measured effective qubit-magnon coupling strength $\tilde{g}_{\mathrm{qm}}$ and the theoretically expected value $\tilde{g}^{\mathrm{th}}_{\mathrm{qm}}/2\pi$ for two different YIG sample.

diameter (mm)	$\tilde{g}_{\mathrm{qm}}/2\pi$ (MHz)	$\tilde{g}^{\mathrm{th}}_{\mathrm{qm}}/2\pi$ (MHz
0.5	3.35 ± 0.16	3.30
1.0	8.21 ± 0.11	9.34

8.3 Strongly coupled tripartite system

With the previously measured qubit-magnon hybrid system in the dispersive regime, the next step is to bring all three participating systems on resonance with each other to create a strongly coupled system consisting of magnon, qubit, and photon.

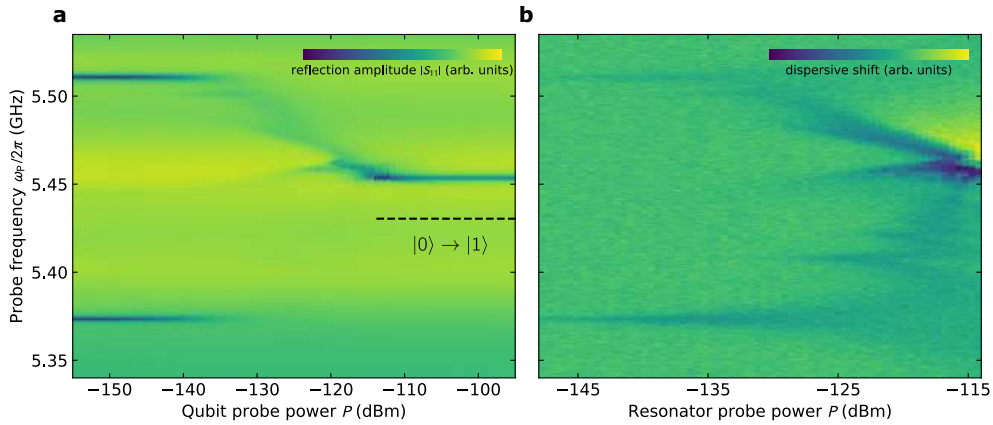

Figure 8.6: Strongly coupled qubit-photon system Power sweep of the reflection spectrum (a) and the dispersive shift measurement (b). The nearly frequency degenerate qubit-resonator system hybridizes and the dressed frequencies $\omega_{\mathrm{qr},\pm}$ are observed at low power excitation. Increasing the power saturates the qubit and only the cavity resonance is observed. We obtain a qubit frequency $\omega_{\mathrm{q}}/2\pi = 5.4304\,\mathrm{GHz}$ and a qubit-resonator coupling strength $g_{\mathrm{qr}}/2\pi = 67.65\,\mathrm{GHz}$

With the magnon representing a spin system, the qubit being an artificial atom, and the photon being a light quantum we therefore create a strongly coupled hybrid

system of light, matter, and spin. At the same time we increases the overall signal strengths and improve the signal to noise ratio by decreasing the frequency detuning between the photon coupling mode and the other two components. This is the next step towards more sophisticated implementations of magnetic components in quantum circuits that require coherent excitation exchange.

We first characterize the qubit in the cavity resonator in the strong coupling regime with respect to its frequencies and coupling strength, then tune the Kittel mode frequency on resonance to create the tripartite system. Different probe powers allow for the qubit-resonator coupling to be turned on and off to individually study the resonator-magnon coupling. The system parameters are determined by the two component measurements and the full tripartite measurement, where we compare the obtained frequencies and coupling strengths. We analyze the spectrum with a three-component analytic function based on the input-output formalism and simulate the spectrum and the eigenenergies of the full tripartite Hamiltonian with qutip [200], a open-source python package for simulating the dynamics of open quantum system. We study the thermal influences on the system and compare the simulated spectra to the data measured at the corresponding temperatures.

8.3.1 Strong qubit-resonator coupling

Since we work with a non tunable qubit, we adapt the cavity resonator frequency by installing all components in the *mk_4* cavity, whose TE_{102} coupling mode is designed to match the previously determined qubit transition frequency. The cavity resonance characteristics are discussed in Sec. 6.2. The cavity resonator hybridizes with the qubit and we observe hybridized qubit-resonator modes, in contrast to the Lamb shifted mode in the dispersive regime due to the presence of the qubit. Figure 8.6 shows a power sweep of the reflection spectrum measured directly with the VNA (a) and the corresponding dispersive shift measurement of the TE_{103} readout mode of the driven system (b) without applied current. The qubit is populated with increasing power and decouples from the resonator. We observe the two hybridized modes in the low power regime and the bare resonator frequency is observed at high probe powers. In the intermediate regime the excitation is distributed into multiple modes that are averaged out in the spectroscopic measurement.

The general scheme of the tripartite system is depicted in Fig. 4.1. We find two hybridized qubit-photon modes at $\omega_{\mathrm{qr},-}/2\pi = 5.373\,\mathrm{GHz}$ and $\omega_{\mathrm{qr},+}/2\pi = 5.510\,\mathrm{GHz}$ in the single photon regime and observe the bare cavity resonance at $\omega_{\mathrm{r}}/2\pi = 5.453\,\mathrm{GHz}$. The dressed frequencies are described analog to Eq. (2.40). We approximate the qubit in the weak excitation limit to only have a single transition

and are able to determine the qubit frequency $\omega_{01} = \omega_q$ and the qubit-resonator coupling g_{qr},

$$\omega_q = \omega_{qr,+} + \omega_{qr,-} - \omega_r = 5.4305\,\text{GHz} \cdot 2\pi \text{ and} \tag{8.11}$$

$$g_{qr} = \sqrt{\omega_r\omega_+ + \omega_r\omega_- - \omega_+\omega_- - \omega_r^2} = 67.60\,\text{MHz} \cdot 2\pi. \tag{8.12}$$

The dispersive shift measurement in subfigure (b) confirms the measurement of the reflection spectrum obtained directly by the VNA, with additional features in the transition regime between coupled and uncoupled system that we attribute to dressed states with higher qubit modes.

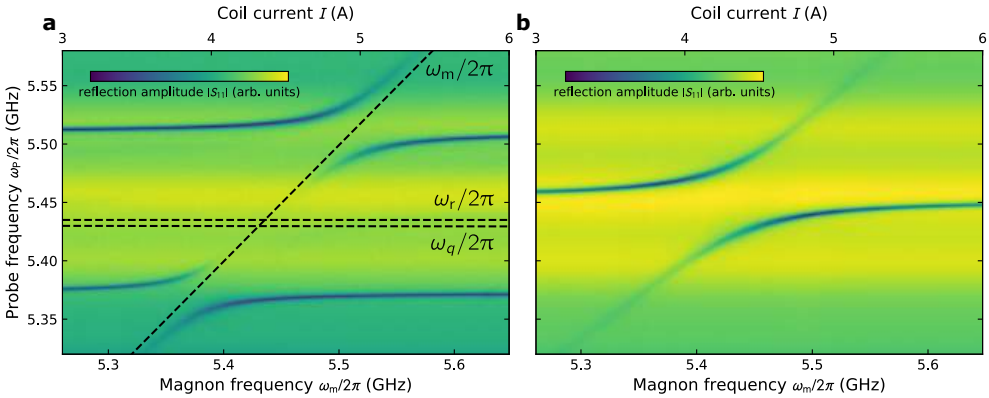

Figure 8.7: Current sweep of the tripartite system (a) We create the tripartite system with three resonance frequencies by tuning the Kittel mode frequency through the dressed qubit-photon states and fit the system by a constant cavity resonator frequency and two linearly changing frequencies for the Kittel mode and the qubit. The additional two anticrossing at the tripartite points have effective coupling strengths $\tilde{g}_1/2\pi = 18.71\,\text{MHz}$ and $\tilde{g}_2/2\pi = 23.07\,\text{MHz}$.(b) Decoupling the qubit from the system by applying a probe power $P = -95\,\text{dBm}$ recovers the magnon-polariton measurement similar to Sec. 7.2 and we obtain a resonator-magnon coupling strength of $g_{rm} = 30.41\,\text{MHz}$.

Comparing the system parameters with the previous measurements in the dispersive case using the *mk_3* cavity, we find the qubit frequency to be shifted by $-10\,\text{MHz}$. This is attributed to the temperature cycle of the sample during warm-up and cool-down, as well as the exposure to oxygen. The cavity coupling mode nearly matches the qubit frequency, being detuned only by $\Delta_{102} = 22.8\,\text{MHz}$. The qubit-resonator coupling remains nearly the same, with an increase of only 1.39 MHz despite a change in the effective qubit position with respect to the electric dipole of the cavity resonance field.

As sketched in Fig. 4.1(c) we create the tripartite quantum system by tuning the Kittel mode into resonance with the two hybrid qubit-resonator modes in the

single photon regime at a probe power $P = -145\,\mathrm{dBm}$. The measurement of the current sweep is depicted in Fig. 8.7(a), where we plot the color coded reflection amplitude against the probe frequency from the VNA and the applied current. We observe two anticrossings when all three components hybridize and obtain the two tripartite point at $I_1 = 3.909\,\mathrm{A}$ and $I_2 = 4.922\,\mathrm{A}$ with an effective coupling of $\tilde{g}_1/2\pi = 18.71 \pm 0.05\,\mathrm{MHz}$ and $\tilde{g}_2/2\pi = 23.07 \pm 0.08\,\mathrm{MHz}$, respectively. Probing with a power of $P = -95\,\mathrm{dBm}$ decouples the qubit from the system, see Fig. 8.7(b), and we observe the cavity magnon-polariton analog to in Sec. 7.2. The coupling strength of $g_{\mathrm{rm}} = 30.41 \pm 0.06\,\mathrm{MHz}$ is a factor of 2.93 larger compared to the measurements with the 0.5 mm diameter YIG sphere, which matches an expected 2.83 times larger value due to the increased number of participating spin quite well.

We fit the tripartite resonance frequencies to the eigenvalues of the coupling matrix, Eq. (4.6), considering the constant resonator frequency ω_{r} to be constant and the qubit frequency changing linearly with the applied magnetic field, see Sec. 4.3, and obtain

$$\omega'_{\mathrm{q}}/2\pi\,(I) = 5.430\,446\,\mathrm{GHz} - 171.7\,\mathrm{kHz}\frac{I}{\mathrm{A}} \text{ and} \tag{8.13}$$

$$\omega'_{\mathrm{m}}/2\pi\,(I) = \left(4.8742 + 0.1286\frac{I}{\mathrm{A}}\right)\mathrm{GHz}. \tag{8.14}$$

The frequencies are also sketched into Fig. 8.7(a). The individual coupling strengths are fitted to

$$g'_{\mathrm{qr}}/2\pi = 67.49 \pm 0.02\,\mathrm{MHz}, \tag{8.15}$$

$$g'_{\mathrm{rm}}/2\pi = 30.32 \pm 0.04\,\mathrm{MHz}, \text{ and} \tag{8.16}$$

$$g'_{\mathrm{qm}}/2\pi = 0.661 \pm 0.038\,\mathrm{MHz}. \tag{8.17}$$

The prime symbol indicates the parameters that were obtained by fitting to the tripartite coupling matrix, in contrast to ones obtained by coupling only two system components.

The fitted values compare well to the ones obtained from the measurements involving only two system components. The zero-current value of the qubit frequency deviates from the one obtained by the power dependent spectroscopy by $\omega_{\mathrm{q}} - \omega'_{\mathrm{q}}\,(I = 0) = 8.7\,\mathrm{kHz}$, which confirms the expected magnetic field dependence. We also recover the coupling strengths with an accuracy within an order of 100 kHz or $\leq 0.5\,\%$. The fit confirms the assumption of an almost negligible direct qubit-magnon coupling, contributing an order of magnitude less, compared to the indirect coupling via the TE_{102} coupling mode.

8.3.2 Input-output fit

We models the full reflection spectrum of the tripartite system by a fit to an analytic model derived using the input-output formalism, see Sec. 4.2. The data processing prior to the fit is analog to the procedure described in Sec. 7.2 for the magnetic linewidth measurements, here including the three tripartite branches. We estimate the field independent background signal from the measurement setup, include it into the fit function and reduce the number of free fit parameters to two, the qubit linewidth κ_q and the magnon linewidth κ_m by using the previously determined component frequencies and resonator linewidths as constant fot parameters at the corresponding magnetic field values. Figure 8.8 shows the reflection amplitude and the corresponding fit plotted against the probe frequencies for the applied current values closest to the two tripartite working points at $I_1^{meas} = 3.91$ A (a) and $I_2^{meas} = 4.92$ A (b), together with the corresponding effective coupling strengths $\tilde{g}_1$ and $\tilde{g}_2$.

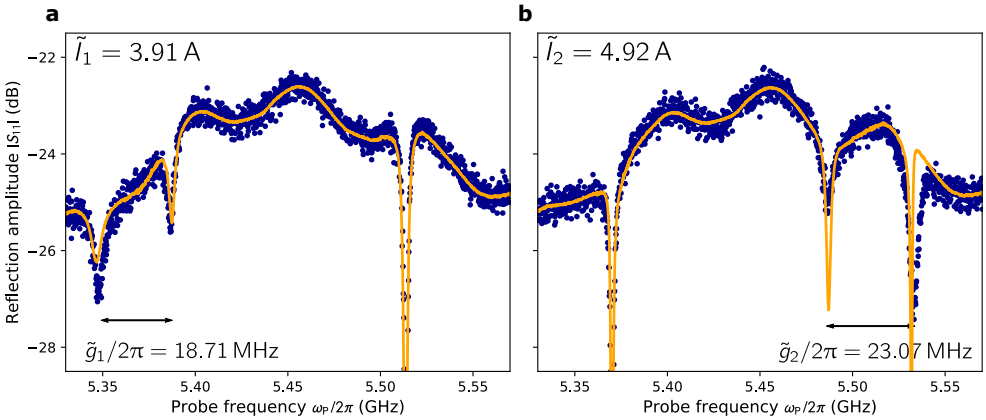

Figure 8.8: Reflection spectrum at the tripartite working points Data and corresponding analytic input-output fit of the amplitude of the reflection spectrum closest to the tripartite working points at $\tilde{I}_1 = 3.91$ A (a) and $\tilde{I}_1 = 4.92$ A (b). The fit qualitatively recovers the three main resonance frequencies, but the resonance line shapes are not reflected most accurately, due to a not precise enough modeling of the background signal. Especially the smallest resonance features are influenced strongest by any inaccuracies in the background estimation. This reduces also the physical meaning of the numerical values representing the optimal fit parameters. Nevertheless, the plots clearly show the anticrossing splitting of the tripartite working points and confirm the strong coupling between the three components.

While we recover the general shape of the spectrum and the three main resonances, there is however a strong deviation of the fit from the data regarding the resonance line shape. While the most pronounced and deepest resonance are represented well by the fit at both currents (for visualization not completely visible in the plots), the

less pronounced resonances are not shaped correctly, failing to represent both the width and the depth of the dips correctly. We attribute this to inaccuracies in the modeling of the background signal, which becomes more crucial at smaller signal strengths. The fit fails to correctly model the only $2-5\,\mathrm{dB}$ signal from the dressed frequencies on top of the background. This is especially well visible at the lowest resonance in Fig. 8.8(a) and the highest resonance in Fig. 8.8(b). While the resonance in the first case is too broad and to shallow compared to the data, with the fit curve rising rising before the data, the fit overestimates the depth of the resonance in the second case, at the $5.53\,\mathrm{GHz}$ resonance in subfigure (b), and the linewidth is modeled much more narrow than in the measurement. At the same time we observe a shoulder feature in the fit that does not match the data, where the background is over estimated compared to the appearing resonance.

Plotting the analytically obtained reflection spectrum color coded, we recover general course of the pronounced resonance features with increasing current, but fitting the data to extract linewidths from the shape of the resonances does not result in reliable data. In order to achieve such a precise fit, there is need for a more elaborate background modeling routine.

8.3.3 Temperature dependent reflection spectra

The weak-excitation approximation of the qubit in the input-output formalism treats the qubit effectively as a two-level system, ignoring all higher non-harmonic energy levels. While we operate the system far away from the temperature equivalent of the participating resonances, the temperature does not necessary reflect the electron temperature or the occupation number of the qubit. In order to visualize the effects of excited higher qubit modes in the reflection spectrum, we simulate spectrum of the tripartite system Hamiltonian with respect to the temperature and compare the features to corresponding measurements.

We simulate the system reflection spectrum using qutip's *qutip.correlation.spectrum* function in an $n = 3$ dimensional Hilbert space for each system component. The function calculates the spectrum of the correlation function

$$S(\omega) = \int_{-\infty}^{\infty} \mathrm{d}\tau \lim_{t\to\infty} \left\langle \hat{A}(t+\tau)\, \hat{B}(t) \right\rangle e^{-\mathrm{i}\omega\tau} \tag{8.18}$$

of the full tripartite system Hamiltonian without the rotating wave approximation,

$$\begin{aligned} \hat{H}_{\mathrm{sys}} = {} & \hat{H}_{\mathrm{r}} + \hat{H}_{\mathrm{m}} + \hat{H}_{\mathrm{q}} + \hbar g_{\mathrm{qr}} \left(\hat{a} + \hat{a}^{\dagger}\right) \left(\hat{\sigma}_{-} + \hat{\sigma}_{+}\right) \\ & + \hbar g_{\mathrm{rm}} \left(\hat{m} + \hat{m}^{\dagger}\right) \left(\hat{a} + \hat{a}^{\dagger}\right) + \hbar g_{\mathrm{qm}} \left(\hat{m} + \hat{m}^{\dagger}\right) \left(\hat{\sigma}_{-} + \hat{\sigma}_{+}\right), \end{aligned} \tag{8.19}$$

with the known coupling strengths and the field dependent frequencies. We construct the qubit Hamiltonian in the charge basis,

$$\hat{H}_{\mathrm{q}} = \sum_n E_{\mathrm{C}} \left(n - \frac{1}{2}\right)^2 |n\rangle \langle n| - \frac{E_{\mathrm{J}}}{2} \left(|n\rangle \langle n+1| + |n+1\rangle \langle n|\right), \tag{8.20}$$

where we calculate the eigenenergies and multiply them with the corresponding excitation number basis. The coupling terms to the magnon and resonator system are calculated individually for the anharmonic qubit levels based on the generalized Jaynes-Cummings Hamiltonian, here stated exemplary for the qubit-resonator coupling,

$$\hat{H}_{\mathrm{qr}} = \sum_{i,j} \hbar g_{ij} |i\rangle \langle j| \left(\hat{a} + \hat{a}^\dagger\right), \tag{8.21}$$

with the coupling energies

$$\hbar g_{ij} \propto \langle i \,|\, \hat{n} \,|\, j \rangle . \tag{8.22}$$

The proportionality factor is based on the fitted coupling strength g_{qr}, describing the coupling to the first qubit transition.

The resonator and magnon Hamiltonians and their coupling are constructed as in Eq. 2.38, with the corresponding creator and annihilator operators and the fitted coupling strength. We add dissipation to the system by defining collapse operators that are introduced in the Lindblad equation

$$\frac{\mathrm{d}}{\mathrm{d}t}\hat{\rho}(t) = -\frac{\mathrm{i}}{\hbar}\left[\hat{H}_{\mathrm{sys}}, \hat{\rho}(t)\right] + \sum_n \left(\hat{C}_n \hat{\rho}(t) \hat{C}_n^\dagger - \frac{1}{2}\left\{\hat{C}_n^\dagger \hat{C}_n, \hat{\rho}(t)\right\}\right), \tag{8.23}$$

where the collapse operators $\hat{C}_j = \sqrt{\kappa_j}\hat{A}_j$ describe the operator $\hat{A}_j$ through which the system couples to the environment with the coupling rate κ_j. The interaction enables both the decay and the creation of excitation. We consider excitation creation and annihilation in the resonator and the magnon due to coupling to a bath and internal losses. The collapse operators of the qubit models the energy relaxation and thermal population at a $1/T_1$ rate combined with an addition dephasing rate. The environment temperature is accounted for by attributing a thermal occupation number $n_i^{\mathrm{th}} = \exp\left(-\hbar\omega_i / k_{\mathrm{B}} T\right)$ based on the Boltzmann distribution to the individual components. It is included as an additional term in the annihilator operators and as a proportionality factor in the collapse operators describing an excitation. Exemplary, we find for the collapse operators of the photon states in the resonator

$$\hat{C}_{r1} = \sqrt{\kappa_{\mathrm{r}}\left(1 + n_r^{\mathrm{th}}\right)}\hat{a} \tag{8.24}$$

$$\hat{C}_{r2} = \sqrt{\kappa_{\mathrm{r}} n_r^{\mathrm{th}}}\hat{a}^\dagger. \tag{8.25}$$

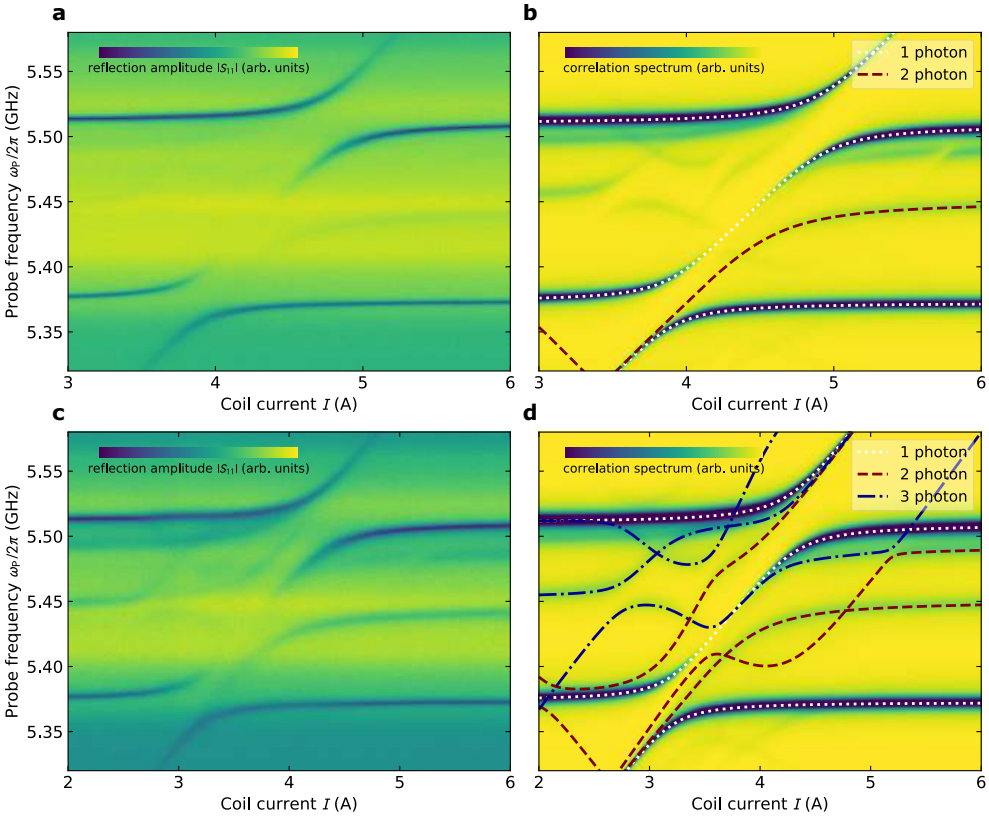

Figure 8.9: Tripartite reflection spectrum and simulation (I) (b) The $T = 25\,\mathrm{mK}$ simulation shows a rich spectrum of thermally excited modes besides the fundamental one photon modes described by the analytic input-output formula. The corresponding data (a) shows the fundamental mode and an additional two photon mode going to higher currents. (d) The simulation at 100 mK shows a thermal broadening of all modes. (c) The data shows more two photon transitions that are also more pronounced and broadened. The first hints of three photon transitions are visible as well. The energy eigenvalues of all modes that are visible in the data are indicated in the simulation plots, with colors indicating the number of photons participating in the transition. The color gradient of the simulated correlation spectra is adjusted to visualize all possible transitions best.

We measure the reflection spectrum of the tripartite system with parameters similar to the ones described in Sec. 8.3.1 for temperatures up to 500 mK, to study the influence of the thermal environment on the system and compare the data with the corresponding simulated spectra. In order to have a similar color, we plot the negative correlation spectrum to the data. This maps the high correlation to the resonance dips in the data.

Figure 8.9 shows a side-by-side comparison of the measured reflection spectrum on the left hand side, subplots (a) at $T = 25\,\mathrm{mK}$ and (c) at $T = 100\,\mathrm{mK}$, with their corresponding simulation on the right hand side in subplots (b) and (d). We increase the visibility of the data, by highlighting the eigenenergies of the modes appearing in the measurements as dashed colored lines in the simulation.

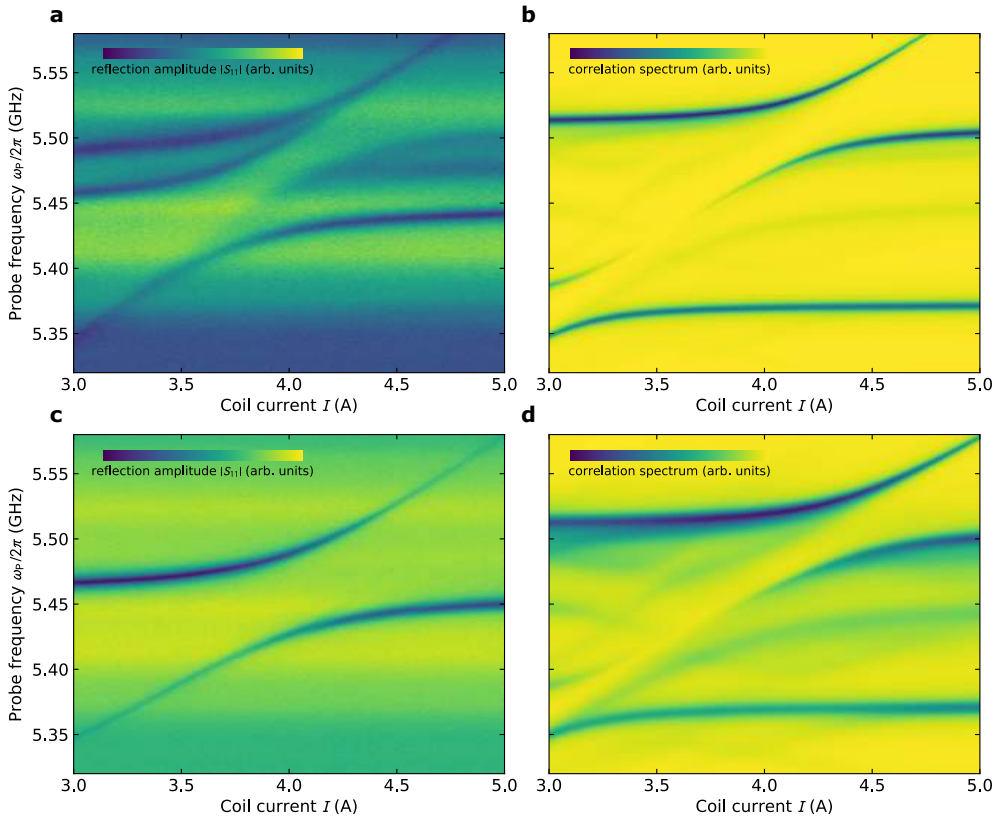

Figure 8.10: Tripartite reflection spectrum and simulation at (II) At $T = 250\,\mathrm{mK}$, the measured spectrum (a) shows already a decoupling of the qubit from the system, where several mixed modes are visible. We observe the magnon-polariton at $T = 500\,\mathrm{mK}$, without qubit influence (b). In contrast to these measurements, the corresponding simulations still show a qubit influence and the tripartite spectra is visible, but thermally smeared out, (b) and (d).

At $T = 25\,\mathrm{mK}$, the simulation shows a rich mode spectrum in addition to the low frequency tripartite modes, which are indicated as white dashed lines in the simulation data. Several other magnon frequency dependent modes, which correspond to multi photon transitions, are visible in the simulation and we are able to identify one of these transitions in the measured spectrum. At high currents, we

find a small resonance at around 5.45 GHz, which for lower currents shifts to lower frequencies. This mode corresponds to a two photon excitation in the system and is indicated as a red dashed line in the simulation plot. Increasing the temperature to 100 mK, comparing the subplots in the lower row, the resonances in both the measured and simulated spectrum broaden and become more pronounced due to the increased interaction with the environment and thermal population of higher modes. Many of the simulated modes are visible in the measured spectrum. Besides the mode seen at 25 mK, other two photon modes (red dashed lines) and the onset of some three photon modes (blue dashed lines) are visible in the measured data and indicated in the simulation plot.

Increasing the temperature further, the qubit-resonator coupling breaks down similar to Fig. 8.6(a) and the spectrum transforms into the known magnon-polariton spectrum without qubit participation at $T = 500$ mK, see Fig. 8.10(c), with a transition regime at $T = 250$ mK shown in Fig. 8.10(a). The qubit is not yet decoupled in the simulations, the smeared out modes of the tripartite spectra are still visible at higher temperatures, see Figs. 8.10(b) and (d).

The qutip simulations are able to reproduce the measurements in the temperature regime, where the qubit is not thermally saturated quite well. We are able to reproduce the observed broadening of the linewidths due to the increased coupling to the environment and the simulations allow us to identify the observed multi-photon transitions at higher environment temperatures.

8.4 Towards Rabi oscillation in the strongly coupled tripartite system

Coherent energy exchange, which was shown by the strong coupling at the tripartite working points, between the system components is necessary for application in quantum information processing. In time domain measurements, this manifests as Rabi oscillation between the system components. Similar to the pure qubit characterization in Sec. 8.4, we analyze the system by applying pulsed microwave excitation and monitor the time dynamics to obtain excitation and coherence lifetimes. First, we characterize the strongly qubit-resonator system with the magnon frequency far detuned at zero applied current. Afterwards we ramp the magnetic field to the first tripartite working point and perform current dependent Rabi oscillation measurements.

Rabi oscillations are measured by applying microwave pulses at various lengths with the previously determined qubit frequency to the system and measure the qubit

state. The pulse rotates the Bloch vector between the ground and excited state and plotting the qubit inversion against the pulse length shows the continuous change in qubit state with an exponential excitation decay. By fitting a damped sine function we obtain the length of the π pulse, T_π, that rotates the qubit state by 180°. The measured data together with the fit and the pulse scheme is shown in Fig. 8.11(a) and we obtain $T_\pi^{\mathrm{qr}} = 27.14\,\mathrm{ns}$ for the strongly coupled qubit-resonator system.

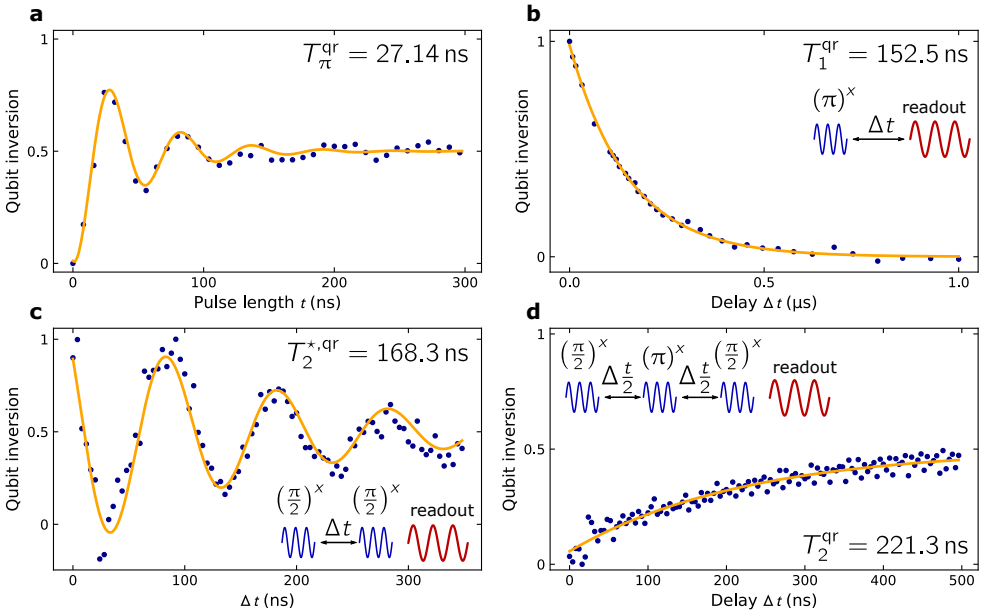

Figure 8.11: Dissipative dynamics of the qubit-resonator mode (a) Driving the qubit transition frequency for varying pulse lengths t rotates the qubit Bloch vector on the sphere between the ground and excited state. Exciting the qubit takes a time $T_\pi^{\mathrm{qr}} = 27.14\,\mathrm{ns}$. (b) Measuring the qubit state after excitation and subsequent time delays results in an energy relaxation time $T_1^{\mathrm{qr}} = 152.5\,\mathrm{ns}$. Decoherence measurements in the Ramsey sequence (b) and with an additional Hahn echo pulse (c) result in qubit coherence lifetimes $T_2^{\star,\mathrm{qr}} = 168.3\,\mathrm{ns}$ and $T_2^{\mathrm{qr}} = 221.3\,\mathrm{ns}$, respectively. No current was applied during these measurements.

We measure an energy relaxation time $T_1^{\mathrm{qr}} = 152.5\,\mathrm{ns}$ and a decoherence time by a Ramsey pulse sequence $T_{2i}^{\star,\mathrm{qr}} = 168.3\,\mathrm{ns}$, see Figs. 8.11(b) and (c). The corresponding pulse sequence is sketched in the corresponding plots and described in more detail in Sec. 8.4. Additionally we perform a Ramsey type measurement with an additional Hahn echo pulse [201], a π pulse that refocuses the dephased qubit state, after half the delay time. We measure an spin echo decoherence time $T_2^{\mathrm{qr}} = 221.3\,\mathrm{ns}$, see Fig. 8.11(d). All measured lifetimes are listed in table 8.3.

Comparing theses lifetimes to the transmon lifetimes in the dispersive limit we find the time of the π pulse a factor 5.9 smaller in the strongly coupled case. The smaller detuning between qubit and resonator allows for a faster energy transfer from the microwave feed line to the qubit through the resonator bandpass. The T_1 time and the $T_2^\star$ time are smaller by a factor of 2.6 and 3.1, respectively, which we attribute to an increased loss out of the resonator.

In order to observe coherent excitation exchange between in the tripartite system, we sweep the current up to the first tripartite working point and perform Rabi oscillation measurements, shown in Fig. 8.12. Figure 8.12(a) shows the color coded qubit inversion with respect to the applied pulse length and the coil current. The individual Rabi oscillation measurements at the two current values marked by white dashed lines at 3.45 A and 4.07 A, with the latter corresponding to the current value of the first tripartite point are show in subplot (b). The current value of the first tripartite point is slightly different compared to the one in Sec. 8.3.3, since these experiments were performed in a separate measurement run.

The qubit inversion shows a decreasing pulse length for the first qubit inversion maximum with increasing current but the overall signal strength decreases, as seen by the data colored all in blue. While we still measure Rabi oscillations with a maximum qubit inversion of 75.6 % at 3.45 A, the signal strength decreases with higher current and the Rabi oscillation vanishes completely at the tripartite point.

Table 8.3: Dissipation parameters of the strongly coupled qubit-resonator system The table includes the duration of the π pulse T_π^{qr}, the energy relaxation time T_1^{qr}, and the decoherence times obtained by a Ramsey measurement with and without an additional Hahn echo pulse T_2^{qr} and $T_2^{\star,\mathrm{qr}}$, respectively. No current was applied to the coil at these measurements.

T_π^{qr} (ns)	T_1^{qr} (ns)	T_2^{qr} (ns)	$T_2^{\star,\mathrm{qr}}$ (ns)
27.14	152.5	168.3	221.3

We are able to implement nonlinear hybrid systems using magnon excitation. In the dispersive regime we observe indirect qubit-magnon coupling and observe the square root dependence of the coupling strength on the number of participating spins. While the effective coupling places the system in the strong coupling regime, the signal to noise ratio is too low to observe the hybridized mode dips in the spectrum. We increase the coupling by reducing the detuning in the strongly coupled tripartite system, where we observe and fit the three dressed modes. Thermal excitation of higher system transition are observed and simulated as well. Although

the system shows strong coupling in the spectroscopic measurements, we do not observe Rabi oscillation in the system approaching the first tripartite working point.

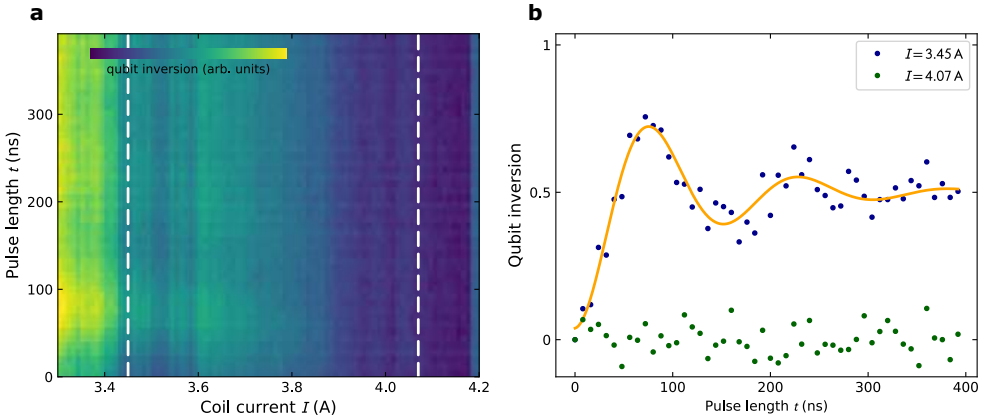

Figure 8.12: Current dependent Rabi oscillations (a) Color coded qubit inversion obtained by Rabi oscillation measurements with respect to the applied coil current. The maximum qubit inversion shifts to lower pulse lengths with increasing coil current, but the overall oscillation signal decreases and vanishes approaching the first tripartite working point. The color gradient is adjusted for better visibility. (b) Individual Rabi oscillation measurements for $I = 3.45\,\mathrm{A}$ (blue) and $I = 4.07\,\mathrm{A}$ (green), that highlight the decreasing Rabi oscillation signal. Both currents are also indicated as dashed lines in the color plot. The applied currents do not coincide with the current axes in Sec. 8.3 since the time domain measurements were measured in a different measurement cool down with a slightly changed current-to-field relationship.

9 Conclusion

The goal of this thesis was to investigate magnetic excitation in quantum circuits, with the goal to explore the potential of magnon based technology for applications in quantum computing and quantum information processing. We embedded magnons in a linear and nonlinear quantum hybrid system in different coupling regimes and studied the microwave properties of the magnetic resonance at millikelvin temperatures and single photon excitation powers. The presented experiments demonstrate the dominant loss mechanism of magnon excitation at the working environment for superconducting quantum circuits and the first measurements on a strongly coupled light-matter-spin tripartite system.

In the first part of the this thesis we designed a harmonic photon-magnon hybrid system still in the regime of classical physics. We strongly coupled the Kittel mode magnons in a ferrimagnetic YIG sphere to cavity resonance photons, creating a cavity magnon polarion quasiparticle with a coupling strength $g = 10.39\,\mathrm{MHz}$. We extracted the internal magnon resonance linewidth from the microwave reflection spectrum and identified the limiting loss mechanism in different temperature regimes, with special focus on the millikelvin temperature regime in a dilution refrigerator. Together with our collaborators at JGU Mainz, we confirmed scattering on rare-earth impurities in the YIG and multi-magnon scattering on the sample surface as the dominant loss mechanism when cooling the system from room temperature down to single digit kelvin temperatures [76]. Cooling further to millikelvin temperatures, the magnetic resonance linewidth is limited by excitation losses into two-level system, a characteristic loss model observed in glasses and superconducting circuits as well. We confirmed the temperature trend of the linewidth following a hyperbolic tangent and observed the power dependence of the linewidth following a $1/\sqrt{P}$ trend from single photon to the 10^7 exchtation regime, which is attributed to incoherent losses to a bath of two-level systems as the main loss mchanism. With our measurements we expanded the study of cavity magnon polaritons to off-resonant measurements, where we were able to extract the magnon excitation percentages in the cavity magnon polariton. With the number of excited magnons depending on the frequency detuning between magnon and photon at constant experimental input power, the observed magnon linewidth trend resembled the power dependent measurements [62].

Having demonstrated the strong magnon-cavity coupling and usability at low temperatures, we fabricated a superconducting 3D transmon qubit as a nonlinear element for our quantum circuit. This allowed us to address single magnon excitations, in contrast to the Boltzmann-distributed excitations of the magnon-photon system. We demonstrated the quantum properties of the qubit by Rabi oscillations and measured quantum excitation lifetimes on the order of 500 ns. With the system in the dispersive limit, the magnon frequency is tuned towards the qubit and magnon-vacuum induced Rabi oscillations as an anticrossing in dispersive shift measurements were observed. The Qubit and the magnon coupled via virtual photon exchange of the surrounding cavity modes with an effective coupling strength of 3.3 MHz, which did not put the system in the strong coupling regime. Measurements on an improved system with a larger coupling of 9.34 MHz due to a larger number of participating spins showed a signal to noise ratio not strong enough for further investigations.

As a next step, we built a quantum hybrid system that coupled light, matter, and spin excitation to increase the effective coupling strength and eliminated the need for dispersive shift measurements. This allowed us to measure the system directly via microwave spectroscopy. We aimed at the cavity resonance modes to be degenerate with the qubit transition, reaching a detuning of 25 MHz compared to a 67.6 MHz coupling strength. Tuning the Kittel mode frequency through the already dressed states revealed two tripartite working points with strong effective coupling on the order of 20 MHz between the components. We were able to fit the reflection spectrum with the input-output formalism and simulated the spectrum of the full system Hamiltonian, which allowed us to identify multi-photon transitions. Temperature sweeps and corresponding simulation showed thermal excitation and subsequent transitions containing up to three photons, before the qubit functionality broke down due to thermal effects.

In the final experimental section we investigated the dissipative dynamics of the tripartite system, looking for Rabi oscillation between the system components. Without magnon contribution, we observed relaxation and coherence times about a factor of 3 smaller than for the bare qubit in the dispersive regime. Increasing the Kittel mode frequency however, the Rabi oscillation frequency decreased slightly before the signal vanished completely towards the tripartite point.

In conclusion, we identified the dominant magnon loss mechanism at low temperatures and presented coherent exchange between a superconducting qubit and a Kittel mode magnon in the dispersive regime, as well as proof-of-principle measurements on a strongly coupled tripartite system, a nonlinear quantum circuit containing magnons.

The presented experiments are a promising foundation for more sophisticated measurements, for which the system could benefit from modification or redesign of individual components.

Outlook

During the course of this thesis, a study showing the first application of a quantum magnonic system besides a proof-of-concept experiment was published, where the number of excited magnons was expicitly counted [67]. This experiment is based on coupled qubit-photon systems measured more than 10 years ago [169, 170] and shows one roadmap for quantum magnonics, realizing features previously measured with photons using magnon excitation, with possible next candidates being the magnon equivalent of coherent superposition states [171] and Schrödinger cat states [172]. A recent preprint follows this path in creating the single-photon detector counterpart for a magnonic system [68].

Time resolved measurements regarding Rabi oscillation or direct measurements of magnon lifetimes, besides an estimation based on a resonance linewidth are yet to be shown. This would open up the door towards quantum storage experiments, where a quantum state is swapped to the magnon and back to the qubit to be read out again. Quantum gates via parametric coupling or fast qubit detuning via as Stark shifts are already available in the toolbox for superconducting circuits and the measurement protocol can be shortened by single shot qubit readout with active reset. Experimentally further away are quantum transport measurement, where a quantum excitation is encoded in $k \neq 0$ magnons that propagate through the sample to be picked up by a second qubit.

Looking at our current measurement setup regarding the next experimental generation, there is room for improvement on all three system components. A manual polishing treatment of the YIG surface may reduce the impact of TLS losses and create a sharper magnon resonance linewidth with increased excitation lifetimes. Conference presentation and comments by members of the Tang lab at Yale University suggest a much improved resonance linewidth after a manual ultra-fine polishing of the sample surface, compared to the values obtained with the initial surface treatment by the supplier. The cavity resonator design can be improved regarding coupling strength of to the Kittel mode, where a coupling in the range of 50 MHz would be advantageous. Fabricating the cavity out of aluminium instead of copper may improve the Q factors, despite the superconductivity breaking down in some parts due to the applied magnetic field. At last, an improved qubit fabrication leads to longer coherence times which increase the overall experimental possibilities.

With these possibilities and already available approaches to solve similar problems we are convinced that magnons can play a role as a building block in future quantum circuits.

Bibliography

[1] R. P. Feynman: *Simulating physics with computers*. International Journal of Theoretical Physics **21**.6 (1982), pp. 467–488. DOI: 10.1007/BF02650179.

[2] I. Georgescu: *Nobel Prize 2012: Haroche & Wineland*. Nature Physics **8**.11 (2012), p. 777. DOI: 10.1038/nphys2472.

[3] R. Babbush, J. McClean, D. Wecker, A. Aspuru-Guzik, and N. Wiebe: *Chemical basis of Trotter-Suzuki errors in quantum chemistry simulation*. Physical Review A **91** (2015), p. 022311. DOI: 10.1103/PhysRevA.91.022311.

[4] D. J. Bernstein and T. Lange: *Post-quantum cryptography*. Nature **549** (2017), 188 EP -. DOI: 10.1038/nature23461.

[5] A. Acin, I. Bloch, H. Buhrman, T. Calarco, C. Eichler, J. Eisert, D. Esteve, N. Gisin, S. J. Glaser, F. Jelezko, S. Kuhr, M. Lewenstein, F. F. Riedel, P. O. Schmidt, R. Thew, A. Wallraff, I. Walmsley, and F. K. Wilhelm: *The quantum technologies roadmap: a European community view*. New Journal of Physics **20**.8 (2018), p. 080201. DOI: 10.1088/1367-2630/aad1ea.

[6] S. Boixo, S. V. Isakov, V. N. Smelyanskiy, R. Babbush, N. Ding, Z. Jiang, M. J. Bremner, J. M. Martinis, and H. Neven: *Characterizing quantum supremacy in near-term devices*. Nature Physics **14**.6 (2018), pp. 595–600. DOI: 10.1038/s41567-018-0124-x.

[7] A. Kandala, A. Mezzacapo, K. Temme, M. Takita, M. Brink, J. M. Chow, and J. M. Gambetta: *Hardware-efficient variational quantum eigensolver for small molecules and quantum magnets*. Nature **549** (2017), 242 EP -. DOI: 10.1038/nature23879.

[8] N. Moll, P. Barkoutsos, L. S. Bishop, J. M. Chow, A. Cross, D. J. Egger, S. Filipp, A. Fuhrer, J. M. Gambetta, M. Ganzhorn, A. Kandala, A. Mezzacapo, P. Müller, W. Riess, G. Salis, J. Smolin, I. Tavernelli, and K. Temme: *Quantum optimization using variational algorithms on near-term quantum devices*. Quantum Science and Technology **3**.3 (2018), p. 030503. DOI: 10.1088/2058-9565/aab822.

[9] H. Zhang, C.-X. Liu, S. Gazibegovic, D. Xu, J. A. Logan, G. Wang, N. van Loo, J. D. S. Bommer, M. W. A. de Moor, D. Car, R. L. M. Op het Veld, P. J. van Veldhoven, S. Koelling, M. A. Verheijen, M. Pendharkar, D. J. Pennachio, B. Shojaei, J. S. Lee, C. J. Palmstrøm, E. P. A. M. Bakkers, S. D. Sarma, and L. P. Kouwenhoven: *Quantized Majorana conductance*. Nature **556** (2018), 74 EP -. DOI: 10.1038/nature26142.

[10] M. H. Devoret and R. J. Schoelkopf: *Superconducting Circuits for Quantum Information: An Outlook*. Science **339**.6124 (2013), pp. 1169–1174. DOI: 10.1126/science.1231930.

[11] I. M. Georgescu, S. Ashhab, and Franco Nori: *Quantum simulation*. Reviews of Modern Physics **86** (2014), pp. 153–185. DOI: 10.1103/RevModPhys.86.153.

[12] F. Arute, K. Arya, R. Babbush, D. Bacon, J. C. Bardin, R. Barends, R. Biswas, S. Boixo, F. G. S. L. Brandao, D. A. Buell, B. Burkett, Y. Chen, Z. Chen, B. Chiaro, R. Collins, W. Courtney, A. Dunsworth, E. Farhi, B. Foxen, A. Fowler, C. Gidney, M. Giustina, R. Graff, K. Guerin, S. Habegger, M. P. Harrigan, M. J. Hartmann, A. Ho, M. Hoffmann, T. Huang, T. S. Humble, S. V. Isakov, E. Jeffrey, Z. Jiang, D. Kafri, K. Kechedzhi, J. Kelly, P. V. Klimov, S. Knysh, A. Korotkov, F. Kostritsa, D. Landhuis, M. Lindmark, E. Lucero, D. Lyakh, S. Mandrà, J. R. McClean, M. McEwen, A. Megrant, X. Mi, K. Michielsen, M. Mohseni, J. Mutus, O. Naaman, M. Neeley, C. Neill, M. Y. Niu, E. Ostby, A. Petukhov, J. C. Platt, C. Quintana, E. G. Rieffel, P. Roushan, N. C. Rubin, D. Sank, K. J. Satzinger, V. Smelyanskiy, K. J. Sung, M. D. Trevithick, A. Vainsencher, B. Villalonga, T. White, Z. J. Yao, P. Yeh, A. Zalcman, H. Neven, and J. M. Martinis: *Quantum supremacy using a programmable superconducting processor*. Nature **574** (2019), pp. 505–510. DOI: 10.1038/s41586-019-1666-5.

[13] W. D. Oliver: *Quantum computing takes flight*. Nature **574** (2019), pp. 487–488. DOI: 10.1038/d41586-019-03173-4.

[14] Y. Nakamura, Yu. A. Pashkin, and J. S. Tsai: *Coherent control of macroscopic quantum states in a single-Cooper-pair box*. Nature **398**.6730 (1999), pp. 786–788. DOI: 10.1038/19718.

[15] C. Neill, P. Roushan, K. Kechedzhi, S. Boixo, S. V. Isakov, V. Smelyanskiy, A. Megrant, B. Chiaro, A. Dunsworth, K. Arya, R. Barends, B. Burkett, Y. Chen, Z. Chen, A. Fowler, B. Foxen, M. Giustina, R. Graff, E. Jeffrey, T. Huang, J. Kelly, P. Klimov, E. Lucero, J. Mutus, M. Neeley, C. Quintana, D. Sank, A. Vainsencher, J. Wenner, T. C. White, H. Neven, and J. M. Martinis: *A blueprint for demonstrating quantum supremacy with superconducting qubits*. Science **360**.6385 (2018), pp. 195–199. DOI: 10.1126/science.aao4309.

[16] A. Wallraff, D. I. Schuster, A. Blais, L. Frunzio, R.-S. Huang, J. Majer, S. Kumar, S. M. Girvin, and R. J. Schoelkopf: *Strong coupling of a single photon to a superconducting qubit using circuit quantum electrodynamics*. Nature **431**.7005 (2004), pp. 162–167. DOI: 10.1038/nature02851.

[17] A. Blais, R.-S. Huang, A. Wallraff, S. M. Girvin, and R. J. Schoelkopf: *Cavity quantum electrodynamics for superconducting electrical circuits: An architecture for quantum computation*. Physical Review A **69** (2004), p. 062320. DOI: 10.1103/PhysRevA.69.062320.

[18] P. V. Klimov, J. Kelly, Z. Chen, M. Neeley, A. Megrant, B. Burkett, R. Barends, K. Arya, B. Chiaro, Yu Chen, A. Dunsworth, A. Fowler, B. Foxen, C. Gidney, M. Giustina, R. Graff, T. Huang, E. Jeffrey, Erik Lucero, J. Y. Mutus, O. Naaman, C. Neill, C. Quintana, P. Roushan, Daniel Sank, A. Vainsencher, J. Wenner, T. C. White, S. Boixo, R. Babbush, V. N. Smelyanskiy, H. Neven, and J. M. Martinis: *Fluctuations of Energy-Relaxation Times in Superconducting Qubits*. Physical Review Letters **121** (2018), p. 090502. DOI: 10.1103/PhysRevLett.121.090502.

[19] J. J. Burnett, A. Bengtsson, M. Scigliuzzo, D. Niepce, M. Kudra, P. Delsing, and J. Bylander: *Decoherence benchmarking of superconducting qubits*. npj Quantum Information **5**.1 (2019), p. 54. DOI: 10.1038/s41534-019-0168-5.

[20] S. Schlör, J. Lisenfeld, C. Müller, A. Bilmes, A. Schneider, D. P. Pappas, A. V. Ustinov, and M. Weides: *Correlating Decoherence in tTansmon Qubits: Low Frequency Noise by Single Fluctuators*. Physical Review Letters **123** (2019), p. 190502. DOI: 10.1038/s41534-019-0168-5.

[21] A. G. Fowler, M. Mariantoni, J. M. Martinis, and A. N. Cleland: *Surface codes: Towards practical large-scale quantum computation*. Physical Review A **86** (2012), p. 032324. DOI: 10.1103/PhysRevA.86.032324.

[22] Z.-L. Xiang, S. Ashhab, J. Q. You, and F. Nori: *Hybrid quantum circuits: Superconducting circuits interacting with other quantum systems*. Reviews of Modern Physics **85** (2013), pp. 623–653. DOI: 10.1103/RevModPhys.85.623.

[23] R. Schirhagl, K. Chang, M. Loretz, and C. L. Degen: *Nitrogen-Vacancy Centers in Diamond: Nanoscale Sensors for Physics and Biology*. Annual Review of Physical Chemistry **65**.1 (2014), pp. 83–105. DOI: 10.1146/annurev-physchem-040513-103659.

[24] A. Tchebotareva, S. L. N. Hermans, P. C. Humphreys, D. Voigt, P. J. Harmsma, L. K. Cheng, D. L. Verlaan, N. Dijkhuizen, W. de Jong, A. Dréau, and R. Hanson: *Entanglement between a Diamond Spin Qubit and a Photonic Time-Bin Qubit at Telecom Wavelength*. Physical Review Letters **123** (2019), p. 063601. DOI: 10.1103/PhysRevLett.123.063601.

[25] S. Wehner, D. Elkouss, and R. Hanson: *Quantum internet: A vision for the road ahead*. **362**.6412 (2018), eaam9288. DOI: 10.1126/science.aam9288.

[26] P. C. Maurer, G. Kucsko, C. Latta, L. Jiang, N. Y. Yao, S. D. Bennett, F. Pastawski, D. Hunger, N. Chisholm, M. Markham, D. J. Twitchen, J. I. Cirac, and M. D. Lukin: *Room-Temperature Quantum Bit Memory Exceeding One Second*. Science **336**.6086 (2012), pp. 1283–1286. DOI: 10.1126/science.1220513.

[27] J. Braumüller, M. Marthaler, A. Schneider, A. Stehli, H. Rotzinger, M. Weides, and A. V. Ustinov: *Analog quantum simulation of the Rabi model in the ultra-strong coupling regime*. Nature Communications **8**.1 (2017), p. 779. DOI: 10.1038/s41467-017-00894-w.

[28] V. Giovannetti, S. Lloyd, and L. Maccone: *Advances in quantum metrology*. Nature Photonics **5**.4 (2011), pp. 222–229. DOI: 10.1038/nphoton.2011.35.

[29] C. L. Degen, F. Reinhard, and P. Cappellaro: *Quantum sensing*. Review of Modern Physisc **89** (2017), p. 035002. DOI: 10.1103/RevModPhys.89.035002.

[30] A. R. Shlyakhov, V. V. Zemlyanov, M. V. Suslov, A. V. Lebedev, G. S. Paraoanu, G. B. Lesovik, and G. Blatter: *Quantum metrology with a transmon qutrit*. Physical Review A **97** (2018), p. 022115. DOI: 10.1103/PhysRevA.97.022115.

[31] S. Danilin, A. V. Lebedev, A. Vepsäläinen, G. B. Lesovik, G. Blatter, and G. S. Paraoanu: *Quantum-enhanced magnetometry by phase estimation algorithms with a single artificial atom*. npj Quantum Information **4**.1 (2018), p. 29. DOI: 10.1038/s41534-018-0078-y.

[32] Y. Kubo, F. R. Ong, P. Bertet, D. Vion, V. Jacques, D. Zheng, A. Dréau, J.-F. Roch, A. Auffeves, F. Jelezko, J. Wrachtrup, M. F. Barthe, P. Bergonzo, and D. Esteve: *Strong Coupling of a Spin Ensemble to a Superconducting Resonator*. Physical Review Letters **105** (2010), p. 140502. DOI: 10.1103/PhysRevLett.105.140502.

[33] S. Probst, H. Rotzinger, S. Wünsch, P. Jung, M. Jerger, M. Siegel, A. V. Ustinov, and P. A. Bushev: *Anisotropic Rare-Earth Spin Ensemble Strongly Coupled to a Superconducting Resonator*. Physical Review Letters **110** (2013). DOI: 10.1103/PhysRevLett.110.157001.

[34] S. Probst, A. Tkalčec, H. Rotzinger, D. Rieger, J-M. Le Floch, M. Goryachev, M. E. Tobar, A. V. Ustinov, and P. A. Bushev: *Three-dimensional cavity quantum electrodynamics with a rare-earth spin ensemble*. Physical Review B **90** (2014), p. 100404. DOI: 10.1103/PhysRevB.90.100404.

[35] S. Probst, N. Kukharchyk, H. Rotzinger, A. Tkalčec, S. Wünsch, A. D. Wieck, M. Siegel, A. V. Ustinov, and P. A. Bushev: *Hybrid quantum circuit with implanted erbium ions*. Applied Physics Letters **105**.16 (2014), p. 162404. DOI: 10.1063/1.4898696.

[36] N. Bohr: *Studier over Metallernes Elektrontheori*. PhD thesis. University of Copenhagen, 2014.

[37] J. H. Van Leeuwen: *Quantum limits on noise in linear amplifiers*. Le Journal de Physique et le Radium **2**.26 (1921), pp. 361–377. DOI: 10.1051/jphysrad:01921002012036100.

[38] A. I. Akhiezer, V. G. Bar'yakhtar, and M. I. Kaganov: *Spin Waves in Ferromagnets and Antiferromagnets. I*. Soviet Physics Uspekhi **3**.4 (1961), pp. 567–592. DOI: 10.1070/pu1961v003n04abeh003309.

[39] A. I. Akhiezer, V. G. Bar'yakhtar, and M. I. Kaganov: *Spin Waves in Ferromagnets and Antiferromagnets. I Interactin of Spin Waves with on another and with Lattice Vibrations, Relaxation and Kinetic Processes*. Soviet Physics Uspekhi **3**.5 (1961), pp. 661–676. DOI: 10.1070/pu1961v003n05abeh003318.

[40] T. Holstein and H. Primakoff: *Field Dependence of the Intrinsic Domain Magnetization of a Ferromagnet*. Physical Review **58** (1940), pp. 1098–1113. DOI: 10.1103/PhysRev.58.1098.

[41] F. J. Dyson: *General Theory of Spin-Wave Interactions*. Physical Review **102** (1956), pp. 1217–1230. DOI: 10.1103/PhysRev.102.1217.

[42] J. H. E. Griffiths: *Anomalous High-frequency Resistance of Ferromagnetic Metals*. Nature **158**.4019 (1946), pp. 670–671. DOI: 10.1038/158670a0.

[43] P. A. Fleury, S. P. S. Porto, L. E. Cheesman, and H. J. Guggenheim: *Light Scattering by Spin Waves in FeF_2*. Physical Review Letters **17** (1966), pp. 84–87. DOI: 10.1103/PhysRevLett.17.84.

[44] S. O. Demokritov, V. E. Demidov, O. Dzyapko, G. A. Melkov, A. A. Serga, B. Hillebrands, and A. N. Slavin: *Bose–Einstein condensation of quasi-equilibrium magnons at room temperature under pumping*. Nature **443** (2006), pp. 430–433. DOI: 10.1038/nature05117.

[45] V. V. Kruglyak, S. O. Demokritov, and D. Grundler: *Magnonics*. Journal of Physics D: Applied Physics **43**.26 (2010), p. 264001. DOI: 10.1088/0022-3727/43/26/264001.

[46] B. Lenk, H. Ulrichs, F. Garbs, and M. Münzenberg: *The building blocks of magnonics*. Physics Reports **507**.4 (2011), pp. 107–136. DOI: https://doi.org/10.1016/j.physrep.2011.06.003.

[47] A. Imamoğlu: *Cavity QED Based on Collective Magnetic Dipole Coupling: Spin Ensembles as Hybrid Two-Level Systems*. Physical Review Letters **102** (2009). DOI: 10.1103/physRevLett.102.083602.

[48] Ö. O. Soykal and M. E. Flatté: *Size dependence of strong coupling between nanomagnets and photonic cavities*. Physical Review B **82** (2010), p. 104413. DOI: 10.1103/PhysRevB.82.104413.

[49] Ö. O. Soykal and M. E. Flatté: *Strong Field Interactions between a Nanomagnet and a Photonic Cavity*. Physical Review Letters **104** (2010), p. 077202. DOI: 10.1103/PhysRevLett.104.077202.

[50] H. Huebl, C. W. Zollitsch, J. Lotze, F. Hocke, M. Greifenstein, A. Marx, R. Gross, and S. T. B. Goennenwein: *High Cooperativity in Coupled Microwave Resonator Ferrimagnetic Insulator Hybrids*. Physical Review Letters **111** (2013), p. 127003. DOI: 10.1103/PhysRevLett.111.127003.

[51] M. Harder and C.-M. Hu: "Cavity Spintronics: An Early Review of Recent Progress in the Study of Magnon-Photon Level Repulsion". Ed. by Robert E. Camley and Robert L. Stamps. Vol. 69. Solid State Physics. 2018, pp. 47–121. DOI: 10.1016/bs.ssp.2018.08.001.

[52] C.-M. Hu: *Dawn of Cavity Spintronics*. Physics in Canada **72**.2 (2016).

[53] X. Zhang, C.-L. Zou, L. Jiang, and H. X. Tang: *Strongly Coupled Magnons and Cavity Microwave Photons*. Physical Review Letters **113** (2014), p. 156401. DOI: 10.1103/PhysRevLett.113.156401.

[54] M. Goryachev, W. G. Farr, D. L. Creedon, Y. Fan, M. Kostylev, and M. E. Tobar: *High-Cooperativity Cavity QED with Magnons at Microwave Frequencies*. Physical Review Applied **2** (2014), p. 054002. DOI: 10.1103/PhysRevApplied.2.054002.

[55] M. Harder, L.-H. Bai, C. Match, J. Sirker, and C.-M. Hu: *Study of the cavity-magnon-polariton transmission line shape*. Science China Physics, Mechanics & Astronomy **59**.11 (2016), p. 117511. DOI: 10.1007/s11433-016-0228-6.

[56] A. Osada, R. Hisatomi, A. Noguchi, Y. Tabuchi, R. Yamazaki, K. Usami, M. Sadgrove, R. Yalla, M. Nomura, and Y. Nakamura: *Cavity Optomagnonics with Spin-Orbit Coupled Photons*. Physical Review Letters **116** (2016), p. 223601. DOI: 10.1103/PhysRevLett.116.223601.

[57] X. Zhang, C.-L. Zou, L. Jiang, and H. X. Tang: *Cavity magnomechanics*. Science Advances **2**.3 (2016). DOI: 10.1126/sciadv.1501286.

[58] J. A. Haigh, N. J. Lambert, A. C. Doherty, and A. J. Ferguson: *Dispersive readout of ferromagnetic resonance for strongly coupled magnons and microwave photons*. Physical Review B **91**.10 (2015), p. 104410. DOI: 10.1103/physrevb.91.104410.

[59] S. Viola Kusminskiy, H. X. Tang, and F. Marquardt: *Coupled spin-light dynamics in cavity optomagnonics*. Physical Review A **94** (2016), p. 033821. DOI: 10.1103/PhysRevA.94.033821.

[60] J. Li, S.-Y. Zhu, and G. S. Agarwal: *Magnon-Photon-Phonon Entanglement in Cavity Magnomechanics*. Physical Review Letters **121** (2018), p. 203601. DOI: 10.1103/PhysRevLett.121.203601.

[61] Y. Tabuchi, S. Ishino, T. Ishikawa, R. Yamazaki, K. Usami, and Y. Nakamura: *Hybridizing Ferromagnetic Magnons and Microwave Photons in the Quantum Limit*. Physical Review Letters **113** (2014), p. 083603. DOI: 10.1103/PhysRevLett.113.083603.

[62] M. Pfirrmann, I. Boventer, A. Schneider, T. Wolz, M. Kläui, A. V. Ustinov, and M. Weides: *Magnons at low excitations: Observation of incoherent coupling to a bath of two-level-systems*. Physical Review Research **1** (2019), p. 032023. DOI: 10.1103/PhysRevResearch.1.032023.

[63] S. Kosen, R. G. E. Morris, A. F. van Loo, and A. D. Karenowska: *Measurement of a magnonic crystal at millikelvin temperatures*. Applied Physics Letters **112**.1 (2018), p. 012402. DOI: 10.1063/1.5011767.

[64] S. Kosen, A. F. van Loo, D. A. Bozhko, L. Mihalceanu, and A. D. Karenowska: *Microwave magnon damping in YIG films at millikelvin temperatures*. APL Materials **7**.10 (2019), p. 101120. DOI: 10.1063/1.5115266.

[65] Y. Tabuchi, S. Ishino, A. Noguchi, T. Ishikawa, R. Yamazaki, K. Usami, and Y. Nakamura: *Coherent coupling between a ferromagnetic magnon and a superconducting qubit*. Science **349** (2015), pp. 405–408. DOI: 10.1126/science.aaa3693.

[66] Y. Tabuchi, S. Ishino, A. Noguchi, T. Ishikawa, R. Yamazaki, K. Usami, and Y. Nakamura: *Quantum magnonics: The magnon meets the superconducting qubit*. Comptes Rendus Physique **17**.7 (2016), pp. 729–739. DOI: 10.1016/j.crhy.2016.07.009.

[67] D. Lachance-Quirion, Y. Tabuchi, S. Ishino, A. Noguchi, T. Ishikawa, R. Yamazaki, and Y. Nakamura: *Resolving quanta of collective spin excitations in a millimeter-sized ferromagnet*. Science Advances **3**.7 (2017), e1603150. DOI: 10.1126/sciadv.1603150.

[68] D. Lachance-Quirion, S. P. Wolski, Y. Tabuchi, S. Kono, K. Usami, and Y. Nakamura: *Entanglement-based single-shot detection of a single magnon with a superconducting qubit*. 2019. arXiv: 1910.09096 [quant-ph].

[69] Y.-P. Wang, G.-Q. Zhang, D. Xu, T.-F. Li, S.-Y. Zhu, J. S. Tsai, and J. Q. You: *Amplitude and frequency sensing of microwave fields with a superconducting transmon qudit*. 2019. arXiv: 1903.12498 [quant-ph].

[70] R. G. E. Morris, A. F. van Loo, S. Kosen, and A. D. Karenowska: *Strong coupling of magnons in a YIG sphere to photons in a planar superconducting resonator in the quantum limit*. Scientific Reports **7**.1 (2017), p. 11511. DOI: 10.1038/s41598-017-11835-4.

[71] R. Hisatomi, A. Osada, Y. Tabuchi, T. Ishikawa, A. Noguchi, R. Yamazaki, K. Usami, and Y. Nakamura: *Bidirectional conversion between microwave and light via ferromagnetic magnons*. Physical Review B **93** (2016), p. 174427. DOI: 10.1103/PhysRevB.93.174427.

[72] R. Barbieri, M. Cerdonio, G. Fiorentini, and S. Vitale: *Axion to magnon conversion. A scheme for the detection of galactic axions*. Physics Letters B **226**.3 (1989), pp. 357–360. DOI: 10.1016/0370-2693(89)91209-4.

[73] R. Barbieri, C. Braggio, G. Carugno, C.S. Gallo, A. Lombardi, A. Ortolan, R. Pengo, G. Ruoso, and C.C. Speake: *Searching for galactic axions through magnetized media: The QUAX proposal*. Physics of the Dark Universe **15** (2017), pp. 135–141. DOI: 10.1016/j.dark.2017.01.003.

[74] G. Flower, J. Bourhill, M. Goryachev, and M. E. Tobar: *Broadening frequency range of a ferromagnetic axion haloscope with strongly coupled cavity–magnon polaritons*. Physics of the Dark Universe **25** (2019), p. 100306. DOI: 10.1016/j.dark.2019.100306.

[75] D. Lachance-Quirion, Y. Tabuchi, A. Gloppe, K. Usami, and Y. Nakamura: *Hybrid quantum systems based on magnonics*. Applied Physics Express **12**.7 (2019), p. 070101. DOI: 10.7567/1882-0786/ab248d.

[76] I. Boventer, M. Pfirrmann, J. Krause, Y. Schön, M. Kläui, and M. Weides: *Complex temperature dependence of coupling and dissipation of cavity magnon polaritons from millikelvin to room temperature*. Physical Review B **97** (2018), p. 184420. DOI: 10.1103/PhysRevB.97.184420.

[77] D. M. Pozar: *Microwave engineering*. 4th ed. Hoboken, NJ: Wiley, 2012.

[78] A. A. Clerk, M. H. Devoret, S. M. Girvin, F. Marquardt, and R. J. Schoelkopf: *Introduction to quantum noise, measurement, and amplification*. Reviews of Modern Physics **82** (2010). See supplementary material at http://link.aps.org/supplemental/10.1103/RevModPhys.82.1155 for additional pedagogical appendices which complement the main text of this article., pp. 1155–1208. DOI: 10.1103/RevModPhys.82.1155.

[79] S. M. Girvin: "Circuit QED: superconducting qubits coupled to microwave photons". *Quantum Machines: Measurement and Control of Engineered Quantum Systems*. Ed. by M. Devoret, B. Huard, R. Schoelkopf, and L. F. Cugliandolo. Oxford: Oxford University Press, 2014. Chap. 3, pp. 113–255. DOI: 10.1093/acprof:oso/9780199681181.003.0003.

[80] J. Braumüller: *Quantum simulation experiments with superconducting qubits*. PhD thesis. Karlsruhe Institute of Technology, 2017.

[81] E. Rephaeli and S. Fan: *Dissipation in few-photon waveguide transport*. Photonic Research **1**.3 (2013), pp. 110–114. DOI: 10.1364/PRJ.1.000110.

[82] J. Gao: *The Physics of Superconducting Microwave Resonators*. PhD thesis. California Institute of Technology, 2005.

[83] S. Probst, F. B. Song, P. A. Bushev, A. V. Ustinov, and M. Weides: *Efficient and robust analysis of complex scattering data under noise in microwave resonators*. Review of Scientific Instruments **86**.2 (2015), p. 024706. DOI: 10.1063/1.4907935.

[84] F. Bloch: *Zur Theorie des Ferromagnetismus*. Zeitschrift für Physik **61**.3 (1930), pp. 206–219. DOI: 10.1007/BF01339661.

[85] C. Kittel: *Introduction to solid state physics*. 8th ed. Hoboken, NJ: Wiley, 2005.

[86] D. D. Stancil and A. Prabhakar: *Spin Waves*. New York, NY: Springer, 2009. DOI: 10.1007/978-0-387-77865-5.

[87] A. Auerbach: *Interacting Electrons and Quantum Magnetism*. New York, NY: Springer, 1994. DOI: 10.1007/978-1-4612-0869-3.

[88] L. R. Walker: *Magnetostatic Modes in Ferromagnetic Resonance*. Physical Review **105** (1957), pp. 390–399. DOI: 10.1103/PhysRev.105.390.

[89] L. R. Walker: *Resonant Modes of Ferromagnetic Spheroids*. Journal of Applied Physics **29**.3 (1958), pp. 318–323. DOI: 10.1063/1.1723117.

[90] P. C. Fletcher and R. O. Bell: *Ferrimagnetic Resonance Modes in Spheres*. Journal of Applied Physics **30**.5 (1959), pp. 687–698. DOI: 10.1063/1.1735216.

[91] C. Kittel: *On the Theory of Ferromagnetic Resonance Absorption*. Physical Review **73** (1948), pp. 155–161. DOI: 10.1103/PhysRev.73.155.

[92] G. S. Agarwal: *Vacuum-Field Rabi Splittings in Microwave Absorption by Rydberg Atoms in a Cavity*. Physical Review Letters **53** (1984), pp. 1732–1734. DOI: 10.1103/PhysRevLett.53.1732.

[93] J. H. Wesenberg, A. Ardavan, G. A. D. Briggs, J. J. L. Morton, R. J. Schoelkopf, D. I. Schuster, and K. Mølmer: *Quantum Computing with an Electron Spin Ensemble*. Physical Review Letters **103** (2009), p. 070502. DOI: 10.1103/PhysRevLett.103.070502.

[94] M. Tavis and F. W. Cummings: *Exact Solution for an N-Molecule—Radiation-Field Hamiltonian*. Physical Review **170** (1968), pp. 379–384. DOI: 10.1103/PhysRev.170.379.

[95] R. H. Dicke: *Coherence in Spontaneous Radiation Processes*. Physical Review **93** (1954), pp. 99–110. DOI: 10.1103/PhysRev.93.99.

[96] S. Haroche and J.-M. Raimond: *Exploring the quantum: Atoms, Cavities and Photons*. Oxford graduate texts. Oxford: Oxford Univiversity Press, 2006. DOI: 10.1093/acprof:oso/9780198509141.001.0001.

[97] S. Probst: *Hybrid quantum system based on rare earth doped crystals*. PhD thesis. Karlsruhe Institute of Technology, 2015.

[98] N. J. Lambert, A. Rueda, F. Sedlmeir, and H. G. L. Schwefel: *Coherent conversion between microwave and optical photons – an overview of physical implementations*. 2019. arXiv: 1906.10255 [physics.optics].

[99] L. Bai, M. Harder, Y. P. Chen, X. Fan, J. Q. Xiao, and C.-M. Hu: *Spin Pumping in Electrodynamically Coupled Magnon-Photon Systems*. Physical Review Letters **114** (2015), p. 227201. DOI: 10.1103/PhysRevLett.114.227201.

[100] I. Boventer, C. Dörflinger, T. Wolz, R. Macêdo, R. Lebrun, M. Kläui, and M. Weides: *Control of the Coupling Strength and the Linewidth of a Cavity-Magnon Polariton*. 2019. arXiv: 1904.00393 [cond-mat.mes-hall].

[101] I. Boventer, M. Kläui, R. Macêdo, and M. Weides: *Steering between Level Repulsion and Attraction: Beyond Single-Tone Driven Cavity Magnon-Polaritons*. 2019. arXiv: 1908.05439 [cond-mat.mes-hall].

[102] T. Wolz, A. Stehli, A. Schneider, I. Boventer, R. Macêdo, A. V. Ustinov, M. Kläui, and M. Weides: *Introducing coherent time control to cavity-magnon-polariton modes*. 2019. arXiv: 1906.08103 [cond-mat.mes-hall].

[103] L. Knöll and D.-G. Welsch: *QED of resonators in quantum optics*. Progress in Quantum Electronics **16**.3 (1992), pp. 135–182. DOI: 10.1016/0079-6727(92)90002-D.

[104] C. W. Gardiner and M. J. Collett: *Input and output in damped quantum systems: Quantum stochastic differential equations and the master equation*. Physical Review A **31** (1985), pp. 3761–3774. DOI: 10.1103/PhysRevA.31.3761.

[105] S. Fan, Ş. E. Kocabaş, and J.-T. Shen: *Input-output formalism for few-photon transport in one-dimensional nanophotonic waveguides coupled to a qubit*. Physical Review A **82** (2010), p. 063821. DOI: 10.1103/PhysRevA.82.063821.

[106] P. M. Alsing, E. E. Hach, C. C. Tison, and A. M. Smith: *Quantum-optical description of losses in ring resonators based on field-operator transformations*. Physical Review A **95** (2017), p. 053828. DOI: 10.1103/PhysRevA.95.053828.

[107] A. J. Princep, R. A. Ewings, S. Ward, S. Tóth, C. Dubs, D. Prabhakaran, and A. T. Boothroyd: *The full magnon spectrum of yttrium iron garnet*. npj Quantum Materials **2**.1 (2017), p. 63. DOI: 10.1038/s41535-017-0067-y.

[108] B. Heinrich and Z. Frait: *Temperature Dependence of the FMR Linewidth of Iron Single-Crystal Platelets*. physica status solidi (b) **16**.1 (1966), K11–K14. DOI: 10.1002/pssb.19660160138.

[109] C. E. Patton: *Linewidth and Relaxation Processes for the Main Resonance in the Spin-Wave Spectra of Ni–Fe Alloy Films*. Journal of Applied Physics **39**.7 (1968), pp. 3060–3068. DOI: 10.1063/1.1656733.

[110] V. E. Demidov, S. O. Demokritov, K. Rott, P. Krzysteczko, and G. Reiss: *Linear and nonlinear spin-wave dynamics in macro- and microscopic magnetic confined structures*. Journal of Physics D: Applied Physics **41**.16 (2008), p. 164012. DOI: 10.1088/0022-3727/41/16/164012.

[111] A. V. Chumak, P. Pirro, A. A. Serga, M. P. Kostylev, R. L. Stamps, H. Schultheiss, K. Vogt, S. J. Hermsdoerfer, B. Laegel, P. A. Beck, and B. Hillebrands: *Spin-wave propagation in a microstructured magnonic crystal*. Applied Physics Letters **95**.26 (2009), p. 262508. DOI: 10.1063/1.3279138.

[112] A. A. Serga, A. V. Chumak, and B. Hillebrands: *YIG magnonics*. Journal of Physics D: Applied Physics **43**.26 (2010), p. 264002. DOI: 10.1088/0022-3727/43/26/264002.

[113] Y. Kajiwara, K. Harii, S. Takahashi, J. Ohe, K. Uchida, M. Mizuguchi, H. Umezawa, H. Kawai, K. Ando, K. Takanashi, S. Maekawa, and E. Saitoh: *Transmission of electrical signals by spin-wave interconversion in a magnetic insulator*. Nature **464** (2010), pp. 262–266. DOI: 10.1038/nature08876.

[114] A. V. Chumak, A. A. Serga, and B. Hillebrands: *Magnon transistor for all-magnon data processing*. Nature Communications **5** (2014), 4700 EP -. DOI: 10.1038/ncomms5700;.

[115] D. Zhang, X.-M. Wang, T.-F. Li, X.-Q. Luo, W. Wu, F. Nori, and J.-Q. You: *Cavity quantum electrodynamics with ferromagnetic magnons in a small yttrium-iron-garnet sphere*. npj Quantum Information **1** (2015), 15014 EP -. DOI: http://dx.doi.org/10.1038/npjqi.2015.14.

[116] X. Zhang, C.-L. Zou, L. Jiang, and H. X. Tang: *Cavity magnomechanics*. Science Advances **2**.3 (2016). DOI: 10.1126/sciadv.1501286.

[117] I. A. Golovchanskiy, N. N. Abramov, M. Pfirrmann, T. Piskor, J. N. Voss, D. S. Baranov, R. A. Hovhannisyan, V. S. Stolyarov, C. Dubs, A. A. Golubov, V. V. Ryazanov, A. V. Ustinov, and M. Weides: *Interplay of Magnetization Dynamics with a Microwave Waveguide at Cryogenic Temperatures*. Physical Review Applied **11** (2019), p. 044076. DOI: 10.1103/PhysRevApplied.11.044076.

[118] V. Cherepanov, I. Kolokolov, and V. L'vov: *The saga of YIG: Spectra, thermodynamics, interaction and relaxation of magnons in a complex magnet*. Physics Reports **229**.3 (1993), pp. 81–144. DOI: 10.1016/0370-1573(93)90107-O.

[119] V. L. Safonov: *Nonequilibrium magnons: theory, experiment and applications*. Weinheim: Wiley-VCH, 2013. DOI: 10.1002/9783527670536.

[120] R.W. Teale and K. Tweedale: *Ytterbium-ion relaxation in ferrimagnetic resonance*. Physics Letters **1**.7 (1962), pp. 298–300. DOI: 10.1016/0031-9163(62)91392-6.

[121] P. E. Seiden: *Ferrimagnetic Resonance Relaxation in Rare-Earth Iron Garnets*. Physical Review **133** (1964), A728–A736. DOI: 10.1103/PhysRev.133.A728.

[122] B. H. Clarke, K. Tweedale, and R. W. Teale: *Rare-Earth Ion Relaxation Time and G Tensor in Rare-Earth-Doped Yttrium Iron Garnet. I. Ytterbium*. Physical Review **139** (1965), A1933–A1943. DOI: 10.1103/PhysRev.139.A1933.

[123] M. Sparks: *Ferromagnetic-relaxation theory*. McGraw-Hill advanced physics monograph series. New York: McGraw-Hill, 1964.

[124] M. Sparks: *Effect of Impurities on the Microwave Properties of Yttrium Iron Garnet*. Journal of Applied Physics **38**.3 (1967), pp. 1031–1038. DOI: 10.1063/1.1709475.

[125] R. C. LeCraw, E. G. Spencer, and C. S. Porter: *Ferromagnetic Resonance Line Width in Yttrium Iron Garnet Single Crystals*. Physical Review **110** (1958), pp. 1311–1313. DOI: 10.1103/PhysRev.110.1311.

[126] R. C. Fletcher, R. C. LeCraw, and E. G. Spencer: *Electron Spin Relaxation in Ferromagnetic Insulators*. Physical Review **117** (1960), pp. 955–963. DOI: 10.1103/PhysRev.117.955.

[127] E. G. Spencer and R. C. LeCraw: *Spin-Lattice Relaxation in Yttrium Iron Garnet*. Physical Review Letters **4** (1960), pp. 130–131. DOI: 10.1103/PhysRevLett.4.130.

[128] M. Sparks, R. Loudon, and C. Kittel: *Ferromagnetic Relaxation. I. Theory of the Relaxation of the Uniform Precession and the Degenerate Spectrum in Insulators at Low Temperatures*. Physical Review **122** (1961), pp. 791–803. DOI: 10.1103/PhysRev.122.791.

[129] J. Nemarich: *Contribution of the Two-Magnon Process to Magnetostatic-Mode Relaxation*. Physical Review **136** (1964), A1657–A1664. DOI: 10.1103/PhysRev.136.a1657.

[130] P. W. Anderson, B. I. Halperin, and C. M. Varma: *Anomalous low-temperature thermal properties of glasses and spin glasses*. The Philosophical Magazine: A Journal of Theoretical Experimental and Applied Physics **25**.1 (1972), pp. 1–9. DOI: 10.1080/14786437208229210.

[131] W. A. Phillips: *Tunneling states in amorphous solids*. Journal of Low Temperature Physics **7**.3 (1972), pp. 351–360. DOI: 10.1007/BF00660072.

[132] W. A. Phillips: *Two-level states in glasses*. Reports on Progress in Physics **50**.12 (1987), p. 1657. DOI: 0034-4885/50/i=12/a=003.

[133] J. M. Martinis and A. Magrant: *UCSB final report for the CSQ program: Review of decoherence and materials physics for superconducting qubits*. 2014. arXiv: 1410.5793 [quant-ph].

[134] C. Müller, J. H. Cole, and J. Lisenfeld: *Towards understanding two-level-systems in amorphous solids: insights from quantum circuits*. Reports on Progress in Physics **82**.12 (2019), p. 124501. DOI: 10.1088/1361-6633/ab3a7e.

[135] M. Imboden and P. Mohanty: *Evidence of universality in the dynamical response of micromechanical diamond resonators at millikelvin temperatures*. Physical Review B **79** (2009), p. 125424. DOI: 10.1103/PhysRevB.79.125424.

[136] F. Hoehne, Yu. A. Pashkin, O. Astafiev, L. Faoro, L. B. Ioffe, Y. Nakamura, and J. S. Tsai: *Damping in high-frequency metallic nanomechanical resonators*. Physical Review B **81** (2010), p. 184112. DOI: 10.1103/PhysRevB.81.184112.

[137] T. Faust, J. Rieger, M. J. Seitner, J. P. Kotthaus, and E. M. Weig: *Signatures of two-level defects in the temperature-dependent damping of nanomechanical silicon nitride resonators*. Physical Review B **89** (2014), p. 100102. DOI: 10.1103/PhysRevB.89.100102.

[138] I. W. Martin, R. Nawrodt, K. Craig, C. Schwarz, R. Bassiri, G. Harry, J. Hough, S. Penn, S. Reid, R. Robie, and S. Rowan: *Low temperature mechanical dissipation of an ion-beam sputtered silica film*. Classical and Quantum Gravity **31**.3 (2014), p. 035019. DOI: 10.1088/0264-9381/31/3/035019.

[139] M. J. Kirton and M. J. Uren: *Noise in solid-state microstructures: A new perspective on individual defects, interface states and low-frequency (1/f) noise*. Advances in Physics **38**.4 (1989), pp. 367–468. DOI: 10.1080/00018738900101122.

[140] C. Enss and S. Hunklinger: *Low-temperature physics*. Berlin: Springer, 2005. DOI: 10.1007/b137878.

[141] F. Bloch: *Nuclear Induction*. Physical Review **70** (1946), pp. 460–474. DOI: 10.1103/PhysRev.70.460.

[142] S. Hunklinger and W. Arnold: "Ultrasonic Properties of Glasses at Low Temperatures". Vol. 12. Physical Acoustics. Academic Press, 1976, pp. 155–215. DOI: 10.1016/B978-0-12-477912-9.50008-4.

[143] J. Reinisch and A. Heuer: *What Is Moving in Silica at 1 K? A Computer Study of the Low-Temperature Anomalies*. Physical Review Letters **95** (2005), p. 155502. DOI: 10.1103/PhysRevLett.95.155502.

[144] J. M. Martinis, K. B. Cooper, R. McDermott, M. Steffen, M. Ansmann, K. D. Osborn, K. Cicak, S. Oh, D. P. Pappas, R. W. Simmonds, and C. C. Yu: *Decoherence in Josephson Qubits from Dielectric Loss*. Physical Review Letters **95** (2005), p. 210503. DOI: 10.1103/PhysRevLett.95.210503.

[145] K. Agarwal, I. Martin, M. D. Lukin, and E. Demler: *Polaronic model of two-level systems in amorphous solids*. Physical Review B **87** (2013), p. 144201. DOI: 10.1103/PhysRevB.87.144201.

[146] P. Kumar, S. Sendelbach, M. A. Beck, J. W. Freeland, Z. Wang, H. Wang, C. C. Yu, R. Q. Wu, D. P. Pappas, and R. McDermott: *Origin and Reduction of 1/f Magnetic Flux Noise in Superconducting Devices*. Physical Review Applied **6** (2016), p. 041001. DOI: 10.1103/PhysRevApplied.6.041001.

[147] S. E. de Graaf, A. A. Adamyan, T. Lindström, D. Erts, S. E. Kubatkin, A. Ya. Tzalenchuk, and A. V. Danilov: *Direct Identification of Dilute Surface Spins on Al_2O_3: Origin of Flux Noise in Quantum Circuits*. Physical Review Letters **118** (2017), p. 057703. DOI: 10.1103/PhysRevLett.118.057703.

[148] S. E. de Graaf, L. Faoro, J. Burnett, A. A. Adamyan, A. Ya. Tzalenchuk, S. E. Kubatkin, T. Lindström, and A. V. Danilov: *Suppression of low-frequency charge noise in superconducting resonators by surface spin desorption*. Nature Communications **9**.1 (2018), p. 1143. DOI: 10.1038/s41467-018-03577-2.

[149] G. Lindblad: *On the generators of quantum dynamical semigroups*. Communications in Mathematical Physics **48**.2 (1976), pp. 119–130. DOI: 10.1007/BF01608499.

[150] N. F. Ramsey: *A New Molecular Beam Resonance Method*. Physical Review **76** (1949), p. 996. DOI: 10.1103/PhysRev.76.996.

[151] I. I. Rabi: *Space Quantization in a Gyrating Magnetic Field*. Physical Review **51** (1937), pp. 652–654. DOI: 10.1103/PhysRev.51.652.

[152] J. J. Sakurai and J. Napolitano: *Modern Quantum Mechanics*. 2nd ed. Cambridge: Cambridge University Press, 2017. DOI: 10.1017/9781108499996.

[153] M. A. Nielsen and I. L. Chuang: *Quantum Computation and Quantum Information*. 10th anniversary ed. Cambridge: Cambridge University Press, 2010. DOI: 10.1017/CBO9780511976667.

[154] A. M. Zagoskin: *Quantum Engineering: Theory and Design of Quantum Coherent Structures*. Cambridge: Cambridge University Press, 2011. DOI: 10.1017/CBO9780511844157.

[155] V. L. Ginzburg and L. D. Landau: *On the theory of superconductivity*. Zhurnal Éksperimental'noĭ i Teoreticheskoĭ Fiziki **20** (1959). (English translation in: *Collected papers of L. D. Landau*. Ed. by D. Ter Haar. Oxford: Pergamon Press, 1965. p. 546), p. 1064.

[156] J. Bardeen, L. N. Cooper, and J. R. Schrieffer: *Theory of Superconductivity*. Physical Review **108** (1957), pp. 1175–1204. DOI: 10.1103/PhysRev.108.1175.

[157] H. Kamerlingh Onnes: *Further experiments with liquid helium. C. On the change of electric resistance of pure metals at very low temperatures etc. IV. The resistance of pure mercury at helium temperatures*. Commununications from the Laboratory of Physics at the University of Leiden **13** (1911), pp. 1274–1276.

[158] W. Meißner and R. Ochsenfeld: *Ein neuer Effekt bei Eintritt der Supraleitfähigkeit*. Naturwissenschaften **21**.44 (1933), pp. 787–788. DOI: 10.1007/BF01504252.

[159] H. Rotzinger, S. T. Skacel, M. Pfirrmann, J. N. Voss, J. Münzberg, S. Probst, P. Bushev, M. P. Weides, A. V. Ustinov, and J. E. Mooij: *Aluminium-oxide wires for superconducting high kinetic inductance circuits*. Superconductor Science and Technology **30**.2 (2016), p. 025002. DOI: 10.1088/0953-2048/30/2/025002.

[160] L. Grünhaupt, N. Maleeva, S. T. Skacel, M. Calvo, F. Levy-Bertrand, A. V. Ustinov, H. Rotzinger, A. Monfardini, G. Catelani, and I. M. Pop: *Loss Mechanisms and Quasiparticle Dynamics in Superconducting Microwave Resonators Made of Thin-Film Granular Aluminum*. Physical Review Letters **121** (2018), p. 117001. DOI: 10.1103/PhysRevLett.121.117001.

[161] N. Maleeva, L. Grünhaupt, T. Klein, F. Levy-Bertrand, O. Dupre, M. Calvo, F. Valenti, P. Winkel, F. Friedrich, W. Wernsdorfer, A. V. Ustinov, H. Rotzinger, A. Monfardini, M. V. Fistul, and I. M. Pop: *Circuit quantum electrodynamics of granular aluminum resonators*. Nature Communications **9**.1 (2018), p. 3889. DOI: 10.1038/s41467-018-06386-9.

[162] B. D. Josephson: *Possible new effects in superconductive tunnelling*. Physics Letters **1**.7 (1962), pp. 251–253. DOI: 10.1016/0031-9163(62)91369-0.

[163] J. Koch, T. M. Yu, J. Gambetta, A. A. Houck, D. I. Schuster, J. Majer, A. Blais, M. H. Devoret, S. M. Girvin, and R. J. Schoelkopf: *Charge-insensitive qubit design derived from the Cooper pair box*. Physical Review A **76** (2007). DOI: 10.1103/physreva.76.042319.

[164] V. Bouchiat, D. Vion, P. Joyez, D. Esteve, and M. H. Devoret: *Quantum Coherence with a Single Cooper Pair*. Physica Scripta **T76**.1 (1998), p. 165. DOI: 10.1238/physica.topical.076a00165.

[165] M. H. Devoret: "Quantum Fluctuations in Electrical Circuits". *Quantum Fluctuations*. Ed. by S. Reynaud, E. Giacobino, and J. Zinn-Justin. Amsterdam: Elsevier, 1997. Chap. 10, pp. 351–386. URL: http://qulab.eng.yale.edu/documents/reprints/Houches_fluctuations.pdf.

[166] I. I. Rabi: *On the Process of Space Quantization*. Physical Review **49** (1936), pp. 324–328. DOI: 10.1103/PhysRev.49.324.

[167] E. T. Jaynes and F. W. Cummings: *Comparison of quantum and semiclassical radiation theories with application to the beam maser*. Proceedings of the IEEE **51**.1 (1963), pp. 89–109. DOI: 10.1109/PROC.1963.1664.

[168] D. I. Schuster: *Circuit Quantum Electrodynamics*. PhD thesis. Yale University, 2007.

[169] J. Gambetta, M. Blais, D. I. Schuster, A. Wallraff, L. Frunzio, J. Majer, M. H. Devoret, S. M. Girvin, and R. J. Schoelkopf: *Qubit-photon interactions in a cavity: Measurement-induced dephasing and number splitting*. Physical Review A **74** (2006), p. 042318. DOI: 10.1103/PhysRevA.74.042318.

[170] D. I. Schuster, A. A. Houck, J. A. Schreier, A. Wallraff, J. M. Gambetta, A. Blais, L. Frunzio, J. Majer, B. Johnson, M. H. Devoret, S. M. Girvin, and R. J. Schoelkopf: *Resolving photon number states in a superconducting circuit*. Nature **445** (2007), 515 EP -. DOI: 10.1038/nature05461;.

[171] Z. Leghtas, G. Kirchmair, B. Vlastakis, M. H. Devoret, R. J. Schoelkopf, and M. Mirrahimi: *Deterministic protocol for mapping a qubit to coherent state superpositions in a cavity*. Physical Review A **87** (2013), p. 042315. DOI: 10.1103/PhysRevA.87.042315.

[172] B. Vlastakis, G. Kirchmair, Z. Leghtas, S. E. Nigg, L. Frunzio, S. M. Girvin, M. Mirrahimi, M. H. Devoret, and R. J. Schoelkopf: *Deterministically Encoding Quantum Information Using 100-Photon Schrödinger Cat States*. Science **342**.6158 (2013), pp. 607–610. DOI: 10.1126/science.1243289.

[173] I. Scholz, J. D. van Beek, and M. Ernst: *Operator-based Floquet theory in solid-state NMR*. Solid State Nuclear Magnetic Resonance **37**.3 (2010), pp. 39–59. DOI: 10.1016/j.ssnmr.2010.04.003.

[174] E. Rephaeli and S. Fan: *Stimulated Emission from a Single Excited Atom in a Waveguide*. Physical Review Letters **108** (2012), p. 143602. DOI: 10.1103/PhysRevLett.108.143602.

[175] E. Rephaeli and S. Fan: *Few-Photon Single-Atom Cavity QED With Input-Output Formalism in Fock Space*. IEEE Journal of Selected Topics in Quantum Electronics **18**.6 (2012), pp. 1754–1762. DOI: 10.1109/JSTQE.2012.2196261.

[176] A. Barone and G. Paternò: *Physics and Applications of the Josephson Effect*. New York, NY: Wiley, 1982. DOI: 10.1002/352760278X.

[177] A. Schneider, T. Wolz, M. Pfirrmann, M. Spiecker, H. Rotzinger, A. V. Ustinov, and M. Weides: *Transmon qubit in a magnetic field: Evolution of coherence and transition frequency*. Physical Review Research **1** (2019), p. 023003. DOI: 10.1103/PhysRevResearch.1.023003.

[178] D. Bothner, T. Gaber, M. Kemmler, D. Koelle, R. Kleiner, S. Wünsch, and M. Siegel: *Magnetic hysteresis effects in superconducting coplanar microwave resonators*. Physical Review B **86** (2012), p. 014517. DOI: 10.1103/PhysRevB.86.014517.

[179] X. Xi, J. Hwang, C. Martin, D. H. Reitze, C. J. Stanton, D. B. Tanner, and G. L. Carr: *Effect of a magnetic field on the quasiparticle recombination in superconductors*. Physical Review B **87** (2013), p. 140502. DOI: 10.1103/PhysRevB.87.140502.

[180] C. Wang, Y. Y. Gao, I. M. Pop, U. Vool, C. Axline, T. Brecht, R. W. Heeres, L. Frunzio, M. H. Devoret, G. Catelani, L. I. Glazman, and R. J. Schoelkopf: *Measurement and control of quasiparticle dynamics in a superconducting qubit*. Nature Communications **5**.1 (2014), p. 5836. DOI: 10.1038/ncomms6836.

[181] S. Kwon, A. Fadavi Roudsari, O. W. B. Benningshof, Y.-C. Tang, H. R. Mohebbi, I. A. J. Taminiau, D. Langenberg, S. Lee, G. Nichols, D. G. Cory, and G.-X. Miao: *Magnetic field dependent microwave losses in superconducting niobium microstrip resonators*. Journal of Applied Physics **124**.3 (2018), p. 033903. DOI: 10.1063/1.5027003.

[182] G. J. Dolan: *Offset masks for lift-off photoprocessing*. Applied Physics Letters **31**.5 (1977), pp. 337–339. DOI: 10.1063/1.89690.

[183] F. Pobell: *Matter and methods at low temperatures*. 3rd review and expanded ed. Berlin: Springer, 2007. DOI: 10.1007/978-3-540-46360-3.

[184] R. Gebauer: *FPGA-based Quantum Feedback for Superconducting Qubits*. MA thesis. Karlsruhe Institute of Technology, 2018.

[185] *Qkit – a quantum measurement and evaluation suite in python*. URL: https://github.com/qkitgroup/qkit.

[186] M. A. Continentino: *Tunneling states in ferromagnetic glasses*. Solid State Communications **38**.10 (1981), pp. 981–984. DOI: 10.1016/0038-1098(81)90792-4.

[187] M. A. Continentino: *Structural relaxation in ferromagnetic glasses*. Journal of Physics C: Solid State Physics **14**.24 (1981), pp. 3527–3539. DOI: 10.1088/0022-3719/14/24/009.

[188] M. A. Continentino: *Dynamic theory of ferromagnetic–to–spin-glass transition*. Physical Review B **27** (1983), pp. 4351–4358. DOI: 10.1103/PhysRevB.27.4351.

[189] M. A. Continentino: *Theory of dilute ferromagnets*. Journal of Physics C: Solid State Physics **16**.3 (1983), pp. L71–L75. DOI: 10.1088/0022-3719/16/3/004.

[190] C. Arzoumanian, A. M. De Goër, B. Salce, and F. Holtzberg: *A study of the insulating spin-glass $Eu_{0.44}Sr_{0.56}S$ by low temperature thermal conductivity measurements*. Journal de Physique Lettres **44**.1 (1983), pp. 39–45. DOI: 10.1051/jphyslet:0198300440103900.

[191] E. F. Wassermann and D. M. Herlach: *Experimental evidence for magnetic two level systems in spin glasses (invited)*. Journal of Applied Physics **55**.6 (1984), pp. 1709–1713. DOI: 10.1063/1.333451.

[192] D. Wesenberg, T. Liu, D. Balzar, M. Wu, and B. L. Zink: *Long-distance spin transport in a disordered magnetic insulator*. Nature Physics **13** (2017), 987 EP -. DOI: 10.1038/nphys4175.

[193] R. N. Kleiman, G. Agnolet, and D. J. Bishop: *Two-level systems observed in the mechanical properties of single-crystal silicon at low temperatures*. Physical Review Letters **59** (1987), pp. 2079–2082. DOI: 10.1103/PhysRevLett.59.2079.

[194] S. Streib, N. Vidal-Silva, K. Shen, and G. E. W. Bauer: *Magnon-phonon interactions in magnetic insulators*. Physical Review B **99** (2019), p. 184442. DOI: 10.1103/PhysRevB.99.184442.

[195] V. Ambegaokar and A. Baratoff: *Tunneling Between Superconductors*. Physical Review Letters **10** (1963), pp. 486–489. DOI: 10.1103/PhysRevLett.10.486.

[196] D. I. Schuster, A. Wallraff, A. Blais, L. Frunzio, R.-S. Huang, J. Majer, S. M. Girvin, and R. J. Schoelkopf: *ac Stark Shift and Dephasing of a Superconducting Qubit Strongly Coupled to a Cavity Field*. Physical Review Letters **94** (2005). DOI: 10.1103/physRevLett.94.123602.

[197] A. Schneider, J. Braumüller, L. Guo, P. Stehle, H. Rotzinger, M. Marthaler, A. V. Ustinov, and M. Weides: *Local sensing with the multilevel ac Stark effect*. Physical Review A **97** (2018), p. 062334. DOI: 10.1103/PhysRevA.97.062334.

[198] M. Kristen, A. Schneider, A. Stehli, T. Wolz, S. Danilin, H. S. Ku, D. P. Pappas, A. V. Ustinov, and M. Weides: *Amplitude and frequency sensing of microwave fields with a superconducting transmon qudit*. 2019. arXiv: 1908.09556 [quant-ph].

[199] N. F. Ramsey: *A Molecular Beam Resonance Method with Separated Oscillating Fields*. Physical Review **78** (1950), pp. 695–699. DOI: 10.1103/PhysRev.78.695.

[200] J. R. Johansson, P. D. Nation, and F. Nori: *QuTiP 2: A Python framework for the dynamics of open quantum systems*. Computer Physics Communications **184**.4 (2013), pp. 1234–1240. DOI: 10.1016/j.cpc.2012.11.019.

[201] E. L. Hahn: *Spin Echoes*. Physical Review **80** (1950), pp. 580–594. DOI: 10.1103/PhysRev.80.580.

List of publications

1. I. Boventer, **M. Pfirrmann**, J. Krause, Y. Schön, M. Kläui, and M. Weides: *Complex temperature dependence of coupling and dissipation of cavity magnon polaritons from millikelvin to room temperature*. Physical Review B **97** (2018), p. 184420. DOI: http://dx.doi.org/10.1103/PhysRevB.97.184420.

2. I. A. Golovchanskiy, N. N. Abramov, **M. Pfirrmann**, T. Piskor, J. N. Voss, D. S. Baranov, R. A. Hovhannisyan, V. S. Stolyarov, C. Dubs, A. A. Golubov, V. V. Ryazanov, A. V. Ustinov, and M. Weides: *Interplay of Magnetization Dynamics with a Microwave Waveguide at Cryogenic Temperatures*. Physical Review Applied **11** (2019), p. 044076. DOI: 10.1103/PhysRevApplied.11.044076.

3. A. Schneider, T. Wolz, **M. Pfirrmann**, M. Spiecker, H. Rotzinger, A. V. Ustinov, and M. Weides: *Transmon qubit in a magnetic field: Evolution of coherence and transition frequency*. Physical Review Research **1** (2019), p. 023003. DOI: 10.1103/PhysRevResearch.1.023003.

4. **M. Pfirrmann**, I. Boventer, A. Schneider, T. Wolz, M. Kläui, A. V. Ustinov, and M. Weides: *Magnons at low excitations: Observation of incoherent coupling to a bath of two-level-systems*. Physical Review Research **1** (2019), p. 032023. DOI: 10.1103/PhysRevResearch.1.032023.

Appendix

A Fabrication parameters

Table 1: Substrate cleaning

solvent	ultrasonic bath	IPA	H_2O	hot plate
NEP	10 min	yes	yes	100 °C, 5 min

Table 2: Application of the resist stack

resist	pre	spin	reflow	hotplate
LOR 500nm	300 rpm, 10 s	3000 rpm, 60 s	30 s	180 °C, 5 min
PMMA 950K AR-P672.03	300 rpm, 10 s	6000 rpm, 60 s	30 s	145 °C, 5 min

Table 3: Electron beam lithography with a 10 keV ***JEOL*** **writer**

	writing current	dose
STRUCTS	1 nA	300 µC cm^{-2}
STRUCTS	100 pA	300 µC cm^{-2}
STRUCTS	100 pA	60 µC cm^{-2}

Table 4: Development

developer	time	rinse	dry on spin coater
MIBK/IPA 1:3, 25 °C	65 s	IPA (65 s), H_2O (60 s)	7500 rpm, 120 s
MIF 726/H_2O 3:2	120 s	H_2O (60 s)	7500 rpm, 120 s

Table 5: Plasma clean with Kaufman source, *PLASSYS*

gas mixture	plasma voltage	current	time
Ar (4 sccm), O_2 (0.5 sccm)	200 V	10 mA	20 s

Table 6: Al evaporation, shadow angle, *PLASSYS*

	angle	rate	thickness
Layer 1	8°	0.2 nm s^{-1}	30 nm
Layer 2	−8°	0.2 nm s^{-1}	50 nm

Table 7: Lift-off

solvent	temperature	time	ultrasonic bath	rinse
NEP	90 °C	4 h	1 min	IPA, H_2O

Acknowledgements

First of all, I want to thank Prof. Martin Weides. He trusted me to be his first PhD student on the "quantum-magnonics" project and gave me the opportunity to attend various seminars, workshops, and conferences. He provided me with constant support and input concerning the project, as well as encouragement over the last years and was always only a fast email response or a Skype call away, despite moving to his new home in Glasgow. Thank you very much.

I would like to thank Prof. Alexey V. Ustinov for not only being my second reviewer, but also accepting me as a master student before my PhD thesis. Thank you for all the seminars that I was able to attend and for all the general scientific input that I received over the years.

I want to thank my magnonic colleagues at KIT, Andre Schneider and Tim Wolz, for the scientific collaboration and friendship beyond the workplace. I really appreciated the time and effort we spent together on the new fridge and measurement setup and the journey into this "something with magnets"-field that was new to us all. Thank you also very much for the helpful feedback regarding presentations, paper manuscript, and this thesis. Additionally, I would like to thank Isabella Boventer for the fruitful cooperation between the labs at KIT and the University of Mainz.

A special thanks goes to Hannes Rotzinger, for contributing so much to the overall research in our labs. It was a pleasure to continue working with him in his role as the driving force and visionary of the qkit software project after we parted scientific ways as I finished my master's thesis. I very much enjoyed his rich lab experience, various fun-fact discussions, and encouraging words.

I want to thank my officemates, Alexander Bilmes, Yannick Schön, and Alexander Stehli, for the great office environment, which resulted in all of us getting noise-canceling headphones in order to be productive.
I want to thank the former "quantum-magnonics" students who worked in some capacity together with me during this thesis. Thank you Tomi, Stefan, Tine, and especially Julius, who convinced me to share his excitement for sailing trips.
Thanks to all my coworkers of the Weides Lab at Glasgow University, all former and current Fluxons, and the rest of my colleagues at the Institute of Physics. There

were a lot of work-related and off-topic discussions and many memorable moments which we shared together. Thank you for this wonderful time.
Many thanks go to Sebastian Skacel for our regular dinner meetings and his many appreciated advice.

There is much to thank for regarding the infrastructural units at our institute, since they are an integral part in keeping the scientific work rolling.
A big thanks goes to our mechanical and electrical workshops under the management of Michael Meyer and Patrick Rust. Designing all the custom made parts for the cryostat setup with them, I learned a great deal about interdisciplinary communication besides the mechanical and electrical intricacies.
My thanks go to our secretary's office, Steffi Baatz and Claudia Alaya, for their indispensable help through the jungle of university bureaucracy, from ordering forms and holiday requests to business travel applications.

I want to acknowledge financial support by the Helmholtz International Research School for Teratronics (HIRST).

Der größte Dank geht an meine Eltern, Großeltern und meinen Bruder. Für jegliche Unterstützung in allen Lebenslagen abseits der Physik. Ohne diese wäre mein Studium und diese Arbeit nicht möglich gewesen.

Dankeschön an alle Elferräte, Gardemädels und Prinzessinnen des TV. Für die harte Arbeit und den Spaß zwischen Anfang November und Ende Februar.

Zum Schluss möchte ich mich noch bei meiner zweiten Familie bedanken. Markus, Dave, Christoph, Felli, Rabea, Micha, Lis, Simon, Simone. Für das, was ihr aus mir gemacht habt. Für alles. And for more to come. Und wie in der Wissenschaft, so steht man auch hier auf den Schultern von Giganten. Fütterer, Sascha, Chris, Steffi, Werner.

Danke.

Marco Pfirrmann Karlsruhe, November 2019

Experimental Condensed Matter Physics
(ISSN 2191-9925)

Herausgeber
Physikalisches Institut

Prof. Dr. David Hunger
Prof. Dr. Alexey Ustinov
Prof. Dr. Georg Weiß
Prof. Dr. Wolfgang Wernsdorfer
Prof. Dr. Wulf Wulfhekel

Band 1 Alexey Feofanov
Experiments on flux qubits with pi-shifters. 2011
ISBN 978-3-86644-644-1

Band 2 Stefan Schmaus
Spintronics with individual metal-organic molecules. 2011
ISBN 978-3-86644-649-6

Band 3 Marc Müller
Elektrischer Leitwert von magnetostriktiven Dy-Nanokontakten. 2011
ISBN 978-3-86644-726-4

Band 4 Torben Peichl
Einfluss mechanischer Deformation auf atomare Tunnelsysteme – untersucht mit Josephson Phasen-Qubits. 2012
ISBN 978-3-86644-837-7

Band 5 Dominik Stöffler
Herstellung dünner metallischer Brücken durch Elektromigration und Charakterisierung mit Rastersondentechniken. 2012
ISBN 978-3-86644-843-8

Band 6 Tihomir Tomanic
Untersuchung des elektronischen Oberflächenzustands von Ag-Inseln auf supraleitendem Niob (110). 2012
ISBN 978-3-86644-898-8

Band 7 Lukas Gerhard
Magnetoelectric coupling at metal surfaces. 2013
ISBN 978-3-7315-0063-6

Band 8 Nicht erschienen.

Die Bände sind unter www.ksp.kit.edu als PDF frei verfügbar oder als Druckausgabe bestellbar.

Band 9 Jochen Zimmer
Cooper pair transport in arrays of Josephson junctions. 2014
ISBN 978-3-7315-0130-5

Band 10 Oliver Berg
Elektrischer Transport durch Nanokontakte von Selten-Erd-Metallen. 2014
ISBN 978-3-7315-0209-8

Band 11 Grigorij Jur'evic Grabovskij
Investigation of coherent microscopic defects inside the tunneling barrier of a Josephson junction. 2014
ISBN 978-3-7315-0210-4

Band 12 Cornelius Thiele
STM Characterization of Phenylene-Ethynylene Oligomers on Au(111) and their Integration into Carbon Nanotube Nanogaps. 2014
ISBN 978-3-7315-0235-7

Band 13 Michael Peter Schackert
Scanning Tunneling Spectroscopy on Electron-Boson Interactions in Superconductors. 2014
ISBN 978-3-7315-0238-8

Band 14 Susanne Butz
One-Dimensional Tunable Josephson Metamaterials. 2014
ISBN 978-3-7315-0271-5

Band 15 Philipp Jung
Nonlinear Effects in Superconducting Quantum Interference Meta-Atoms. 2014
ISBN 978-3-7315-0294-4

Band 16 Sebastian Probst
Hybrid quantum system based on rare earth doped crystals. 2016
ISBN 978-3-7315-0345-3

Band 17 Wolfram Kittler
Magnetische Anisotropie und Quantenphasenübergang in $CeTi_{1-x}V_xGe_3$. 2015
ISBN 978-3-7315-0363-7

Band 18 Moritz Peter
Towards magnetic resonance in scanning tunneling microscopy using heterodyne detection. 2015
ISBN 978-3-7315-0410-8

Band 19 Junji Tobias Märkl
Investigation of Magnetic Adatoms with Scanning Tunneling Techniques. 2015
ISBN 978-3-7315-0435-1

Band 20 Jochen Braumüller
Quantum simulation experiments with superconducting circuits. 2018
ISBN 978-3-7315-0780-2

Band 21 Jinjie Chen
Local Investigation of Single Magnetic Molecules with Scanning Tunneling Microscopy. 2018
ISBN 978-3-7315-0819-9

Band 22 Arnold Seiler
Einfluss der Leitungselektronen auf die Dynamik atomarer Tunnelsysteme in ungeordneten Festkörpern: Relaxationsprozesse in metallischen Gläsern und ungeordneten dünnen Aluminiumoxid-Schichten. 2019
ISBN 978-3-7315-0870-0

Band 23 Jasmin Maria Jandke
Elastic and Inelastic Scanning Tunneling Spectroscopy on Iron-Based Superconductors. 2019
ISBN 978-3-7315-0747-5

Band 24 Kevin Edelmann
Electroluminescence from Plasmonic Excitations in a Scanning Tunnelling Microscope. 2019
ISBN 978-3-7315-0923-3

Band 25 Lei Zhang
Sub-Kelvin scanning tunneling microscopy on magnetic molecules. 2019
ISBN 978-3-86644-950-3

Band 26 Lukas Grünhaupt
Granular aluminium superinductors. 2019
ISBN 978-3-7315-0956-1

Band 27 Alexander Bilmes
Resolving locations of defects in superconducting transmon qubits. 2019
ISBN 978-3-7315-0967-7

Band 28 Marco Pfirrmann
Adding nonlinearity to an electromagnetic-magnonic quantum hybrid device. 2020
ISBN 978-3-7315-1003-1

Karlsruher Institut für Technologie
Physikalisches Institut

Future quantum hardware will utilize the individual advantages of connected quantum systems of different physical origin, with electromagnetic excitation being used to connect the individual components. While the underlying logic with fast and scalable quantum gates is often realized using a solid-state approach utilizing i.e. superconducting circuits, additional elements are needed for storing quantum information or frequency transducing. These circuits operate at microwave frequencies and allow for research of fundamental interactions of physical systems with light. With the nonlinear energy structure of a superconducting quantum bit, the interaction of matter with other physical systems, i.e. spins, can be studied in similar fashion. In order to achieve strong coherent coupling of superconducting circuit elements to magnetic spin excitation the number of participating spins is increased and collective magnetic bulk excitation are employed to study spin-based hybrid systems.

In this book, hybrid systems based on yttrium-iron-garnet (YIG), three dimensional microwave cavity resonators, and superconducting transmon qubits, are investigated by continuous wave and pulsed microwave spectroscopy. Limitations to the magnetic linewidth in the quantum regime are identified and coherent exchange between a magnon and a superconducting qubit are demonstrated. Finally, a first step towards a strongly coupled hybrid system containing all three components is demonstrated.

ISSN 2191-9925
ISBN 978-3-7315-1003-1